

REFLECTIVE AND TRANSPARENT DIFFRACTIVE OPTICAL ELEMENTS
AND THEIR ANGULAR RESPONSE

A THESIS SUBMITTED TO
THE GRADUATE SCHOOL OF NATURAL AND APPLIED SCIENCES
OF
MIDDLE EAST TECHNICAL UNIVERSITY

BY

PARISA NAGHINAZHADAHMADI

IN PARTIAL FULFILLMENT OF THE REQUIREMENTS
FOR
THE DEGREE OF DOCTOR OF PHILOSOPHY
IN
MICRO AND NANOTECHNOLOGY

MARCH 2025

Approval of the thesis:

**REFLECTIVE AND TRANSPARENT DIFFRACTIVE OPTICAL
ELEMENTS AND THEIR ANGULAR RESPONSE**

submitted by **PARISA NAGHINAZHADAHMADI** in partial fulfillment of the requirements for the degree of **Doctor of Philosophy in Micro and Nanotechnology Department, Middle East Technical University** by,

Prof. Dr. Naci Emre Altun
Dean, Graduate School of **Natural and Applied Sciences** _____

Prof. Dr. Emrah Ünalın
Head of Department, **Micro and Nanotechnology** _____

Assist. Prof. Dr. Ihor Pavlov
Supervisor, **Micro and Nanotechnology, METU** _____

Assoc. Prof. Dr. Serdar Kocaman
Co-supervisor, **Electrical and Electronics Engineering, METU** _____

Examining Committee Members:

Assist. Prof. Dr. Parviz Elahi
Faculty of Engineering, Özyeğin University _____

Assist. Prof. Dr. Ihor Pavlov
Department Of Physics, METU _____

Prof. Dr. Enver Bulur
Department of Physics, METU _____

Prof. Dr. Halil Berberoglu
Department Of Physics, Ankara Haci Bayram Veli University _____

Assoc. Prof. Dr. Selçuk Yerci
Electrical and Electronics Engineering, METU _____

Date:13.03.2025

I hereby declare that all information in this document has been obtained and presented in accordance with academic rules and ethical conduct. I also declare that, as required by these rules and conduct, I have fully cited and referenced all material and results that are not original to this work.

Name, Surname: Parisa Naghinazhadahmadi

Signature :

ABSTRACT

REFLECTIVE AND TRANSPARENT DIFFRACTIVE OPTICAL ELEMENTS AND THEIR ANGULAR RESPONSE

Naghinazhadahmadi, Parisa

Ph.D., Department of Micro and Nanotechnology

Supervisor: Assist. Prof. Dr. Ihor Pavlov

Co-Supervisor: Assoc. Prof. Dr. Serdar Kocaman

March 2025, 91 pages

Improving solar cell efficiency has been a primary focus in achieving cost-effective and efficient solar cells, fulfilling space requirements and reducing environmental footprints. Of the various techniques available to improve the efficiency of solar cells, integrating diffractive optical elements (DOEs) with multi-junction solar cells has gained significant attention as a promising solution. However, DOEs are designed and optimized to operate under a fixed incident angle, hindering their use in solar cell applications. Therefore, the design of dedicated angle-independent DOEs capable of simultaneously splitting and concentrating sunlight (SpliCons) is paramount for the solar energy industry. In this thesis we used a significantly fast experimental approach to spectrally split and concentrate broadband light using SpliCons operating under angled illumination. In our experimental setup, a phase-only spatial light modulator (SLM) is used to emulate the SpliCons, where the thickness variations in the SpliCon are mimicked by controlling and modifying the gray levels in the SLM. The broadband spectrum is split and concentrated in the regions that are chosen for red (560-875 nm), green (425-620 nm), and blue (420-535 nm) wavelengths. We obtain

58%, 51% and 59% spectral splitting ratios with an enhancement factor of 202%, 188% and 204% for red, green, and blue channels, respectively. Experimentally, we show that the angle response of our angle-independent SpliCon is enhanced by 4.8 times which is limited by the acceptance angle of our setup. We further calculated the angle response of our SpliCon design using convolution method and show the angle independency of spectral splitting and concentration over a $\pm 40^\circ$ span. A proof-of-concept SpliCon has been fabricated by stereolithography additive manufacturing method using an ultra-clear resin with a refractive index of 1.45, closely resembling that of glass. The fabricated SpliCons have been tested under angled illumination, and their angular response is studied. Test results have revealed a successful angle-independent simultaneous splitting and concentration of the broadband light, validating the concept. The designed SpliCons represent a significant advancement toward the feasibility of building-integrated solar cells by enhancing tolerance to variations in the incident angle of sunlight, thereby improving overall energy capture and efficiency.

Keywords: Wavefront Shaping, Solar Cell Efficiency, Diffractive Optical Elements, Spectral Splitting, Stereolithography Additive Manufacturing.

ÖZ

YANSITICI VE ŞEFFAF KIRINIMSAL OPTİK ELEMANLAR VE AÇISAL TEPKİLERİ

Naghinazhadahmadi, Parisa

Doktora, Mikro ve Nanoteknoloji Bölümü

Tez Yöneticisi: Dr. Öğr. Üyesi. Ihor Pavlov

Ortak Tez Yöneticisi: Doç. Dr. Serdar Kocaman

Mart 2025 , 91 sayfa

Güneş hücrelerinin verimliliğini artırmak, uygun maliyetli ve verimli güneş hücreleri elde edilmesinde, alan gereksinimlerini karşılama ve çevresel ayak izinin azaltılmasında temel bir odak noktası olmuştur. Güneş hücrelerinin verimliliğini artırmak için mevcut çeşitli teknikler arasında, kırınımlı optik elemanların (KOE'ler) çok bağlantılı güneş hücreleri ile birleştirilmesi umut vaat eden bir çözüm olarak önemli ilgi kazanmıştır. Ancak, KOE'ler sabit bir geliş açısı altında çalışacak şekilde tasarlanıp optimize edildiğinden, güneş hücresi uygulamalarında kullanılmalarını engellemektedir. Bu nedenle, güneş ışığını aynı anda bölebilen ve yoğunlaştırabilen (SpliCons) açıdan bağımsız KOE'lerin tasarımı, güneş enerjisi endüstrisi için büyük önem taşımaktadır. Bu tezde, açılı aydınlatma altında çalışan SpliCons kullanarak geniş bantlı ışığı spektral olarak bölme ve yoğunlaştırma için oldukça hızlı bir deneysel yaklaşım kullandık. Deney düzeneğimizde, yalnızca faz modülasyonu yapan bir uzamsal ışık modülatörü (SLM) SpliCon'u taklit etmek için kullanılmıştır; SpliCon'daki kalınlık değişimleri, SLM'deki gri tonlarının kontrolü ve değiştirilmesiyle taklit edilmiştir.

Geniş bantlı spektrum, kırmızı (560-875 nm), yeşil (425-620 nm) ve mavi (420-535 nm) dalga boyları için seçilen bölgelere bölünmüş ve yoğunlaştırılmıştır. Kırmızı, yeşil ve mavi kanallar için sırasıyla %58, %51 ve %59 spektral ayırma oranları ve %202, %188 ve %204 yoğunlaştırma faktörleri elde edilmiştir. Deneysel olarak, açıdan bağımsız SpliCon'umuzun açı tepkisinin, deney düzeneğimiz'n kabul açısıyla sınırlı olmak üzere 4.8 kat arttığını gösterdik. Ayrıca, SpliCon tasarımımızın açı tepkisini konvolüsyon yöntemi kullanarak hesapladık ve spektral bölünme ve yoğunlaştırmanın $\pm 40^\circ$ aralığında açıdan bağımsız olduğunu gösterdik. Bir kavramsal kanıtı SpliCon, caminkine yakın bir kırılma indisine (1.45) sahip ultra-şeffaf bir reçine kullanılarak stereolitografi eklemeli imalat yöntemiyle üretilmiştir. Üretilen SpliCon'lar, açılı aydınlatma altında test edilmiş ve açısal tepkileri incelenmiştir. Test sonuçları, geniş bantlı ışığın açıdan bağımsız bir şekilde aynı anda bölünmesi ve yoğunlaştırılmasının başarılı olduğunu ortaya koyarak konsepti doğrulamıştır. Tasarımı yapılan SpliCon'lar, güneş ışığının geliş açısındaki değişimlere karşı toleransı artırarak toplam enerji yakalama kapasitesini ve verimliliği iyileştirmek suretiyle bina entegreli güneş pillerinin uygulanabilirliğine yönelik önemli bir ilerlemeyi temsil etmektedir.

Anahtar Kelimeler: Dalga Cephesi Şekillendirme, Güneş Hücresi Verimliliği, Kırınmsal Optik Elemanlar, Spektral Ayırma, Stereolitografi Katmanlı Üretim.

To my family ...

ACKNOWLEDGMENTS

I would like to extend my sincere gratitude to my advisor, Assist. Prof. Dr. Ihor Pavlov, for his invaluable guidance, encouragement, and the wonderful moments he provided throughout this study. I would also like to express my appreciation to my co-advisor, Assoc. Prof. Dr. Serdar Kocaman, for his support.

I also sincerely thank Associate Prof. Dr. Emre Yüce for his innovative ideas and support during this work. Additionally, I am deeply grateful to Prof. Dr. Alpan Bek for providing me with the opportunity to work in their lab.

I extend my gratitude to the members of the Programmable Photonics and ALPhA Group, especially Berk Nezir Gün, Dr. Alim Yolalmaz, Mehmet Tabak, Dr. Şahin Kürekçi, and Dr. Arian Goodarzi, for their valuable assistance.

I am deeply thankful to my family for their unwavering support. A special thanks to my spouse, Dr. Samet Akar, for his boundless love. I am also profoundly grateful to my sister, Dr. Somaye Naghinazhad, for her endless love and support.

Furthermore, I appreciate my dear friends Dr. Naz Dizeci, Pardis Aydın, Dr. Damla Alptekin, Büşra Altınsoy, and Sema Yektaee for their support throughout my thesis journey. Thank you all for your kindness and presence.

TABLE OF CONTENTS

| | |
|---|-----|
| ABSTRACT | v |
| ÖZ | vii |
| ACKNOWLEDGMENTS | x |
| TABLE OF CONTENTS | xi |
| LIST OF TABLES | xiv |
| LIST OF FIGURES | xv |
| LIST OF ABBREVIATIONS | xx |
| CHAPTERS | |
| 1 INTRODUCTION | 1 |
| 1.1 Motivation and Problem Definition | 1 |
| 1.2 Multi-junction solar cells | 3 |
| 1.3 Spectral Splitting | 6 |
| 1.4 Angular Dependence of Solar Cell Efficiency | 8 |
| 1.5 Proposed Methods and Models | 11 |
| 1.6 The Outline of the Thesis | 12 |
| 2 DESIGN OF ANGLE-INDEPENDENT SPLICONS FOR IMPROVED SOLAR CELL EFFICIENCY | 13 |
| 2.1 Introduction | 13 |

| | | |
|---------|--|----|
| 2.2 | Experimental Setup | 14 |
| 2.3 | Measuring the Acceptance Angle | 19 |
| 2.4 | Wavefront Shaping-Light Shifting | 20 |
| 2.5 | Wavefront Shaping-Concentration | 24 |
| 2.5.1 | Optimization Algorithm | 28 |
| 2.6 | Results of the Optimization | 30 |
| 2.7 | Conclusions | 38 |
| 3 | CALCULATING SPLICON'S RESPONSE FOR WIDE INCIDENT AN- GLES | 41 |
| 3.1 | Theory of Fourier Optics | 41 |
| 3.2 | Methodology | 42 |
| 3.3 | Results | 46 |
| 3.4 | Conclusions | 51 |
| 4 | FABRICATION AND EXPERIMENTAL TESTING OF SPLICONS | 55 |
| 4.1 | Transforming an Optimized SpliCon to a Physical SpliCon | 55 |
| 4.2 | Fabrication of SpliCons | 57 |
| 4.2.1 | Direct Laser Writing of Crown Glass | 59 |
| 4.2.2 | Fabrication of SpliCons by PDMS Casting | 62 |
| 4.2.3 | Fabrication of SpliCons by Stereolithography Additive Man- ufacturing | 63 |
| 4.2.3.1 | Materials for the SLA | 64 |
| 4.2.3.2 | Computer-aided Design | 64 |
| 4.2.3.3 | SLA 3D Printing | 65 |
| 4.3 | Experimental Testing of SpliCons | 68 |

| | | |
|-----|--|----|
| 4.4 | Conclusions | 72 |
| 5 | CONCLUSION AND OUTLOOK | 73 |
| 5.1 | Recommendations for Future Works | 74 |
| | REFERENCES | 75 |
| | CURRICULUM VITAE | 89 |

LIST OF TABLES

TABLES

| | |
|---|----|
| Table 2.1 Enhancement Factors Corresponding to Various Square Superpixel- to-Total SLM Area Ratios | 27 |
| Table 2.2 Enhancement values for different number of iterations | 37 |
| Table 2.3 Splitting Ratio for different number of iterations | 37 |
| Table 2.4 Comparison of Iterations for Enhancement and Splitting Ratios . . . | 38 |

LIST OF FIGURES

FIGURES

| | | |
|------------|--|----|
| Figure 1.1 | (a) Vertically stacked (Tandem) multi-junction solar cell, (b) Laterally aligned multijunction solar cell | 4 |
| Figure 1.2 | Three most commonly used spectral splitting methods: (a) Dichroic spectrum-splitting filter, (b) Surface relief grating, (c) Volume grating | 7 |
| Figure 2.1 | (a) Schematic of the optical system used to emulate SpliCon using an SLM. (The optical system consists of a fiber (F), a plano convex lens (C), neutral density filter (ND), mirrors (M), a polarizer (P), an actuated controlled mirror (ACM), and converging lenses (L)), (b) Image on the CCD camera before optimization, (c) Image showing simultaneous spectrum-splitting and concentration on the region of interest after optimization, (d) Phase pattern of the SLM which splits and concentrates the light. | 15 |
| Figure 2.2 | Real optical system | 18 |
| Figure 2.3 | Measuring the acceptance angle of the system | 19 |
| Figure 2.4 | (a) The blazed grating phase plate generated by Holoeye software and used to shift the light to the uppermost portion of the CCD camera, (b) The image on the CCD camera before the application of phase plate, (c) Image recorded on the CCD camera showing the shifted light to the uppermost portion of the camera. | 20 |

| | | |
|-------------|--|----|
| Figure 2.5 | (a) The blazed grating phase plate generated by Holoeye software and used to shift the light to the lowermost portion of the CCD camera, (b) Image recorded on the CCD camera showing the shifted light to the lower portion of the camera. | 21 |
| Figure 2.6 | (a) The combined phase plate used to shift the light to the central region of the CCD camera, (b) The image obtained on the CCD camera after using combined blazed grating phase plate. | 22 |
| Figure 2.7 | The normalized intensity for red, green and blue channels using combined blazed grating phase plate. | 23 |
| Figure 2.8 | Schematic representation of the proposed design, integrating a combined blazed grating (gray region) with a central square superpixel region (black). Different configurations illustrate variations in the width of the square superpixel region relative to the total SLM area. | 25 |
| Figure 2.9 | (a) A combined blazed grating with a superpixel region at the center, displayed in grayscale. The inset provides a magnified view of the central superpixel-modulated area, (b) The corresponding experimental image captured on the CCD camera, showing the effect of the superpixel region, (c) Normalized intensity profiles along the Y-axis for red, green, and blue channels, highlighting the modulation effects introduced by the superpixel region. | 26 |
| Figure 2.10 | (a) Combined background rectangular superpixels with square superpixels at the middle of the phase plate, (b) Corresponding raw image on the CCD camera(c)The normalized intensity for red, green and blue channels along Y-axis of the image | 28 |
| Figure 2.11 | Flowchart of the experimental optimization method | 29 |
| Figure 2.12 | The phase plate after optimization using rectangular superpixels . | 31 |

| | | |
|-------------|---|----|
| Figure 2.13 | (a) The raw image on the CCD camera using optimized phase plate with rectangular superpixels, (b) The normalized intensity using optimized phase plate with rectangular superpixels, showing successful simultaneous spectrum-splitting and concentration. | 32 |
| Figure 2.14 | The intensity profiles for combined color channels (a) before (b) after optimization. (c) Differential intensity changes for combined color channels, Differential change for separate colors (d) Red, (e) Green and (f) Blue. The dashed lines indicate the target areas in which the colors are concentrated. The green and blue bands are directed to a rectangular region with the same dimensions at the lower half of the target plane. . . | 33 |
| Figure 2.15 | The phase plate of a conventional DOE | 34 |
| Figure 2.16 | The raw image of the conventional DOE on CCD camera | 35 |
| Figure 2.17 | Enhancement of angle-independent SpliCon compared with conventional DOE | 36 |
| Figure 3.1 | The spectral radiance from a black-body as a function of wavelength | 43 |
| Figure 3.2 | Refractive Index of BK-7 glass as a function of wavelength | 44 |
| Figure 3.3 | Alignment of input and output planes which are divided into pixels to obtain angular response of the optimized SpliCon | 45 |
| Figure 3.4 | (a) The phase plate reported by Yolalmaz and Yüce used for validation, (b) SOE of the test DOE at 400 nm, which is measured at the central pixel of the target plane at different angles of illumination . . . | 47 |
| Figure 3.5 | Efficiency map of the SpliCon as a function of wavelength (400–1100 nm) and incidence angle (-40° to 40°). | 48 |
| Figure 3.6 | Efficiency variation of the SpliCon as a function of incidence angle for selected wavelengths (400 nm, 550 nm, 700 nm, and 1100 nm). | 48 |

| | | |
|-------------|---|----|
| Figure 3.7 | Wavelength-dependent efficiency of the SpliCon for different incidence angles (0°, 10°, 20°, and 40°). | 49 |
| Figure 3.8 | Efficiency map of the conventional DOE as a function of wavelength (400–1100 nm) and incidence angle (-40° to 40°). | 49 |
| Figure 3.9 | Efficiency map of the conventional DOE as a function of wavelength (400–1100 nm) and incidence angle (-40° to 40°). | 50 |
| Figure 3.10 | Efficiency map of the conventional DOE as a function of wavelength (400–1100 nm) and incidence angle (-40° to 40°). | 50 |
| Figure 3.11 | Calculations validate the angle independency of the SpliCon outside the acceptance angle of the experimental setup which expands up to $\pm 40^\circ$ | 51 |
| Figure 4.1 | (a) The surface of the SLM with seven varying refractive indices, and (b) A physical DOE with seven varying height levels. | 56 |
| Figure 4.2 | Refractive index vs. gray levels of the SLM | 58 |
| Figure 4.3 | (a) Thickness of the physical SpliCon versus Pixel number, and (b) The histogram of thickness distribution of the physical SpliCon | 58 |
| Figure 4.4 | Schematic illustration of the direct laser writing method to realize SpliCons on Crown Glass | 60 |
| Figure 4.5 | Micro-channels produced at the minimum laser energy (~2.5 μ J) on Crown Glass | 61 |
| Figure 4.6 | Schematic representation of the PDMS casting process: (a) Cross-section of the mold, (b) Pouring PDMS into the Mold Cavity, (c) Demolding of SpliCon after curing | 62 |
| Figure 4.7 | Micro-channels fabricated on Silicon using direct laser writing: (a) Different number of scans with an etching period of 5 min., (b) Different number of scans with an etching period of 8 min. | 63 |

| | | |
|-------------|---|----|
| Figure 4.8 | Solid Model of the SpliCon | 65 |
| Figure 4.9 | SLA settings for the SpliCon fabrication | 66 |
| Figure 4.10 | SLA 3D printing to realize proof-of-concept SpliCons | 67 |
| Figure 4.11 | (a) Proof-of-concept SpliCons fabricated by SLA 3D printing, and (b) Topography of the SpliCons measured by LSM. | 67 |
| Figure 4.12 | Experimental setup to test the proof-of-concept SpliCon | 68 |
| Figure 4.13 | The raw image on the CCD camera for the proof-of-concept SpliCon | 69 |
| Figure 4.14 | The intensity profiles for: (a) plane device, (b) proof-of-concept SpliCon, (c) Differential intensity changes for combined color chan- nels. Differential change for separate colors (d) Red, (e) Green and (f) Blue. The dashed lines indicate the target areas in which the colors are concentrated. | 70 |
| Figure 4.15 | The enhancement of the proof-of-concept SpliCon under angled illumination | 71 |

LIST OF ABBREVIATIONS

ABBREVIATIONS

| | |
|------|-----------------------------------|
| 1D | 1 Dimensional |
| 3D | 3 Dimensional |
| DOE | Diffractive Optical Element |
| LFR | Linear Fresnel Reflector |
| DSC | Dye Solar Cell |
| CCD | Charge-coupled Device |
| ND | Neutral Density |
| SLM | Spatial Light Modulator |
| PDMS | Polydimethylsiloxane |
| SLA | Stereolithography |
| HF | Hydrofluoric |
| STL | Standard Tessellation Language |
| CAD | Computer-aided Design |
| LSM | Laser Scanning Microscope |
| FWHM | Full-width Half Maximum |
| SCE | Spectral Conversion Efficiency |
| ROI | Region of Interest |
| RGB | Red, Green and Blue |
| MMF | Mismatch Correction Factor (MMF) |
| FGM | Functional Gradient Material |
| CTE | Coefficient of Thermal Expansion |
| PV | Photovoltaic |
| BIPV | Building-integrated Photovoltaics |

CHAPTER 1

INTRODUCTION

1.1 Motivation and Problem Definition

The use of solar energy as a renewable and sustainable energy source is gaining more and more importance due to the ever-increasing environmental problems. The widespread use of this energy source not only demands for economic ways of solar panel production but also requires an increased efficiency. Photovoltaic (PV) technology, already underestimated, has emerged as a new force in controlling global warming thanks to the reduced cost and improved power conversion efficiency (PCE) [1–7].

The low conversion efficiency of the solar cells is considered as one the major limiting factor to achieving low-cost solar energy. For single-junction solar cells, an efficiency of 28.3% is reported by Green et al. [6]. This value is very close to the maximum theoretical efficiency of 33.7% dictated by the Shockley–Queisser limit [4]. This can be attributed to various phenomena. Important of all is the broadband nature of the sunlight, which contains wavelengths in the range of 350 nm–2000 nm [4]. Depending on the bandgap of the solar cell materials, only a fraction of this broadband radiation will be converted into a useful form of energy. Incident photons having energies above the energy of the bandgap of the semiconductor material trigger the phenomenon of thermalization, where they lose the excess energy in the form of heat. The incident photons with fewer energies will not be absorbed, resulting in so-called below-bandgap losses [4].

Another important factor that largely affects the efficiency of the solar panels is the variation in the incident angle of the sunlight. It is a well-known fact that the incident angle of the sunlight changes during the day and shows large variations seasonally.

PV panels with a higher tolerance to the incident angle of incoming light contribute to increased solar power generation in two ways: by enhancing solar cell efficiency through receiving a greater intensity of the sunlight and by extending the solar utilization time [8].

In this thesis, we have focused on two critical aspects of the problem of PCE in PV cells and explored strategies to overcome these limitations. The first aspect pertains to the intrinsic properties of the semiconductor material, as each material exhibits a specific bandgap that determines the range of the solar spectrum it can effectively convert into electrical energy. Since conventional single-junction solar cells can absorb only a restricted portion of the solar spectrum, a substantial portion of incident energy remains unutilized, leading to efficiency losses.

The second aspect we addressed involves the daily and seasonal variations in the incident angle of sunlight. Due to the Earth's rotation and orbital motion, the angle at which sunlight strikes a solar panel continuously changes, resulting in fluctuations in the amount of absorbed energy. Significant losses can occur if solar panels are not optimized for these variations, limiting the overall energy output throughout the day and across different seasons.

To tackle these challenges, we designed and optimized diffractive optical elements (DOEs) capable of simultaneous spectrum-splitting and broadband light concentration, referred to as SpliCons. These advanced optical structures effectively split incoming light into different wavelength components while simultaneously concentrating it, enabling more efficient energy harvesting. SpliCons are particularly advantageous when used in conjunction with parallel multi-junction solar cells, where multiple semiconductor materials are deliberately layered so that each material absorbs its corresponding portion of the solar spectrum. This approach significantly minimizes below-bandgap losses and thermalization effects, thereby enhancing the system's overall efficiency.

Moreover, to mitigate the losses caused by variations in the incident sunlight angle, we optimized SpliCons to be angle-independent. By ensuring consistent performance across a wide range of incident angles, our approach enables more stable and sustained energy generation, regardless of the time of day or season. This design en-

hances the adaptability of PV systems to real-world applications, making them more reliable and efficient.

In this chapter, we will delve into some of the most important and recent advancements in improving the PCE of PV systems. We will highlight key innovations, experimental findings, and theoretical insights contributing to developing next-generation solar energy technologies. Through this discussion, we aim to comprehensively understand how cutting-edge optical and material engineering strategies can revolutionize solar power generation and contribute to the transition toward more sustainable energy solutions.

1.2 Multi-junction solar cells

Several researchers have focused on improving solar cell efficiencies using different approaches [9–15], among which multi-junction solar cells are promising [4, 10, 16–20]. In multi-junction solar cells, the aim is to absorb different wavelengths of solar radiation by suitable semiconductor materials [9]. This is an efficient approach to overcome the Shockley-Queisser limit of 33.7% for single-junction solar cells [16,21]. Triple-junction solar cells have already found significant utility in space applications [22]. By increasing the number of junctions in these cells, an asymptotic increase in the conversion efficiency of up to 65% has been reported [23]. It has been reported that a theoretical efficiency of about 85% can be realized by selecting an appropriate combination of semiconductor materials [19,24]. To achieve this theoretical efficiency, there is a need for optical concentration of the light to intensify the density of photogenerated carriers in the material and to force the voltage of junctions near the bandgap limit by additionally separating the quasi-Fermi levels [25].

Among recent developments in solar cell technologies, multi-junction perovskite solar cells have emerged as promising candidates for integration into spectral splitting systems [7] thanks to their excellent characteristics, such as high conversion efficiencies of up to 25.2% [26], approaching the efficiency of silicon-based cells (26.7%) [27, 28], unveiling a broad range of tunable energy bandgaps, spanning from 1.25 eV to 2.3 eV [29–31], enabling their integration into multi-junction and

spectrum-splitting systems and benefiting from low-energy manufacturing processes, which could lead to production costs lower than those of silicon cells [32].

Presently, numerous companies and research groups are directing their efforts towards concentration systems, aiming to facilitate the deployment of these cells for terrestrial applications [19]. This strategic focus reflects the expanding interest and recognition of the potential advantages these advanced solar cell technologies offer outside the boundaries of space exploration. However, high concentrating power is somehow problematic, as the cells cannot utilize the diffuse sunlight (light scattered by the atmosphere), and it is not compatible with the simpler single-axis tracking systems commonly used in large-scale photovoltaic plants. These issues have led to numerous multi-junction cell manufacturers to abandon their expansion plans [33].

Multi-junction solar cells can have two main architectures based on their method of arrangement. The first method is to stack the sub-cells of different bandgap semiconductor materials vertically, called tandem multi-junction solar cells [1, 17, 24], as illustrated in Figure 1.1(a).

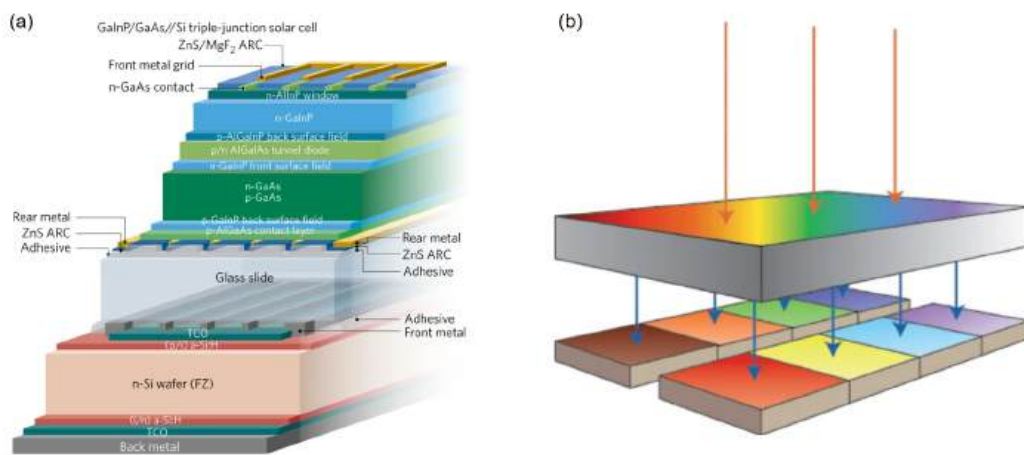


Figure 1.1: (a) Vertically stacked (Tandem) multi-junction solar cell [1], (b) Laterally aligned multi-junction solar cell [2].

Vertically stacked multi-junction solar cells are shown to be promising for concentrated photovoltaic applications [34]. Different efficiencies have been reported based on the semiconductor material employed. An efficiency of 19.19% has been reported by Xing et al. [34] under 2480 suns. They also showed that the efficiency can be

increased by using numerical calculations and optimization up to 30%. A higher efficiency of 44% has been reported by Green et al. [6], while Yuen et al. [35]. have reported an efficiency of 43.5%. In tandem multi-junction solar cells, the upper layer (higher energy bandgap junction) is selected to absorb all the short wavelengths while permitting longer wavelengths to enter the lowermost layers (lower energy bandgap junctions). The total efficiency of the tandem cells (η_{SSS}) consisting of k junctions is calculated as given in Eq. 1.1 [36]:

$$\eta_{SSS} = \frac{1}{P_{AM1.5}} \cdot \int E_{AM1.5}(\lambda) \left[SCE_1(\lambda) + \sum_{k=1}^K \left(SCE_{k+1}(\lambda) \cdot \prod_{i=1}^k T_i(\lambda) \right) \right] d\lambda \quad (1.1)$$

where λ is the wavelength, SEC is the spectral conversion efficiency, $T(\lambda)$ is the transmittance and $P_{AM1.5}$ and $E_{AM1.5}$ are the incident optical power and spectral irradiance corresponding to the Air Mass 1.5 standard spectrum, respectively.

Due to their structure, Tandem solar cells can naturally split the solar radiation. However, they face three major limitations, which limit their low-cost applications [10,24]. The first limitation concerns their fabrication method, as these solar cells require complex epitaxial growth. As in these kind of solar cells, different semiconductors are connected in series, they produce different currents, which results in current mismatch issues. As a result, based on Kirchhoff's law, the overall current output of the tandem device is constrained by the sub-cell with the lowest current [37]. The lattice matching between stacks of semiconductor materials is another limitation of tandem solar cells [38].

The second approach is to laterally align the cells, which are named parallel multi-junction solar cells or lateral spectrum-splitting systems as illustrated in Figure 1.1(b). These systems make it possible to avoid the lattice and current-matching constraints associated with tandem architectures [2]. In this type of multi-junction solar cells, more sub-cells can be integrated into parallel, which largely reduces the thermalization loss and hence results in an increased efficiency [11,39]. Additionally, removing lattice matching constraints provides more flexibility in choosing semiconductor material for the cells.

For a parallel multi-junction solar cell with k different cells, the total efficiency can

be calculated as Eq. 1.2 [36]:

$$\eta_{SS} = \frac{1}{P_{AM1.5}} \cdot \int E_{AM1.5}(\lambda) \left[\sum_{k=1}^K SCE_k \cdot \tau_k(\lambda) \cdot T(\lambda) \right] d\lambda \quad (1.2)$$

where λ is the wavelength, SEC is the spectral conversion efficiency, $T(\lambda)$ is the transmittance, $\tau_k(\lambda)$ is the spectral overlap parameter and $P_{AM1.5}$ and $E_{AM1.5}$ are the incident optical power and spectral irradiance corresponding to the Air Mass 1.5 standard spectrum, respectively.

For spectrum-splitting systems, the light can be concentrated first, then spectrally split, or it can be concentrated and spectrally split at the same time using certain optical elements [40]. When spectral splitting elements are used, an additional optical loss is introduced compared with a tandem multi-junction structure. Therefore, the simultaneous concentration and splitting of the light are paramount for successfully implementing these solar cells, which can be achieved by designing and optimizing DOEs. Simultaneously splitting and concentrating will also resolve the great dilemma linked with singular concentrators, mitigating the adverse impact of high temperatures on solar cell efficiency [41]. The following section is devoted to the relevant beam splitting techniques.

1.3 Spectral Splitting

Since parallel multi-junction solar cells cannot naturally split the incident sunlight, beam splitting is an indispensable part of the design of these solar cells. The three most commonly used spectral splitting techniques has been shown schematically in Figure 1.2.

The use of a dichroic spectrum-splitting filter (also known as interference filters) made by depositing layers of materials with low and high refractive indices has been reported by Zhang et al. [42]. The main issue associated with dichroic filters is that the perfect functionality can only be attained under collimated incoming light. When the incident angle changes, their optical concentration ratio reduces significantly [43]. The multi-layer structure in these filters is inherently reflective outside their design-

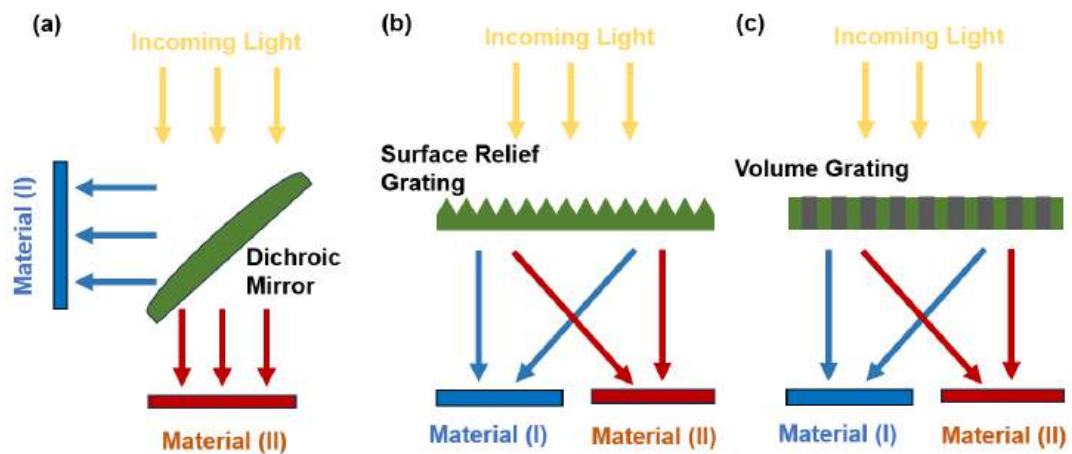


Figure 1.2: Three most commonly used spectral splitting methods: (a) Dichroic spectrum-splitting filter, (b) Surface relief grating, (c) Volume grating

nated transmission bands. This reflective behavior is a key factor that complicates the design of modules—especially when attempting to match the form factors of conventional flat-panel designs. The interference effects associated with the high-reflection and spectral filtering cause unwanted reflections that necessitate additional optical or mechanical design considerations [44].

A one-dimensional (1D) surface relief grating called “polychromat” has been used by Mohammad et al. [45] for spectrum splitting and concentration. Their device is called 1D, as it has been pixelated only in one direction and was uniform in the other direction. Their device consisted of 5001 pixels with a pixel size of $3\ \mu\text{m}$. A step height of 23.81 nm is used with 64 different levels. An increase of 35.52% in the overall efficiency has been reported. For solar cells made from GaInP, GaAs and Silicon, they achieved an increase in the PCE of 43.63% , 30.84% and 30.86%, respectively.

Volume holograms can also be preferred for spectrum-splitting PV systems. These holograms can operate either by transmission or reflection. The volume and phase type holograms are among the most extensively used holograms for the purpose of splitting and concentration [46]. The use of DOEs for efficient splitting and concentrating of broadband sunlight for solar energy applications has been shown by Kim et al. [12]. Because of the importance of simultaneous splitting and concen-

tration of broadband sunlight in solar energy applications, the term SpliCon has been coined by Gün and Yüce [47]. In addition to their simultaneous concentration and splitting, SpliCons are also superior to conventional spectral splitters such as prisms [48], dichroic mirrors [13], holographic structures [49], and combinations of prism-cylindrical lenses [50] because of their small footprint, cost-effectiveness, scalability to larger areas, light configurations and suitability for practical solar applications [3,51–55]. SpliCons also outperform conventional linear Fresnel reflectors (LFRs) because LFRs may cause shading, blockage and encounter issues with solar energy loss [56]. Moreover, SpliCons can also guide sunlight away from metallic contacts blocking the light, thereby increasing the overall efficiency [57].

1.4 Angular Dependence of Solar Cell Efficiency

A stationary PV panel achieves maximum electric power generation when the incident light strikes it perpendicularly, meaning the incident angle is zero. Under these optimal conditions, the solar cell absorbs the maximum possible intensity of sunlight, leading to peak power conversion efficiency. However, in real-world applications, the incident angle of the sun continuously changes throughout the day due to the Earth’s rotation and further varies seasonally due to its orbital motion. These variations lead to fluctuations in the amount of light the solar panel captures, ultimately reducing the overall energy output. In this case, improperly designed angles result in a substantial difference in the efficiency of the solar cells [58]. In certain geographic locations (e.g. higher latitude regions), the efficiency losses caused by the dependence of solar cells on the incident angle of sunlight can be the primary reason for reduced energy generation [59].

To tolerate these variations and maintain stable performance, solar panels must exhibit a high tolerance to changes in the incident light angle. A solar panel with robust angular independence can sustain efficient energy conversion over a wide range of incident angles, thereby maximizing the total power-generation capacity and effective solar energy utilization period. By optimizing solar cells for angle independence, power output can be enhanced not only at peak conditions but also during early morning, late afternoon, and throughout different seasons, ensuring more steady and con-

sistent energy harvesting.

Several advanced approaches have been discovered to expand this angular tolerance. These include integrating anti-reflective coatings [60, 61], light-trapping structures [62, 63], and adaptive tracking systems [64] that dynamically adjust panel orientation to optimize sunlight capture. Additionally, recent developments in nanophotonic and plasmonic materials [65] have aided more efficient light manipulation, allowing solar cells to sustain higher absorption rates even at non-optimal angles [66].

Among the aforementioned approaches, sun-tracking systems are widely accepted for maximizing solar energy capture by adjusting the orientation of panels to follow the sun's path. However, this approach has significant limitations. The primary drawback is the high initial cost associated with these systems. The complexity and mechanical components of sun-tracking mechanisms significantly elevate the initial investment required for installation [67]. Another critical limitation is energy consumption. The motors and control systems that enable tracking consume a portion of the energy generated, thereby reducing the net energy output [68]. Additionally, the high maintenance requirements pose a challenge. The mechanical complexity of tracking systems increases the potential for technical issues, leading to higher maintenance demands and associated costs. Finally, the unsuitability for stationary applications is another major drawback. Sun-tracking mechanisms are not feasible for installations with fixed panels, such as building-integrated photovoltaics (BIPV), limiting their applicability in such contexts [69]. Due to these challenges, alternative approaches are being explored to enhance solar energy capture without relying on sun-tracking systems.

In the literature, there exists a limited amount of work that reports the angular response of solar cells. The angular response of single-junction solar cells (GaAs) has been studied by Kosten et al. [70]. Their theoretical study based on a detailed balanced model of the GaAs solar cells revealed that limiting the emission angle by light trapping techniques can be effectively used to achieve efficiencies of 38%.

Denkler et al. [71] have studied the angular response of bulk-heterojunction organic solar cells (poly(3-hexylthiophene): 1-(3-methoxy-carbonyl-propyl)-phenyl-C61). The study of Cheyns et al. [72] deals with the angular response of thin-film organic solar

cells. Their finding showed that the light distribution in the thin layers of organic solar cells significantly alters by the changes in the incident angle. Sha et al. [58] have developed a theoretical model to study the angular response of thin-film organic solar cells. They considered solar cells having periodic gold back nanostrips. Their results showed a strong variation of the total absorptivity with changing of incident angle. Similar results have also been reported in the work of D'Ercole et al. [73] for the angular response of dye solar cells (DSCs).

Stockhausen et al. [74] have compared the effect of incident angle variations on the performance of three different solar cells i.e. Perovskite Solar Cells , Dye-Sensitized Solar Cells , and Silicon Heterojunction Solar Cells for building-integrated applications. The results indicate that Silicon Heterojunction and Perovskite Solar Cells follow a cosine-dependent efficiency reduction, while Dye-Sensitized Solar Cells show an improved efficiency at intermediate angles (15° – 45°), deviating from a purely geometric loss pattern.

The angular response of the bare and encapsulated silicon solar panels has been studied by Balenzategui and Chenlo [75]. Their findings revealed that the angular response of silicon solar cells is affected by surface texture and uniformity in bare cells, but encapsulation with front glass regulates their angular behavior, regardless of cell technology. Notably, textured mono-Si cells exhibit significant changes in angular response when encapsulated, with the combination of flat glass and textured surfaces reducing absolute angular deviations. Their findings highlight the dominant role of encapsulation in the angular performance of solar panels.

A comprehensive review of the literature reveals that notable research has been done to analyze the angular response of solar cells under angled illumination. These studies have provided valuable insights into how the conversion efficiency of different solar panel technologies fluctuates with variations in the incident angle of incoming light. However, less attention has been directed toward developing practical solutions to mitigate efficiency losses caused by angular variations, particularly in the context of Building-Integrated Photovoltaic (BIPV) applications, where fixed panel orientations pose a major challenge. Recognizing these limitations, our research focuses on designing angle-independent DOEs that can simultaneously perform spectrum splitting

and light concentration. By enhancing the tolerance of solar cells to incident angle variations, our approach aims to maximize energy capture and improve overall efficiency, offering a practical and scalable solution for BIPV and other stationary solar energy applications.

1.5 Proposed Methods and Models

In this thesis, an angle-independent spectral splitting and concentration system (SpliCons) is designed and optimized for the first time. The proposed methodology includes a highly efficient and rapid experimental approach to perform spectrum splitting and concentration of broadband light under angled illumination. The significant methods and models employed in this research are summarized as follows:

- A phase-only spatial light modulator (SLM) is utilized to emulate the SpliCon, where thickness variations are mimicked by modifying the gray levels in the SLM.
- The convolution method is implemented to calculate the angular response of the SpliCons across a broad illumination angle range of $\pm 40^\circ$.
- Stereolithography (SLA) additive manufacturing technique is employed for the first time to realize SpliCons using ultra-clear resin, ensuring high optical clarity and precision.
- The experimental setup enables the angle-independent operation of SpliCons, providing an effective solution for broadband spectral splitting and concentration.
- To generate the 3D solid models of the SpliCons, which contains more than 1000 micro-features, a subroutine has been developed for the SolidWorks program, which automatically generates our design, facilitating the design and manufacturing process of SpliCons.

1.6 The Outline of the Thesis

In Chapter 2, we discussed the design and optimization of angle-independent SpliCons for the broadband light's simultaneous spectral splitting and concentration. The experimental method and setup used for this purpose are introduced and described. The angle independence of the device has been verified over the acceptance angle of the system. In Chapter 3, the idea has been extended to the angles beyond the acceptance angle of the system. The use of the convolution method to calculate the response of the SpliCons under angled illumination has been explained. The enhancement of the device is calculated for a span of $\pm 40^\circ$. In Chapter 4, different techniques for fabricating SpliCons have been demonstrated. The challenges we faced during the realization of the SpliCons are discussed. The successful application of stereolithography to fabricate proof-of-concept devices has been shown. The successful operation of the device has been proved under angled illumination. Chapter 5 is devoted to the conclusions we achieved in this thesis, along with proposals for future works that can be done to extend the idea.

CHAPTER 2

DESIGN OF ANGLE-INDEPENDENT SPLICONS FOR IMPROVED SOLAR CELL EFFICIENCY

2.1 Introduction

As comprehensively outlined in Chapter 1, one of the key challenges in PV technology is the spectral mismatch between incident solar radiation and the absorption properties of the PV cell materials. Spectrum-splitting and light-concentration techniques have been proposed as viable methods for enhancing solar energy conversion efficiency to address this issue. Spectrum-splitting enables different wavelength bands to be directed toward PV cells optimized for specific spectral regions, thereby reducing thermalization and below bandgap losses and improving overall efficiency. Additionally, light concentration increases the intensity of incident radiation, enhancing the power output of the PV system.

In this chapter, we explore an experimental approach for designing and optimizing angle-independent spectrum-splitting concentrators (SpliCons) to achieve simultaneous spectral splitting and concentration of broadband light. Unlike conventional diffraction optical elements, which exhibit angular dependency and reduced efficiency at oblique incidence angles, the SpliCons developed in this study maintain stable performance across a range of incident angles. We employ a phase-only spatial light modulator to emulate the thickness variations in the SpliCon, providing an efficient means of testing and optimizing the optical and angular response of our device.

We have tried various phase plates, including blazed grating, blazed grating combined with square superpixels, rectangular superpixels, and a combination of rectangular and square superpixels to split and concentrate the incoming light. The efficiency

of each phase plate was analyzed in terms of concentration and splitting capabilities. The results revealed the superior performance of the rectangular superpixels in attaining our purpose. Upon achieving a superior performance when using rectangular superpixels, we used these superpixels to optimize the phase plate for the angle-independent SpliCons. The applied experimental optimization algorithm is explained in detail.

The experimental setup used for the study is demonstrated, where the SpliCons are emulated using a programmable phase-only spatial light modulator to mimic the thickness variations of the SpliCon at any specific position corresponding to the phase difference of the incoming light at that position. The experimental method of this study provided the ability to design and optimize angle-independent SpliCons for solar energy applications, which is much faster than numerical methods. The angular response of the SpliCons is obtained over the acceptance angle of the system (4.2°), where a motor control mirror is used to manipulate and control the incident angle of the incoming light. We compared the angular response of our SpliCon with a conventional DOE, to clearly demonstrate its superior performance. The Enhancement of these two DOEs is compared. We have observed a superior angular response over the acceptance angle of our experimental setup.

2.2 Experimental Setup

To conduct our experiments, we initially designed and prepared a two-path setup. However, a critical challenge emerged in utilizing this configuration was the simultaneous observation of two distinct regions within the field of view of the charge-coupled device (CCD) camera. This limitation arose due to the relatively small size of the camera chip, which restricted its ability to capture both regions concurrently. Notably, this issue could not be resolved solely through optical alignment. Consequently, we opted to modify our experimental setup by transitioning to a single-path configuration, effectively mitigating this limitation and ensuring more reliable data acquisition.

In our single-path setup (Figure 2.1) a fiber-coupled Quartz Tungsten-Halogen broad-

band white light source (THORLABS SLS201L) that emits light with a wavelength between 360-2600 nm is utilized. The light source delivers a blackbody-type spectrum at 2796 K with a Fiber coupled optical power of 10 mW. Along the optical path, a neutral density filter (ND) is placed to avoid the saturation of the incident beam and to prevent damage of high-intensity light to the CCD camera.

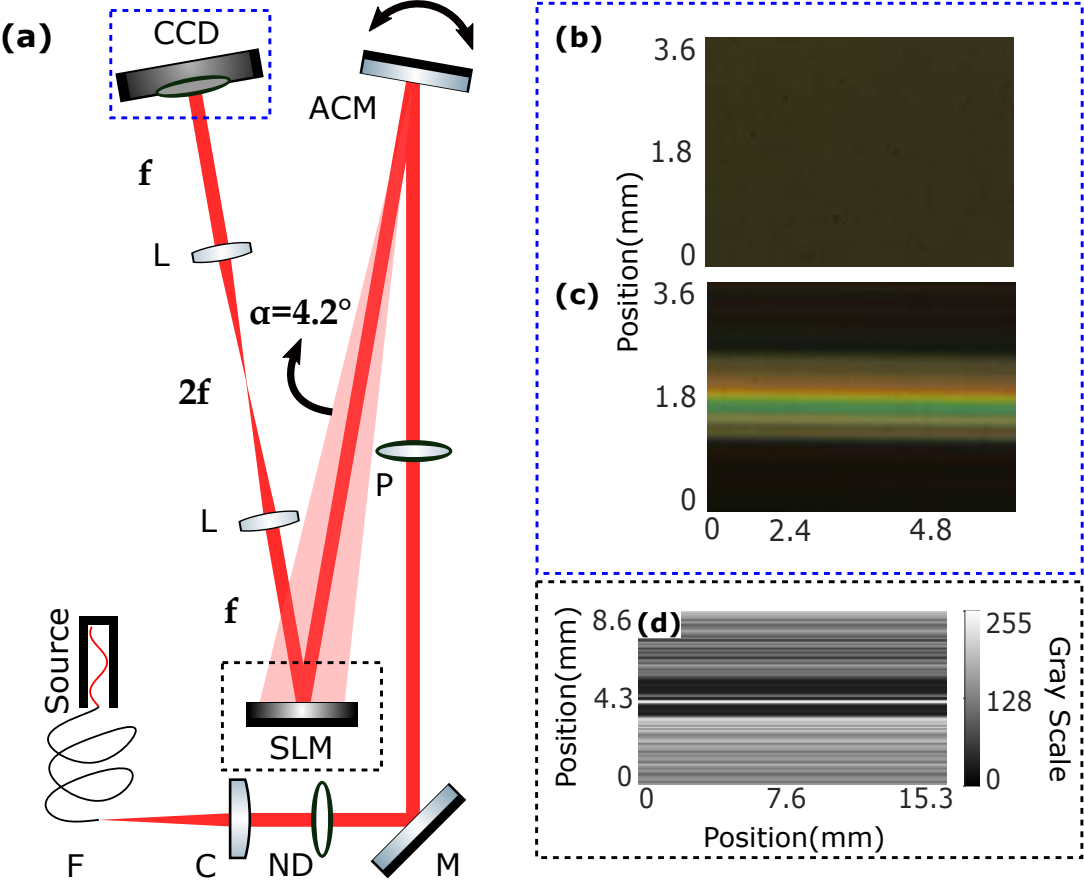


Figure 2.1: (a) Schematic of the optical system used to emulate SpliCon using an SLM. (The optical system consists of a fiber (F), a plano convex lens (C), neutral density filter (ND), mirrors (M), a polarizer (P), an actuated controlled mirror (ACM), and converging lenses (L)), (b) Image on the CCD camera before optimization, (c) Image showing simultaneous spectrum-splitting and concentration on the region of interest after optimization, (d) Phase pattern of the SLM which splits and concentrates the light.

A Holoeye Pluto-2.1 phase-only liquid crystal on silicon SLM with an active area of 15.36×8.64 mm (0.7" diagonal), a resolution of 1920×1080 pixels and a pixel size of

8 μm is used to modulate the incident beam. As a liquid crystal-based device, SLM enables a high-resolution, high-speed phase and amplitude modulation through independently controlled pixels or Superpixels. The light beam has been shaped dynamically using a computer interface, optimizing light utilization based on pixel count and control. Since liquid crystals modulate specific wavelengths, SLM may have different specifications, such as pixel size, operating wavelength, and anti-reflective coatings. We used a wire grid polarizer is used to eliminate the polarization axis that cannot be modulated by the SLM. The whole setup is controlled using a LabVIEW program.

A 4f system with two converging lenses is set to reflect the image on the surface of SLM to the CCD camera (Guppy PRO F-125C) with a pixel size of 3.75 μm and a resolution of 1292 \times 964 pixels. The chip of the multi-channel CCD camera (Sony ICX445) has red, green, and blue channels with peak quantum efficiencies at 610 nm, 535 nm, and 450 nm, respectively. The incident angle on the SLM is controlled by a servo motor-controlled mirror (Thorlabs Kinesis K-Cube) which sweeps angles in the range of 13.4°. Considering the size of our SLM and its distance from the motor-controlled mirror, only a portion of the SLM is illuminated by the incoming light, which sets the acceptance angle to 4.2° (Additional details regarding the measurement of the acceptance angle for the system is given the subsequent section).

Figure 2.1(a) illustrates the schematic of the experimental setup to emulate SpliCon using an SLM. The intensity distribution before the light modulation is observed in Figure 2.1(b). We spectrally split and concentrate the light on the target positions as depicted in Figure 2.1(c). The target arrays are located from 0.8 mm to 1.4 mm for the red channel and 1.4 mm to 2 mm for the green and blue channels in the transverse axis. The intensity distributions for channels are observed in the desired positions, indicating both the concentration and spectral splitting as is obvious in the camera image in Figure 2.1(c). Figure 2.1(d) represents the optimized SLM pattern to achieve angle independent spectral splitting and broadband light concentration. We performed the optimization using stripes that elongate through the longitudinal axis of the SLM surface. As a result, the SpliCon is angle independent along the strips.

It is worth to be mentioned that, in PV systems, a lens is generally used to focus or collimate the light before it reaches to the DOE, allowing for greater control over the

direction and intensity of the light reaching the solar panel. However, in our setup, the role of the condenser lens before the SLM is to improve the efficiency of the lighting system. The role of the condenser lens is not to perform any light control before the SLM. It is placed in front of the halogen lamp to collect and focus scattered light rays and improve the overall efficiency of the lighting system. The role of the 4f system, which is located after the SLM, is to direct the light from SLM to the CCD camera. Therefore, we do not perform any light manipulation and control before SLM. It should also be noted that, in real applications, the intensity of the Sun is sufficiently large not to require concentration before the SLM. Therefore, no additional optics are required to implement the SpliCons.

The real optical system for experimental optimization is shown in Figure 2.2. The setup consists of the following components:

- A Quartz Tungsten-Halogen fiber-coupled white light source that emits light with a wavelength between 360 nm - 2600 nm
- A phase-only SLM with a nominal resolution of 1920×1080 pixels
- A multi-channel CCD camera with 1292×964 pixels and a pixel size of $3.75\mu\text{m}$.
- An ND filter to reduce the light intensity and avoid any possible damage to the camera
- A converging lens ($f=150$ mm)
- A plano-convex lens ($f = 100$ mm)
- Polarizer
- Motor controlled Mirror
- Mirrors

We ensure the precision and reliability of our experimental setup by implementing a careful calibration procedure for both the SLM and the CCD camera. To reduce the impact of noise on individual pixels, superpixels are used by grouping adjacent pixels, which makes the analysis more resilient to noise-induced inaccuracies in individual

pixel measurements. There are several advantages of using superpixels instead of single pixels in the optimization process. Firstly, the usage of superpixels reduces computational complexity, as it decreases the number of elements that are needed to be processed and analyzed. This, in turn, makes denoising and other image-processing algorithms more efficient [76]. Secondly, when grouping multiple pixels to a superpixel, random noise variations in individual pixels tend to cancel each other out, resulting in a smoother signal [77]. Finally, as Superpixels increase the effective area for intensity measurement, they result in an improved Signal-to-Noise Ratio [78].

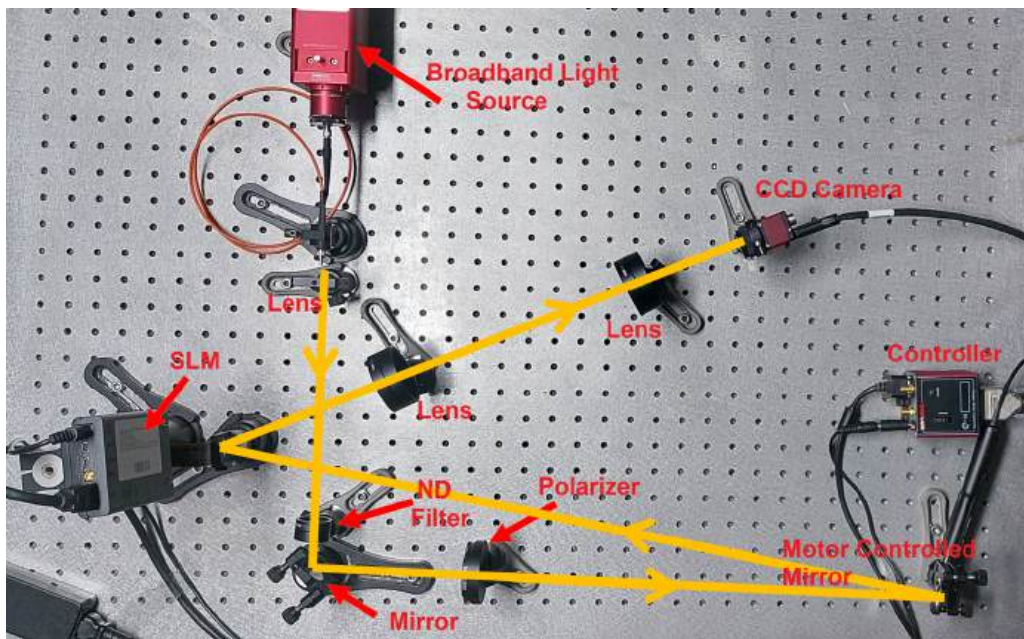


Figure 2.2: Real optical system

We also systematically employ control experiments to identify and mitigate potential errors within the setup. Moreover, we take measures to minimize environmental influences by rigorously controlling the humidity and temperature of the testing environment. Precise alignment of the optical components is carried out to reduce misalignment errors and optimize the accuracy of the system. Our methodology involves the execution of multiple trial runs, serving to validate the consistency of our obtained results. This approach ensures the repeatability and reproducibility of our experimental findings, thereby reinforcing the robustness and credibility of the outcomes.

2.3 Measuring the Acceptance Angle

Figure 2.3 schematically illustrates the measurement of the acceptance angle of our system.

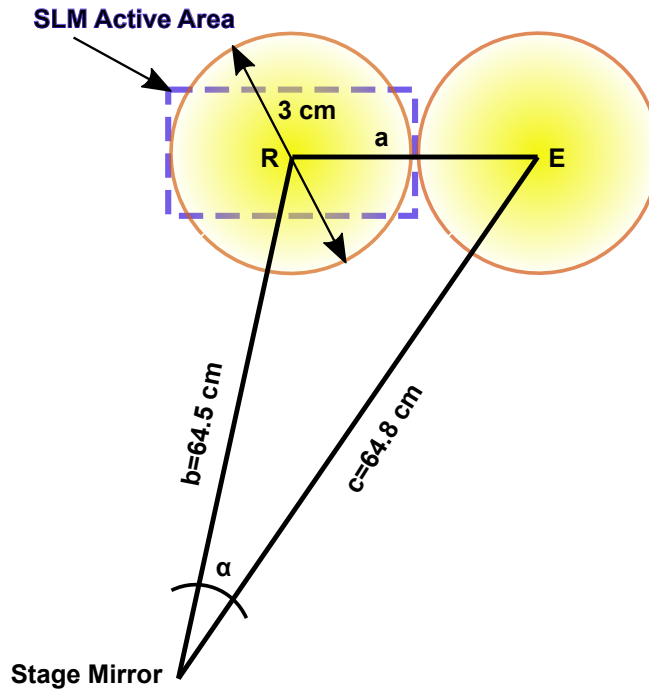


Figure 2.3: Measuring the acceptance angle of the system

The light beam incident on the SLM covers 12.54° in total. We change the angle by moving the mirror attached to the Thorlabs Kinesis K-Cube. Since the light beam incident on the SLM is a large circular-shaped beam with a diameter of 3 cm, we consider the reference point (R) as the center of the circle. We track the movement of the center point of the circle to measure the angle. When the beam is centered around the surface of the SLM, point R is also at the center of the SLM surface. Kinesis K-Cube is moved at 0.1 mm intervals until the beam completely exits the SLM surface with the beam center denoted by point E. This movement creates a triangle between the motor-controlled mirror, the center point of the SLM surface and the center point of the beam as it exits the SLM. Each 0.1 mm movement of Kinesis K-Cube results in a 0.3° change according to Eq. (2.1), considering the distance between the motor-controlled mirror and point R (b), the motor-controlled mirror and point E (c), and point R and point E (a). The light beam starts illuminating the SLM surface at 1.1

mm and exits completely at 2.5 mm. As a result, the SLM surface is illuminated for 14 increments meaning an angle of $14 \times 0.3 = 4.2^\circ$.

$$\alpha = \arccos \left((b^2 + c^2 - a^2) / 2bc \right) \quad (2.1)$$

2.4 Wavefront Shaping-Light Shifting

In order to achieve the goal of spectrum-splitting and concentration of the broadband light, we started by shifting the light to the specific portions of the CCD camera (target area). At the first attempt, we aimed to shift the light to the top portion of the camera. For this purpose, we created a blazed grating phase plate with diagonal strips (Figure 2.4(a)) using Holoeye software.

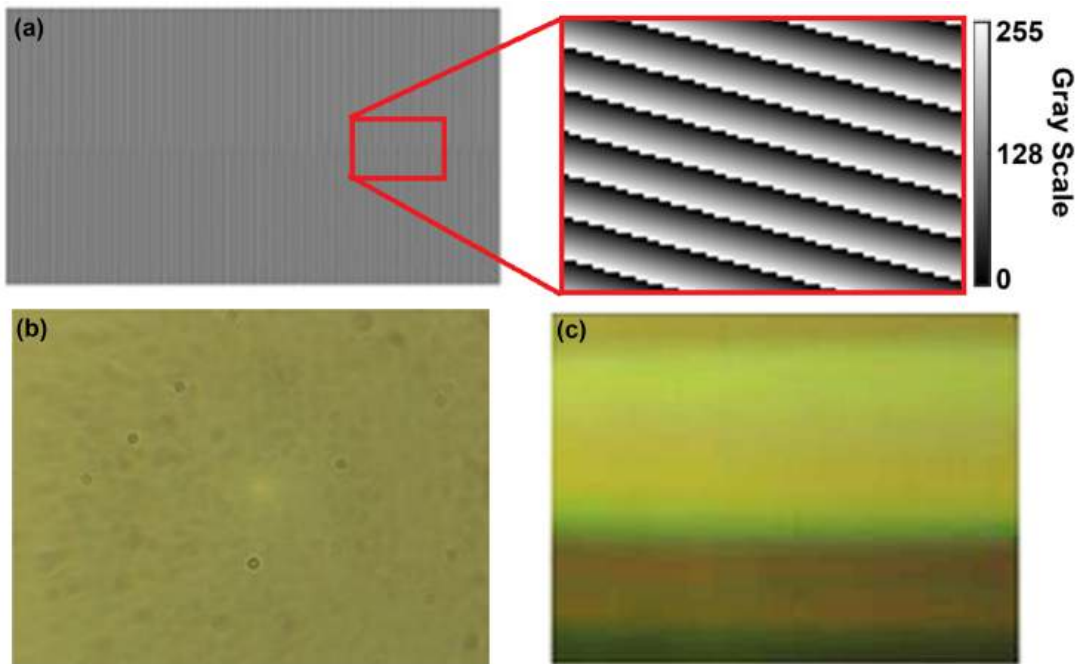


Figure 2.4: (a) The blazed grating phase plate generated by Holoeye software and used to shift the light to the uppermost portion of the CCD camera, (b) The image on the CCD camera before the application of phase plate, (c) Image recorded on the CCD camera showing the shifted light to the uppermost portion of the camera.

This pattern, also called Echollette grating, is a type of diffraction grating where the

grooves are asymmetrically shaped, typically forming a saw-tooth intensity profile rather than a purely sinusoidal one. The blazed grating has been used extensively as a fundamental optical part of spectrometers to reflect most of the incoming light in one particular diffraction order [79]. The image before applying the phase plate has been shown in Figure 2.4(b) for comparison. The generated blazed grating pattern has been loaded to the SLM and the image on the CCD camera has been recorded as illustrated in Figure 2.4(c). A clear shift to the upper most portion of the CCD camera can be clearly distinguished from Figure 2.4(c).

After shifting the light to the top portion of the CCD camera, we have changed our target area to the lower portion. To do that we generated a new phase plate with diagonal strips but having different strip artifacts. The generated phase plate and associated image on the CCD camera has been shown in Figure 2.5. Again, a clear shift to the lowermost portion of the CCD camera can be clearly distinguished from Figure 2.5(b).

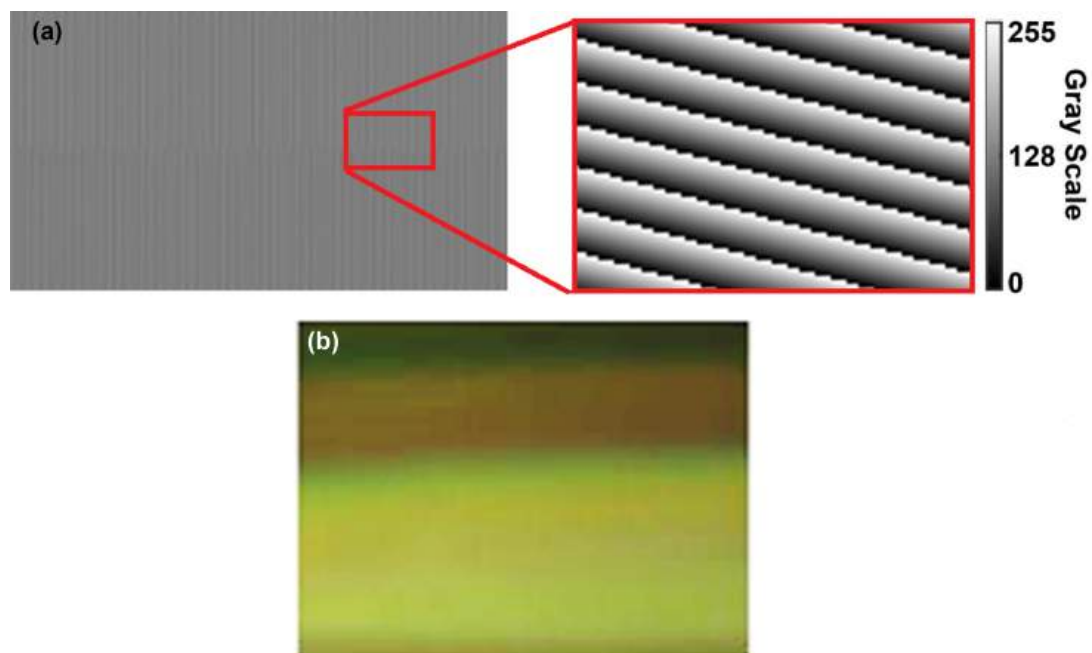


Figure 2.5: (a) The blazed grating phase plate generated by Holoeye software and used to shift the light to the lowermost portion of the CCD camera, (b) Image recorded on the CCD camera showing the shifted light to the lower portion of the camera.

To achieve light shifting toward the central region of the CCD camera, we devised an

approach that involved combining the two previously developed phase patterns. By integrating these patterns, we aimed to leverage the strengths of each configuration to achieve a more balanced spectral distribution while maintaining effective concentration. The combined phase pattern was systematically analyzed to assess its impact on the spatial redistribution of light, ensuring that the intensity across all red, green and blue (RGB) channels was optimized. The combined phase plate and resulting image on the CCD camera can be seen in Figure 2.6(a) and Figure 2.6(b), respectively.

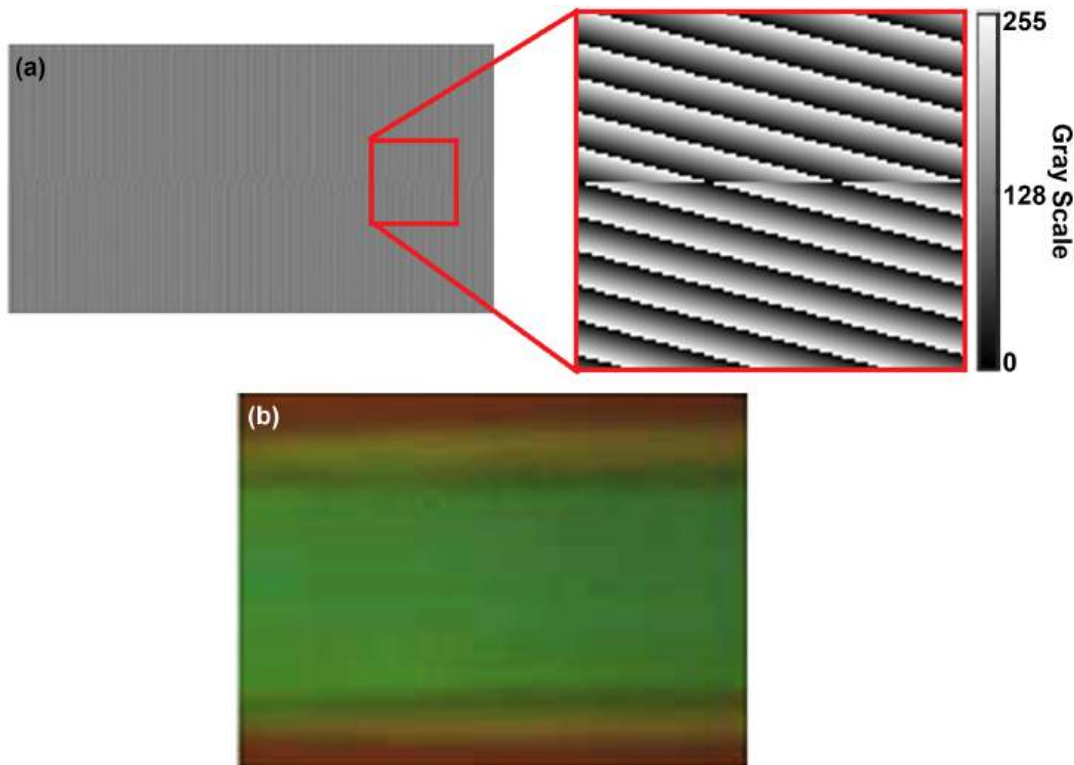


Figure 2.6: (a) The combined phase plate used to shift the light to the central region of the CCD camera, (b) The image obtained on the CCD camera after using combined blazed grating phase plate.

In order to further investigate the resulting image, we analyze the image to obtain the normalized intensity for RGB colors. To achieve this, we normalize the image captured by the CCD camera after applying the phase plate against the image taken before its application. We obtain the results along the vertical axis of the image (Y-axis). The normalized intensity for different colors can be seen in Figure 2.7.

As illustrated in Figure 2.7, the use of a combined blazed grating pattern, incorpo-

rating diagonal strip patterns, resulted in a significant enhancement in the intensity of the green color. Additionally, a slight improvement was observed in the intensity of the blue color, suggesting a partial optimization of the spectral redistribution. However, the intensity of the red color within the region of interest (ROI) exhibited a substantial reduction. This indicates that the current phase plate configuration does not achieve an optimal balance for the simultaneous concentration of all RGB color channels, necessitating further refinement.

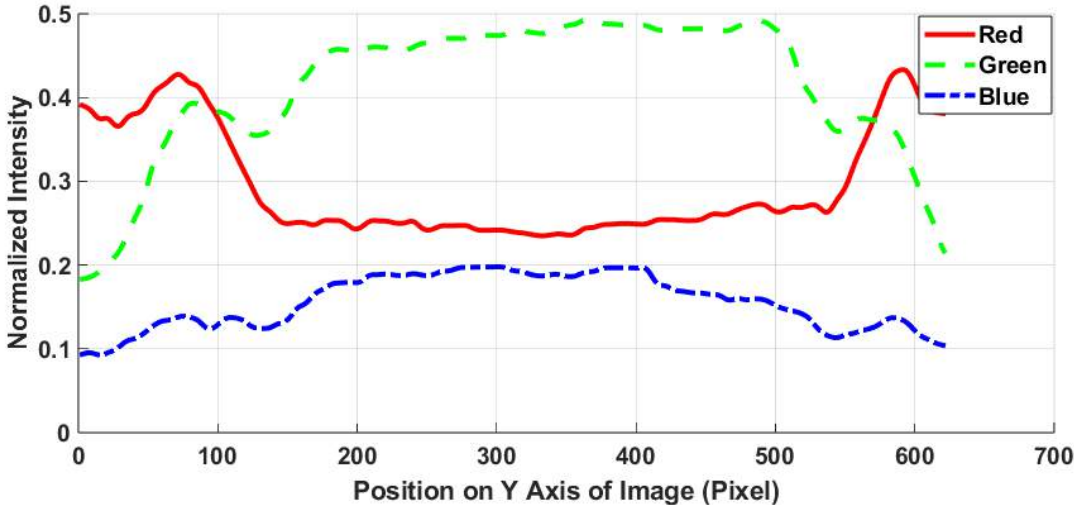


Figure 2.7: The normalized intensity for red, green and blue channels using combined blazed grating phase plate.

To address the limitations we faced when using combined blazed grating, we utilized the combined pattern as a background pattern and systematically modified the middle portion of the phase plate. This adjustment aimed to achieve a more uniform spectral distribution while maintaining the efficiency of the spectrum-splitting and concentration mechanism. By reprogramming the phase plate, we sought to optimize phase modulation parameters, ensuring that all three color channels—red, green, and blue—were concentrated effectively within their designated regions. The refined approach aims to enhance the spectral splitting efficiency and improve the overall performance of the optical system in light restructuring and angular stability. Further experimental validation and iterative refinements were performed to assess the impact of these modifications on spectral concentration and overall system performance.

2.5 Wavefront Shaping-Concentration

The pattern obtained by combining two blazed grating patterns (Figure 2.7) has demonstrated the ability to concentrate blue and green colors while significantly reducing the intensity of the red color, without achieving spectral splitting.

To achieve finer control over the pattern design and overcome the limitations of the Holoeye software in generating customized patterns, we opted to use the LabVIEW program for pattern generation. Subsequently, we applied an optimization algorithm (further details will be provided in the next section) to refine the gray levels of the square superpixels, enhancing the precision of light modulation. It is worth mentioning that the optimization algorithm can also be extended to the entire phase plate, allowing for a continuous and sequential determination of the optimal gray level values for each pixel or a group of pixels (superpixels). This approach ensures a systematic and adaptive optimization process, improving the efficiency of spectral splitting and concentration. The algorithm referred to as the Continuous Sequential Optimization Algorithm, enables real-time adjustments to maximize performance while maintaining computational efficiency.

In this approach, we explored variations in the width of the region containing square superpixels. Specifically, we experimented with different ratios of the square superpixel area to the total SLM area, testing proportions of 1/4, 1/5, 1/7, and 1/10. The concept is schematically illustrated in Figure 2.8.

An example of the generated phase plate with square superpixel-to-total SLM ration of 1/7 has been illustrated in Figure 2.9(a). The image captured on the CCD camera for this phase plate has been shown in Figure 2.9(b). The graph in Figure 2.9(c) illustrates the normalized intensity distribution along the Y-axis for the red, green, and blue color channels, revealing how the combined blazed grating with a central superpixel region influences light modulation.

As it can be seen in Figure 2.9(c), a distinct peak appears at the center, corresponding to the superpixel-modulated area, where light is most concentrated. The green channel exhibits the highest intensity, followed closely by the red channel, while the blue channel shows a lower response, suggesting that the modulation is more effec-

Blazed Grating
Square Superpixel Region

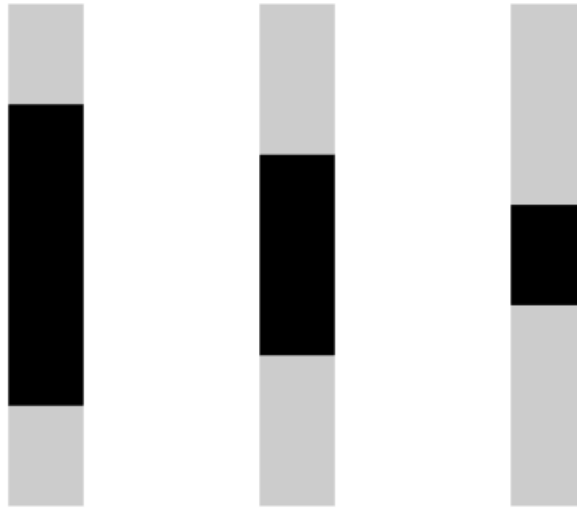


Figure 2.8: Schematic representation of the proposed design, integrating a combined blazed grating (gray region) with a central square superpixel region (black). Different configurations illustrate variations in the width of the square superpixel region relative to the total SLM area.

tive for longer wavelengths. This spectral dependence may result from wavelength-dependent diffraction or phase modulation effects introduced by the superpixel structure. The slight asymmetry and broadening in the intensity curves, especially for red and green, indicate potential phase shifts or diffraction spreading, whereas the lower and more uniform intensity outside the central region confirms that the surrounding blazed grating does not significantly enhance light concentration. Overall, the results highlight the superpixel region's ability to enhance intensity with noticeable wavelength-dependent variations, making it particularly effective for modulating specific spectral components.

In order to analyze the effect of the square superpixel-to-total SLM area ratios on light enhancement, Table 2.1 presents the enhancement factors for different ratios across the red, green, and blue color channels. The enhancement factor quantifies the intensity increase due to the presence of the superpixel structure. As the ratio decreases, the enhancement values vary across different color channels, indicating a

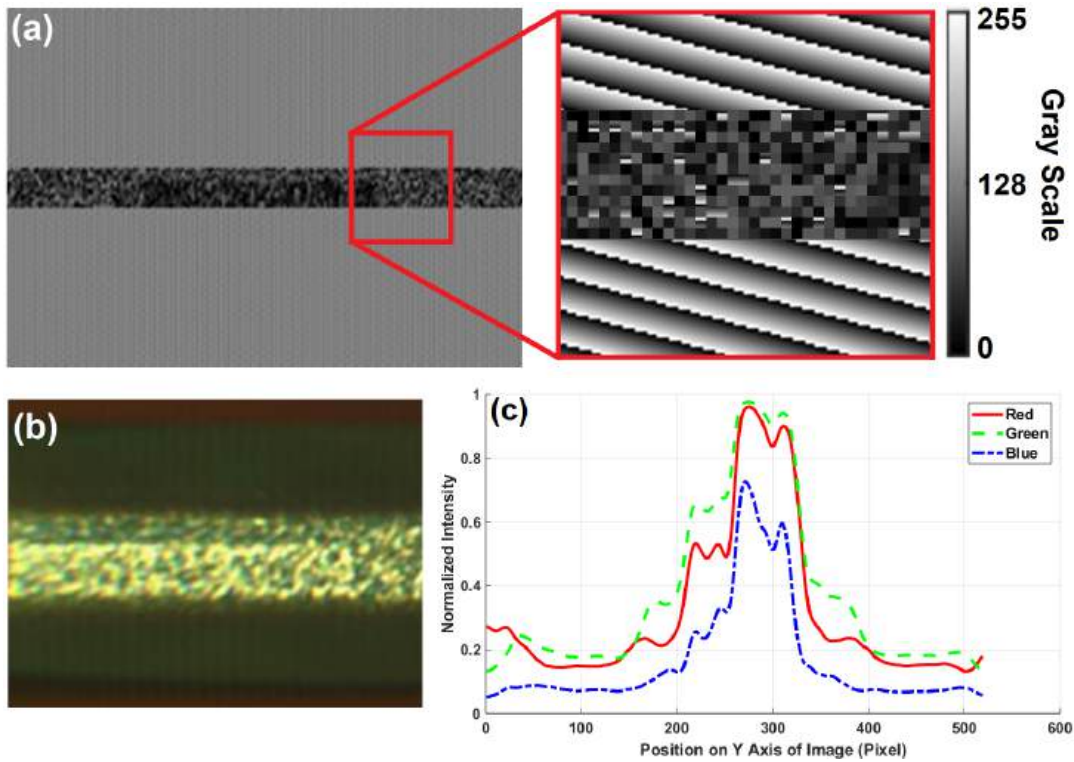


Figure 2.9: (a) A combined blazed grating with a superpixel region at the center, displayed in grayscale. The inset provides a magnified view of the central superpixel-modulated area, (b) The corresponding experimental image captured on the CCD camera, showing the effect of the superpixel region, (c) Normalized intensity profiles along the Y-axis for red, green, and blue channels, highlighting the modulation effects introduced by the superpixel region.

wavelength-dependent modulation effect. The results suggest that certain ratios favor specific color channels, reflecting the influence of the superpixel design on spectral light distribution.

In an attempt to further improve the light concentration at the region of interest, we have tried to use rectangular superpixels as a background phase plate combined with square superpixels at the middle. The phase plate has been shown in Figure 2.10. The comparison between the combined blazed grating with a central square superpixel region (Figure 2.9) and the rectangular background superpixel structure with embedded square superpixels (Figure 2.10) demonstrates that the latter offers superior light modulation performance.

Table 2.1: Enhancement Factors Corresponding to Various Square Superpixel-to-Total SLM Area Ratios

| Square Superpixel to SLM Ratio | Enhancement | | |
|-----------------------------------|-------------|-------|------|
| | Red | Green | Blue |
| 1/4 | 1.30 | 1.27 | 1.19 |
| 1/5 | 1.21 | 1.30 | 1.22 |
| 1/7 | 0.97 | 1.08 | 1.15 |
| 1/10 | 1.17 | 1.26 | 1.31 |

The intensity profile in Figure 2.9 exhibits sharp peaks with abrupt variations, especially in the blue channel, indicating strong localized enhancement but also significant spectral imbalance due to wavelength-dependent diffraction. In contrast, Figure 2.10 shows a more gradual and uniform intensity transition, providing better control over spatial light distribution. Additionally, the rectangular superpixel structure results in more balanced enhancement across the red, green, and blue channels, reducing chromatic dispersion effects observed in the blazed grating case.

The structured pattern in Figure 2.10 allows for finer spatial control, leading to a more stable and evenly distributed intensity modulation, whereas the blazed grating introduces stronger diffraction artifacts and spectral fluctuations. Overall, the transition to a rectangular superpixel background with square superpixels improves intensity stability, spectral uniformity, and spatial control, making it a more effective approach for structured light modulation. Therefore, we came into the conclusion that we can achieve the goal of our research using rectangular superpixels. In the following sections we will explain in detail how we achieved the optimized angle independent SpliCons. We will start with the optimization algorithm followed by the results of optimization.

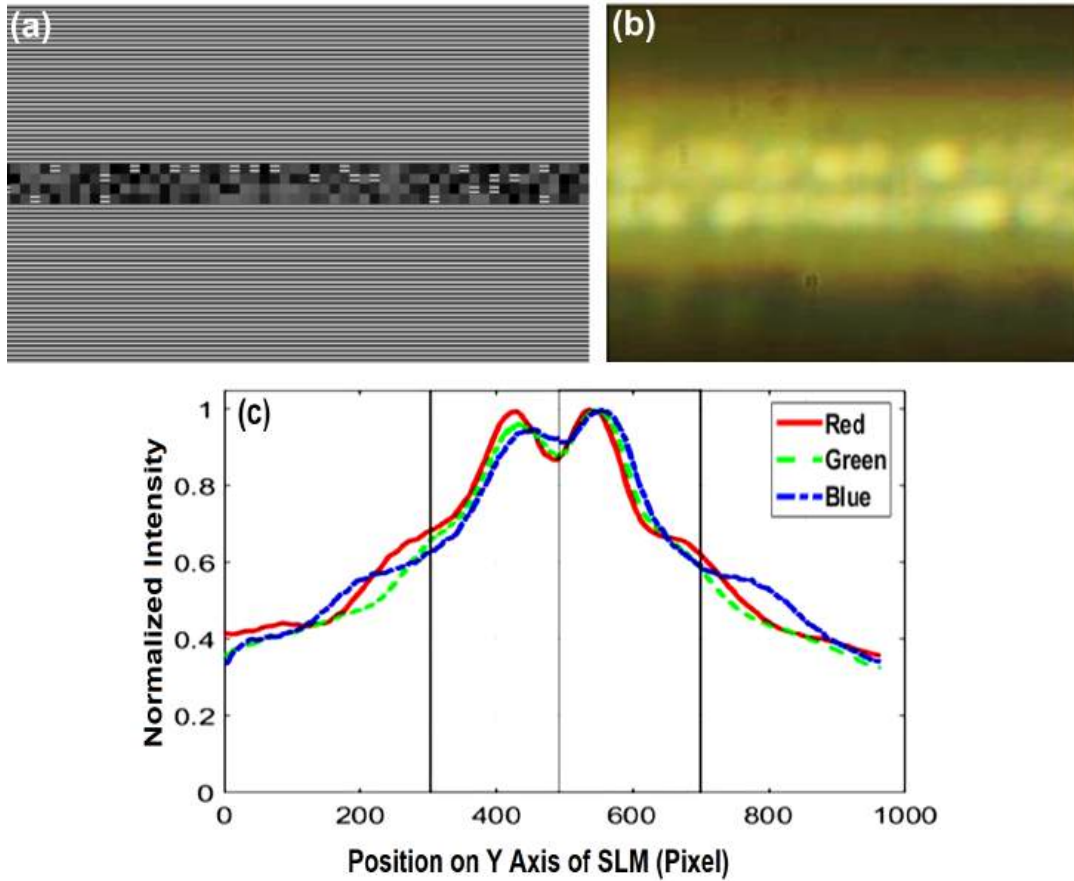


Figure 2.10: (a) Combined background rectangular superpixels with square superpixels at the middle of the phase plate, (b) Corresponding raw image on the CCD camera (c) The normalized intensity for red, green and blue channels along Y-axis of the image

2.5.1 Optimization Algorithm

The calculation of a SpliCon can take up to 89 days [3] for each wavelength between 400-1100 nm since the optimization of SpliCon includes a Fourier transformation of the phase pattern at every step. Instead, we have shown that experimental optimization provides an overwhelming advantage since the Fourier transformation is taken care of by the lenses that provide an optical computation of the response of the phase patterns at the speed of light. Experimentally, the optimization time is limited by the refresh rate of the SLM, the camera exposure time, and the number of iterations. The image captured by the CCD camera is directly affected by each pixel present

on the SLM. However, modifying individual pixels on the SLM does not produce a detectable difference in the captured images, because the change caused by a single pixel is insignificant and does not surpass the noise threshold [80].

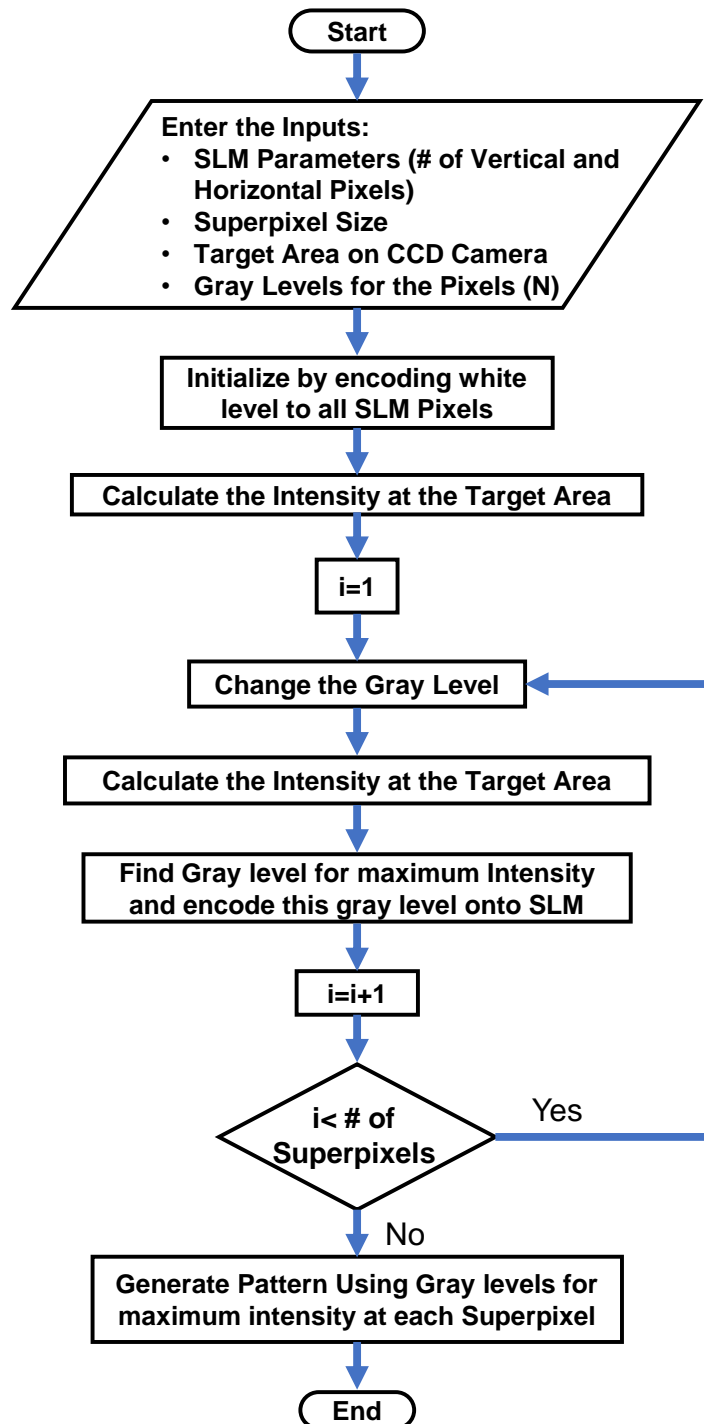


Figure 2.11: Flowchart of the experimental optimization method

As a result, we group and control pixels on the SLM surface as superpixels. In our algorithm (given in Figure 2.11), we used rectangular superpixels (strips) instead of square superpixels. Rectangular superpixels have shown superior performance over square superpixels as they elongate through the longitudinal axis of the SLM surface and remain angle independent along the strips. One rectangular superpixel consists of 1×1920 pixels, a single pixel of the SpliCon. We use 8-bit gray levels ranging from pure white to jet-black to feed the superpixels. We have divided the gray levels on the SLM into 16 steps.

The process of phase optimization of a superpixel has been performed in a sub-iteration step, which is referred to as scanning through 16 gray-level steps on a superpixel and measuring the resulting output intensity pattern at the target. At the end of the optimization, we acquire a phase pattern for each superpixel with a total of 1080×1 superpixels which is called the main iteration. The working principle of the algorithm is based on encoding 8-bit gray values to each superpixel, and measuring the intensity of the image on the CCD camera according to the corresponding gray value. As the gray values are divided into 16 steps on the SLM surface and we have 1080 superpixels, we process $1080 \times 16 = 17280$ parameters. We start with a flat phase on the SLM surface indicating that there is no modulation of the wavefront. Gray values are encoded to each superpixel sequentially, and the phase step that gives the maximum intensity value on the target region is encoded to the SLM surface. After all superpixels are scanned sequentially, an SLM phase pattern is provided which takes only 80 minutes to optimize a SpliCon. The phase pattern after completing the optimization process have been shown in Figure 2.12.

2.6 Results of the Optimization

After we obtained the optimized phase plate given in the Figure 2.12, we loaded the pattern into the SLM to investigate its spectrum-splitting and concentration capabilities. The raw image captured on the CCD camera has been shown in Figure 2.13 (a). The normalized intensity distribution along the Y-axis of this image has been shown in Figure 2.13(b). We have observed a successful simultaneous spectrum-splitting and concentration using our optimized pattern with rectangular superpixels. As it can



Figure 2.12: The phase plate after optimization using rectangular superpixels

be seen in Figure 2.13(b), for the target area denoted by Red, we observe a peak for the red color, while the other two colors have lower intensity profiles. The same phenomenon can also be seen in the target area specified by Green and Blue. In this area the green and blue colors have their maximum intensity profiles, while red colors intensity is low. indicating we are achieved our goal.

A replot of raw images of Figure 2.1(b) and (c) are shown in Figure 2.14, which quantitatively expresses the intensity changes for different frequency bands. The intensity profiles before and after wavefront shaping captured by the CCD camera are shown in Figure 2.14(a) and (b), respectively.

The results are normalized to the un-optimized (flat phase) phase pattern. Therefore, the features of the Fresnel reflections are also normalized in our results. Figure 2.14(c) illustrates the differential change in the intensity ($\Delta I^k(\lambda)$), which is used to indicate the increase in the intensity by our optimized SpliCon. We define the differential change in the intensity as:

$$\Delta I^k(\lambda) = \frac{I_f^k(\lambda) - I_i^k(\lambda)}{I_i^k(\lambda)} \quad (2.2)$$

where the scalar-valued function $I^k(\lambda)$ shows spectral intensity values at pixel number k (taking values of $\{1, 2, \dots, N\}$). The initial and final intensities are denoted by subscripts i and f , respectively.

The differential intensity changes of the desired wavelengths of red (560-875 nm),

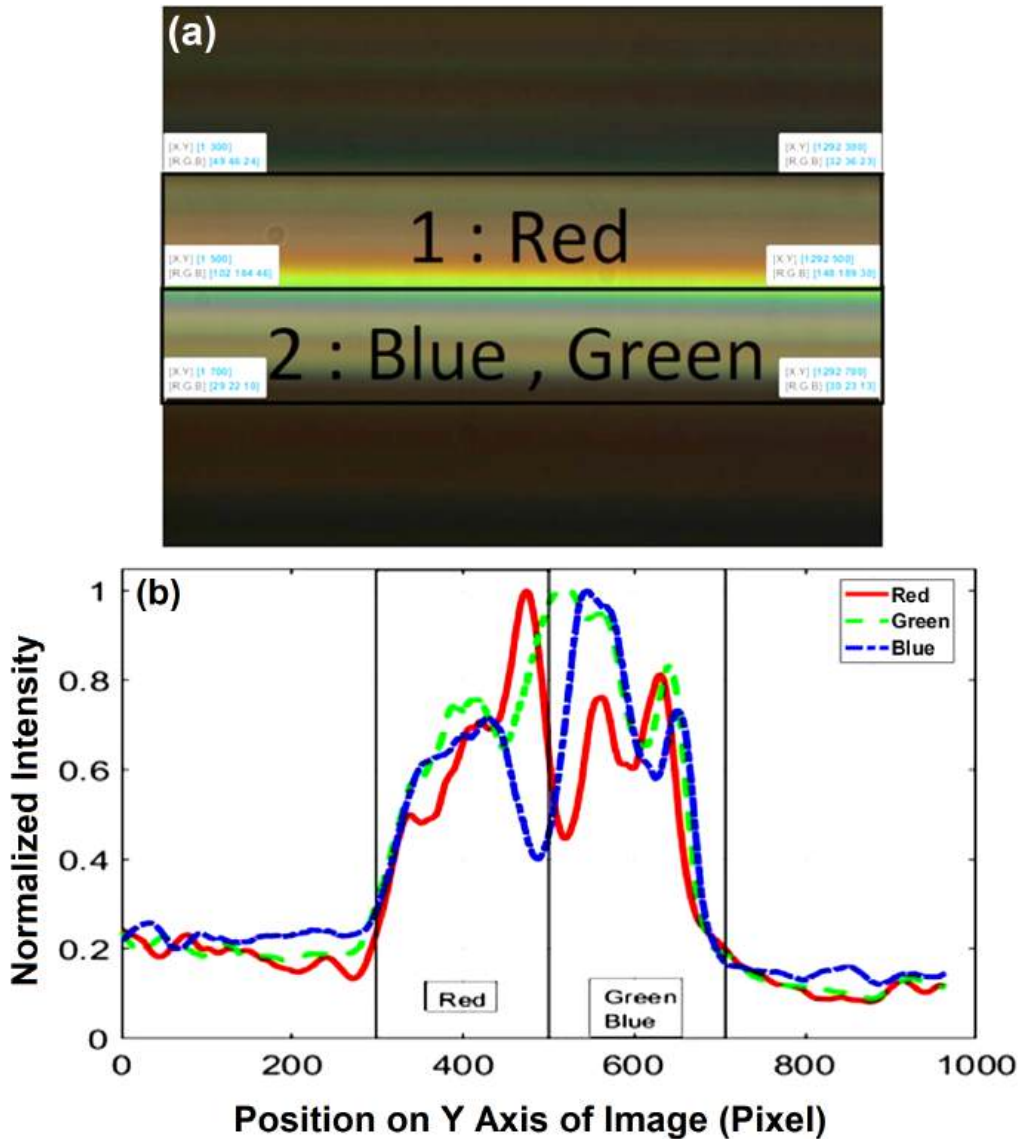


Figure 2.13: (a) The raw image on the CCD camera using optimized phase plate with rectangular superpixels, (b) The normalized intensity using optimized phase plate with rectangular superpixels, showing successful simultaneous spectrum-splitting and concentration.

green (425-620 nm), and blue (420-535 nm) channels are shown in Figure 2.14(d-f). In our optimization algorithm, the red band is directed to a rectangular area of (1920×200 Pixels) located in the upper half of the target plane Figure 2.14(d). The green and blue bands are directed to a rectangular region with the same dimensions located at the lower half of the target plane (Figure 2.14(e) and (f)). The intensity

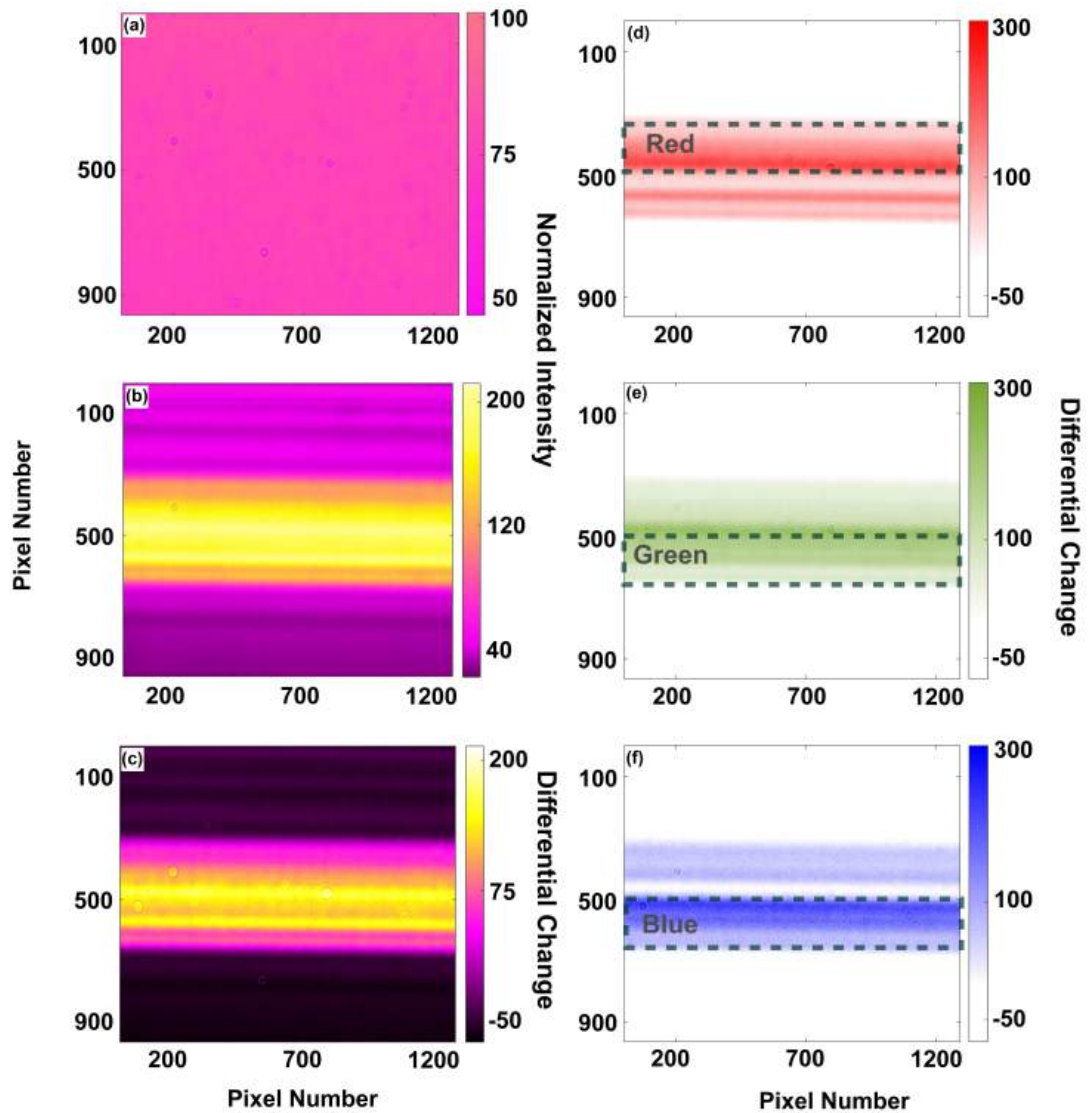


Figure 2.14: The intensity profiles for combined color channels (a) before (b) after optimization. (c) Differential intensity changes for combined color channels, Differential change for separate colors (d) Red, (e) Green and (f) Blue. The dashed lines indicate the target areas in which the colors are concentrated. The green and blue bands are directed to a rectangular region with the same dimensions at the lower half of the target plane.

increase for each band can be clearly distinguished from Figure 2.14(d-f), which indicates the success of the designed SpliCon for the simultaneous spectral splitting and concentration of the broadband incident light. Although the red channel is targeted in the upper half of the target plane, an increase in the intensity of the red light in

the lower half is observed. This can be mainly attributed to the overlapping quantum efficiency of color channels of the CCD camera. At 5% quantum efficiency, the CCD chip's red and green bands have 29.3% overlap. The overlap increases to 66.7% between the green and blue bands [47]. Therefore, we have directed green and blue bands to the same target area. Nevertheless, for all channels, a spectral splitting ratio larger than 0.5 has been observed. For each channel, the enhancement factor $\eta(\lambda)$ is calculated by dividing the intensity after splitting and concentration (I_f) by the initial intensity (I_i) at the target region using Eq. (2.3), where A_m is the area of the m^{th} target region, where $m = \{1,2\}$.

$$\eta(\lambda) = \frac{\int_T I_f(A_m, \lambda) dA_m}{\int_T I_i(A_m, \lambda) dA_m} \quad (2.3)$$

Applying Eq. (2.3), the enhancement factor for the red, green, and blue channels is calculated as 202%, 188%, and 204%, respectively.

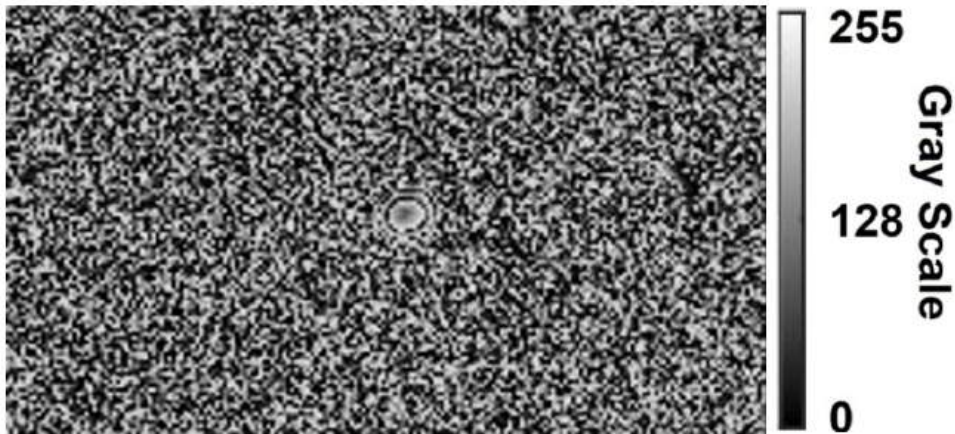


Figure 2.15: The phase plate of a conventional DOE

For different channels, the spectral splitting ratio $S(\lambda)$ is calculated using Eq. (2.4), where the spectral intensity of the target area is divided by the total spectral intensity. In our test setup, splitting is performed on two regions for $m,n = \{1,2\}$, where $m \neq n$. A spectral splitting ratio of 0.58, 0.51, and 0.59 is obtained for red, green, and blue channels, respectively.

$$S(\lambda) = \frac{\int_T I_f(A_m, \lambda) dA_m}{\int_T I_f(A_m, \lambda) dA_m + \int_T I_f(A_n, \lambda) dA_n} \quad (2.4)$$

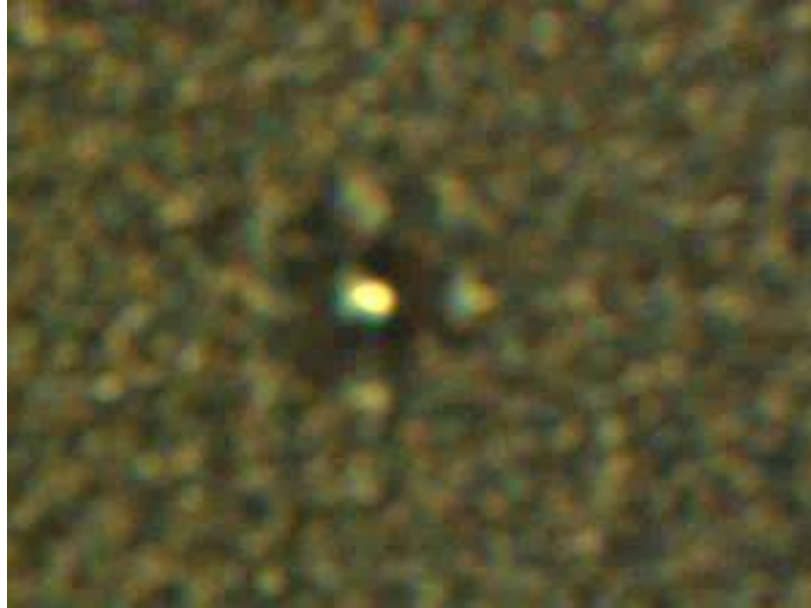


Figure 2.16: The raw image of the conventional DOE on CCD camera

The response of the designed SpliCon has been tested under angled illumination. To do so, a motor-controlled mirror is used to change the angle of the incident light over an acceptance angle of 4.2° , as illustrated in Figure 2.2. We have compared our SpliCon and a conventional DOE using the same setup. The phase plate of the conventional DOE used for comparison has been illustrated in Figure 2.15. For the given phase plate, the raw image captured on the CCD camera has been shown in Figure 2.16.

Figure 2.17 compares the enhancement of our SpliCon and a conventional DOE. It can be seen in Figure 2.17 that the full-width half maximum (FWHM) for our SpliCon is 3.2° compared to an FWHM of 0.66° for the conventional DOE, indicating a superior angle-independent behavior of our SpliCon compared with a conventional DOE over an acceptance angle of 4.2° . The angle-independent behavior of the designed SpliCon has been verified experimentally over the acceptance angle of the setup (4.2°), which was the maximum angle we could test using our setup due to the size of our SLM.

We also tried to investigate the effect of number of iterations on the spectrum-splitting and concentration enhancements in our algorithm. In order to determine the most suitable number of iterations, we have analyzed the maximum values for both en-

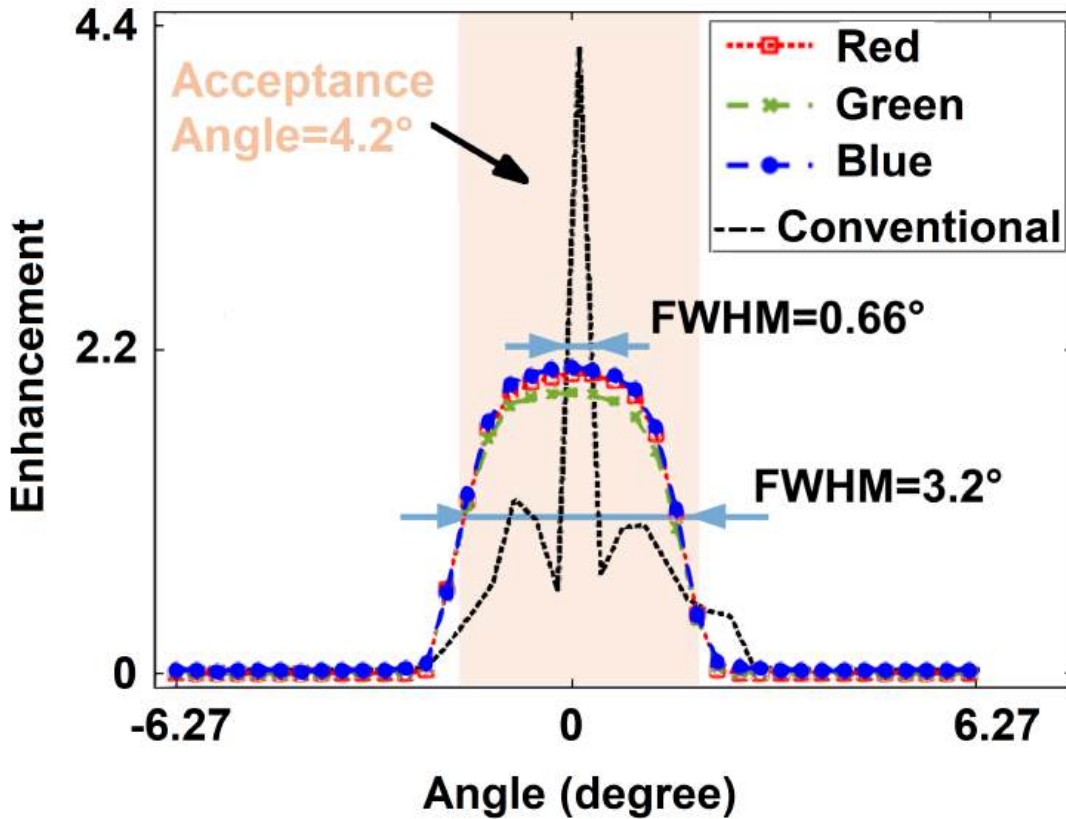


Figure 2.17: Enhancement of angle-independent SpliCon compared with conventional DOE

enhancement values (Table 2.2) and splitting ratio (Table 2.3). The enhancement values for different number of iterations are given in Table 2.2.

The splitting ratio for different number of iterations are summarized in Table 2.3. Taking into account the values reported in Table 2.2 and Table 2.3 the maximum values for the enhancement and spectral splitting ratio can be summarized as follows:

- **The maximum values for enhancement are:**
 - **Red:** 2.0644 at **Iteration 5**
 - **Green:** 1.9656 at **Iteration 2**
 - **Blue:** 2.1094 at **Iteration 2**
- **The maximum values for the splitting ratio are:**

Table 2.2: Enhancement values for different number of iterations

| Number of Iterations | Enhancement | | |
|----------------------|---------------|---------------|---------------|
| | Red | Green | Blue |
| 1 | 2.0187 | 1.8766 | 2.0444 |
| 2 | 2.0065 | 1.9656 | 2.1094 |
| 3 | 2.0584 | 1.9006 | 2.0967 |
| 4 | 1.9997 | 1.9287 | 2.0886 |
| 5 | 2.0644 | 1.9274 | 2.0563 |
| 6 | 2.0374 | 1.8559 | 2.0210 |
| 7 | 2.0249 | 1.8202 | 2.0627 |
| 8 | 2.0234 | 1.7805 | 1.9436 |
| 9 | 2.0385 | 1.8258 | 2.0340 |
| 10 | 1.9853 | 1.9122 | 2.0310 |

Table 2.3: Splitting Ratio for different number of iterations

| Number of Iterations | Splitting Ratio | | |
|----------------------|-----------------|---------------|---------------|
| | Red | Green | Blue |
| 1 | 0.5782 | 0.5036 | 0.5864 |
| 2 | 0.5563 | 0.5166 | 0.5931 |
| 3 | 0.5920 | 0.5102 | 0.5997 |
| 4 | 0.5638 | 0.5116 | 0.5986 |
| 5 | 0.5878 | 0.5166 | 0.5881 |
| 6 | 0.5938 | 0.5047 | 0.5859 |
| 7 | 0.5973 | 0.5031 | 0.6045 |
| 8 | 0.5937 | 0.4954 | 0.5799 |
| 9 | 0.6032 | 0.4983 | 0.5929 |
| 10 | 0.5687 | 0.5144 | 0.5846 |

– **Red:** 0.6032 at **Iteration 9**

– **Green:** 0.5166 at **Iteration 5**

– **Blue:** 0.6045 at **Iteration 7**

To select the best number of iterations, we assign rank scores based on how close an iteration is to the maximum value in each column. The ranking results are summarized in Table 2.4. Based on the Table of ranking, it can be seen that Iteration #2 and Iteration #5 both have the lowest total rank score of 17. Iteration #2 is better for Green and Blue in enhancement but worse for Splitting Ratio. However, Iteration #5 has the maximum Red enhancement and the best Green splitting ratio, making it the most balanced choice.

Table 2.4: Comparison of Iterations for Enhancement and Splitting Ratios

| Iterations | Enhancement | | | Splitting | | | Total Rank |
|------------|-------------------------------|-------------------------------|-------------------------------|-------------------------------|-------------------------------|-------------------------------|------------|
| | Red | Green | Blue | Red | Green | Blue | |
| 2 | 4th (2.0065) | 1st (1.9656) | 1st (2.1094) | 7th (0.5563) | 2nd (0.5166) | 2nd (0.5931) | 17 |
| 5 | 1st (2.0644) | 3rd (1.9274) | 5th (2.0563) | 2nd (0.5878) | 1st (0.5166) | 5th (0.5881) | 17 |
| 9 | 3rd (2.0385) | 6th (1.8258) | 6th (2.0340) | 1st (0.6032) | 6th (0.4983) | 4th (0.5929) | 26 |
| 7 | 6th (2.0249) | 7th (1.8202) | 3rd (2.0627) | 4th (0.5973) | 7th (0.5031) | 1st (0.6045) | 28 |

2.7 Conclusions

In this chapter, angle-independent SpliCons, capable of simultaneously splitting and concentrating broadband light, are reported for the first time. We implement an experimental optimization method for wavefront shaping, demonstrating significantly reduced optimization time compared to computational techniques. In this method, a phase-only SLM is used to emulate the SpliCon, where the thickness variations in

the SpliCon are emulated by controlling and modifying the gray levels in the SLM. Using the optimized SpliCon, we obtain 58%, 51%, and 59% spectral splitting ratios with an enhancement factor of 202%, 188%, and 204% for red (560-875 nm), green (425-620 nm), and blue channels (420-535 nm), respectively. A full-width half maximum (FWHM) of 3.2° has been achieved compared to 0.66° for a conventional DOE within the acceptance angle of the experimental setup of 4.2° . In addition to optimizing spectral splitting and concentration, we explored wavefront shaping techniques to control light distribution dynamically. Through the use of blazed grating phase plates and combined patterns, we demonstrated how light could be selectively shifted across different regions of the CCD camera. However, we observed that while certain configurations enhanced specific colors, they also introduced spectral imbalances. To address this, we refined our approach by modifying the middle portion of the phase plate, leading to a more uniform spectral distribution while maintaining efficient splitting and concentration. Furthermore, our study investigated the impact of iteration count on spectral splitting and concentration enhancements. By analyzing enhancement values and splitting ratios across multiple iterations, we identified 5 iterations as the most balanced choice, offering the highest enhancement for the red channel while maintaining strong performance in the green and blue channels. This result underscores the importance of selecting an optimal iteration count to maximize efficiency while minimizing computational complexity.

CHAPTER 3

CALCULATING SPLICON'S RESPONSE FOR WIDE INCIDENT ANGLES

3.1 Theory of Fourier Optics

The propagation of light through amplitude- or phase-modifying optics with feature sizes on the order of a wavelength involves self-interference based on the wave nature of light. Consequently, the irradiance pattern that emerges exhibits complexities that cannot be fully captured by ray-tracing methods alone. Huygens, a seminal figure in diffraction theory, explained this behavior by representing the illuminating field as a collection of secondary point sources, termed “wavelets,” located at the aperture. These wavelets emit spherical phase fronts, with amplitude-modifying DOEs selectively blocking some wavelets, and phase-modifying DOEs present relative phase delays among them [81].

When the distance of the output plane (observation plane) is sufficiently large, the spherical wavefronts can be approximated to simplify calculations. Important of these approximations is the Fresnel approximation, which assumes that the wavelets take on a nearly parabolic shape. This approximation is particularly valid in the Fresnel diffraction regime, which applies when the Fresnel numbers smaller than 100. For an apparatus with a radius r located at a distance of d with respect to the output plane, the Fresnel number can be calculated as [82]:

$$N_f = \frac{r^2}{\lambda d} \quad (3.1)$$

where λ is the wavelength.

Based on Frensel approximation, if we define X and Y as the coordinates at output

plane, the light field in the output plane (U) can be calculated as follows [82]:

$$U(X, Y) = -\frac{i e^{ikd}}{\lambda d} \int_{-\infty}^{\infty} \int_{-\infty}^{\infty} u(x, y) \exp\left[\frac{ik}{2d}((X - x)^2 + (Y - y)^2)\right] dx dy. \quad (3.2)$$

where x and y are coordinates in the input plane, d is the distance between output and input plane, and k is the wave number. Expanding the terms within the integral makes it evident that the light field can be expressed as a Fourier transform multiplied by a quadratic factor as given in Eq 3.3 [82].

$$U(X, Y) = -\frac{i e^{ikd}}{\lambda d} \exp\left[-\frac{ik}{2d}(X^2 + Y^2)\right] \times \int_{-\infty}^{\infty} \int_{-\infty}^{\infty} u(\xi, \eta) \exp\left[-\frac{ik}{2d}(\xi^2 + \eta^2)\right] \exp\left[\frac{ik}{d}(X \xi + Y \eta)\right] d\xi d\eta. \quad (3.3)$$

where $\xi = \frac{x}{\lambda d}$ and $\eta = \frac{y}{\lambda d}$.

In the Fraunhofer regime, the light field on the output plane can be calculated as [82]:

$$U(X, Y) = -\frac{i e^{ikd}}{\lambda d} e^{-\frac{ik}{2d}(x^2+y^2)} \int_{-\infty}^{\infty} \int_{-\infty}^{\infty} \left[u(\xi, \eta) e^{-\frac{ik}{2d}(\xi^2+\eta^2)} \right] e^{\frac{ik}{d}(x\xi+y\eta)} d\xi d\eta. \quad (3.4)$$

Equation 3.4 is the Fourier Transform of the light field at coordinate system define by ξ and η .

3.2 Methodology

Since we are interested in investigating the response of our designed SpliCon for larger incident angles, we calculated the angle-independent response of the SpliCon for a range of angles beyond the acceptance angle of the experimental setup. To do so, the SpliCon is illuminated by a normally incident plane wave covering wavelengths of 400 nm-1100 nm. The sun's radiation is modeled using Planck's law for black-body radiation at temperature T , given in Eq. 3.5 [83].

$$f(\nu, T) = \frac{8\pi\nu^2}{c^3} \frac{h\nu}{\exp(h\nu/kT) - 1} \quad (3.5)$$

where B is the spectral radiance of a body, ν is the frequency of the electromagnetic radiation, T is the absolute temperature, k_B is the Boltzmann constant ($k_B = 5.6693 \times 10^{-8} \text{ W/m}^2/\text{K}^4$), h is the Planck constant ($h = 6.62607015 \times 10^{-34} \text{ m}^2\text{kg/s}$) and c is the speed of light in the vacuum. The spectral radiance from a black-body as a function of wavelength for a temperature of 5578 K is shown in Figure 3.1.

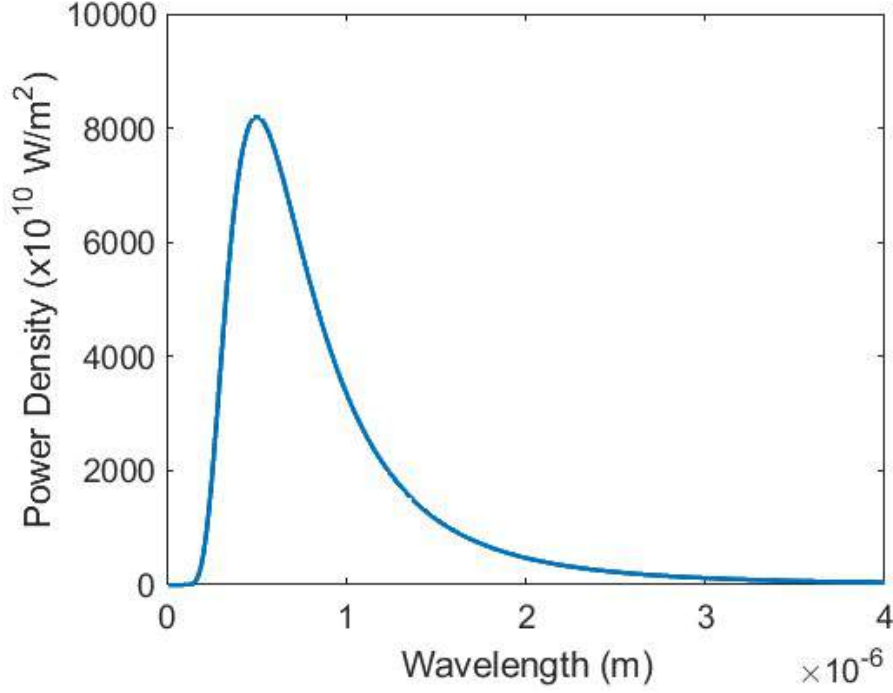


Figure 3.1: The spectral radiance from a black-body as a function of wavelength

The optimized SLM pattern (1920×1080 Pixels), which is shown in Figure 2.12, has been converted into the thickness variations of the DOE. This part will be discussed in detail in the next chapter. In this case, for each pixel on the phase plate, we calculate the corresponding DOE thickness as [47]:

$$h_{xy} = \frac{\lambda}{2\pi [n(\lambda) - 1]} \phi_{xy}(\lambda) \quad (3.6)$$

where, h_{xy} is the thickness of the medium, λ is the wavelength of the incident light, $n(\lambda)$ is the refractive index of the medium and $\phi(\lambda)$ is the phase of the incident light.

The equivalent thickness of the SpliCon for each pixel has an integer multiple of $1 \mu\text{m}$ thickness ranging between $1 \mu\text{m}$ and $8 \mu\text{m}$. The reason to select $1 \mu\text{m}$ steps is due to the limitations in the available fabrication methods. Based on the available methods

of fabrication, such as direct laser writing and 3D printing methods we have decided a resolution of 1 μ m for our device. It is worth to be mentioned that due to the flexibility on the design of our device, this value can be selected with ease of freedom as far as we are not violating fundamental optical principles.

In order to reduce the calculation time, horizontal superpixels are defined, therefore the size of the problem has been reduced from 1920x1080 to 1x1080. In this way a significant reduction in the calculation time is achieved. BK-7 glass is considered as the SpliCon material where its Refractive index as a function of wavelength is defined by Eq. 3.7 given as [84]:

$$n(\lambda) = \sqrt{1 + \frac{1.03961\lambda^2}{\lambda^2 - 0.00600} + \frac{0.23179\lambda^2}{\lambda^2 - 0.02002} + \frac{1.01047\lambda^2}{\lambda^2 - 103.56065}} \quad (3.7)$$

Figure 3.2 illustrates the variation of the refractive index of BK-7 glass as a function of wavelength.

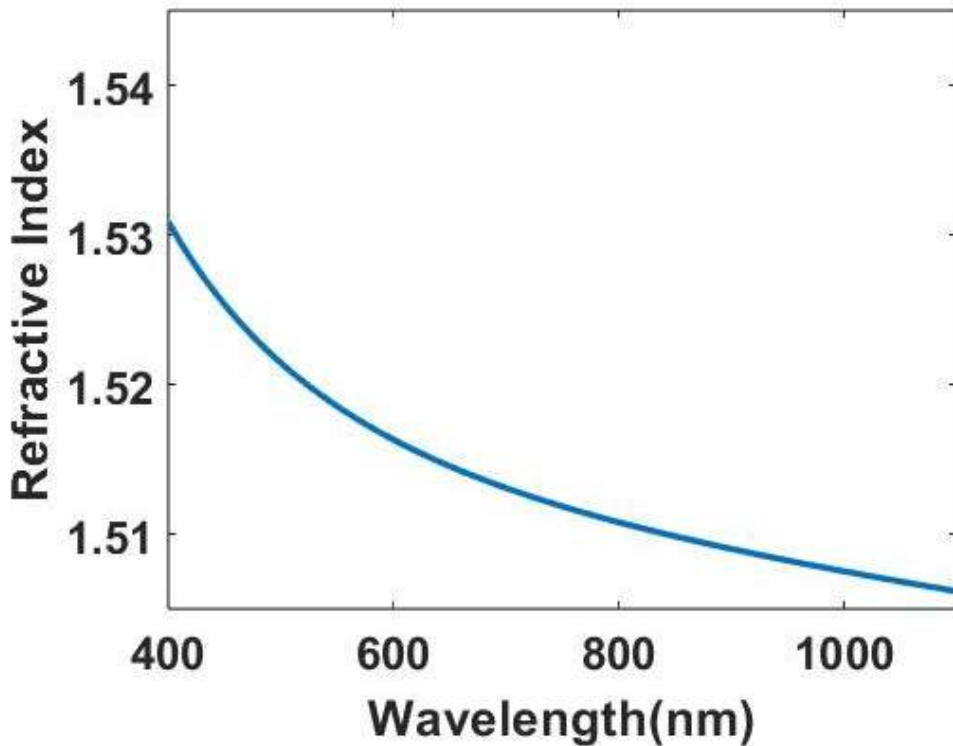


Figure 3.2: Refractive Index of BK-7 glass as a function of wavelength

The calculations of the angle response of the SpliCon have been performed for angles

in a range of $\pm 40^\circ$ using the convolution method by positioning the SpliCon parallel to the output plane as depicted in Figure .

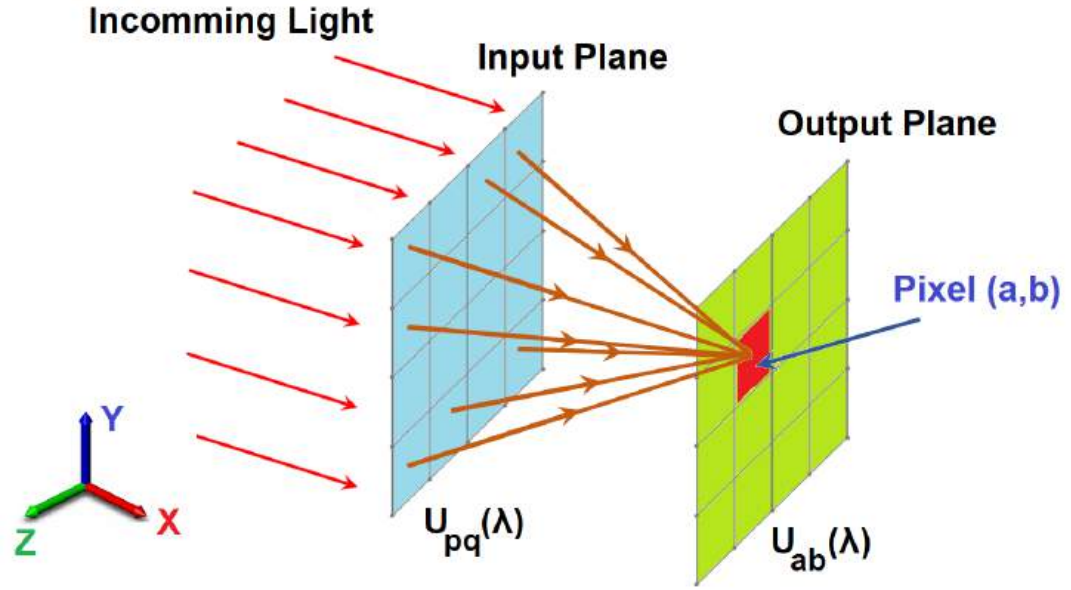


Figure 3.3: Alignment of input and output planes which are divided into pixels to obtain angular response of the optimized SpliCon

We have not considered the polarization of light sources, as it has only a minor effect on the spectral splitting performance of DOEs. Studies indicate that the polarization of light sources does not affect the spectral splitting performance of DOEs by more than 0.1% [3, 85]. Therefore, we assume a normally incident plane wave illumination of the SpliCon that covers the entire wavelength range of the light sources (400-1100 nm) with a 1 nm wavelength resolution. Our calculations also did not take into account material absorption, internal reflections and scattering of the incident light within the SpliCon [3]. We have included the dispersion curve of BK7 [84], to reflect the properties of SpliCon materials. Additionally, we utilize Planck's law to obtain the Blackbody radiation curve of the Sun at different wavelengths. The curve has been normalized by considering the peak spectral radiance of the Sun.

The discrete summation form of Fresnel-Kirchhoff diffraction integral Eq. (3.8) is used to calculate the output electric field distribution (U_{ab}) for desired wavelength λ at a pixel with indices a and b (3.3). In Eq. (3.8) U_{pq} is the electric field distribution of

the incident plane wave after SpliCon on the input plane at a pixel with indices p and q , which is calculated using Eq. (3.9), where A_{pq} and h_{pq} are the amplitude and height of the pixel at a pixel with indices of p and q . The kernel transformation function (G_{pq}) in Eq. (3.8) is calculated using Eq. (3.10), where the (x,y) is used to show the location of the pixels in the input plane, while (X, Y) is used for pixel positions in the output plane. In our calculations, the separation between the input and output planes (d) is taken as $350 \mu\text{m}$ to have diffraction patterns in the Fraunhofer regime.

$$U_{ab}(\lambda) = \sum_{pq} U_{pq}(\lambda) * G_{pq}(\lambda) \quad (3.8)$$

$$U_{pq}(\lambda) = A_{pq}(\lambda) \exp [2\pi j h_{pq} [n(\lambda) - 1] / \lambda] \quad (3.9)$$

$$G_{pq}(\lambda) = \left(\frac{1}{j\lambda d} \right) * \exp \left(\frac{j2\pi d}{\lambda} \right) * \exp \left[j\pi \frac{\{(y_{pq} - Y_{ab})^2 + (x_{pq} - X_{ab})^2\}}{\lambda d} \right] \quad (3.10)$$

Through Eq. (2.3) and Eqs. (3.8 -3.10), the enhancement is calculated for the angle in the range of $\pm 40^\circ$ with an increment of 0.1° .

3.3 Results

Initially, to validate our MATLAB code, we conducted a primary study using the phase plate testified by Yolalmaz and Yüce [3], which is designed to concentrate a monochromatic light at 400 nm onto a single pixel located at the center of the output plane (see Figure 3.4(a)). For this phase plate, we computed the angular response of the equivalent DOE under angled illumination, and the resulting SOE is presented in Figure 3.4(a)). Our SOE exhibits a pattern that closely reflects that reported by the original authors. However, the absolute efficiency values are somewhat lower. This discrepancy is attributed to the fact that we did not have access to the original phase plate; instead, we extracted the phase profile from a PDF source, which altered the gray-level distribution. Nevertheless, the overall agreement between our results and those in the literature is satisfactory.

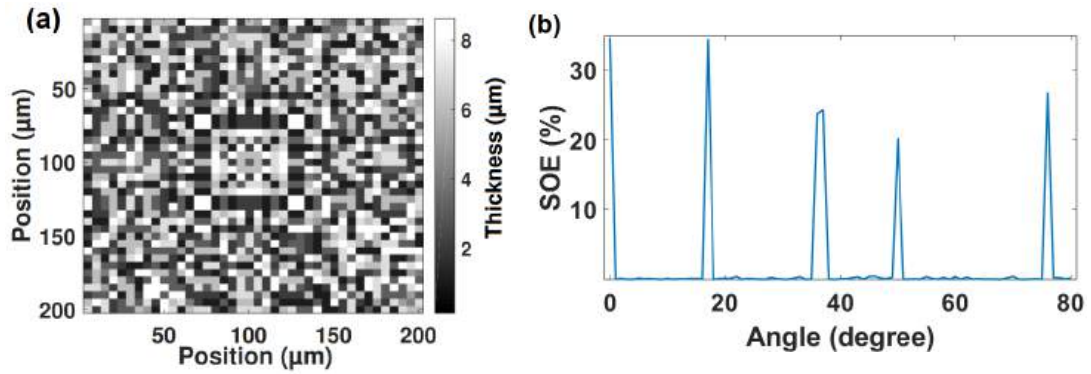


Figure 3.4: (a) The phase plate reported by Yolalmaz and Yüce [3] used for validation, (b) SOE of the test DOE at 400 nm, which is measured at the central pixel of the target plane at different angles of illumination.

After verification of our code, we loaded our optimized phase plate given in Figure 2.13. We used the Fourier optics, leveraging the Huygens–Fresnel principle and the Fresnel diffraction approximation. The optical field at the output plane was computed using a Fresnel propagation method, where the SpliCon modulated the incident wavefront, and the resulting diffracted field was analyzed. Efficiency was determined as the fraction of power focused on a specific region of interest at the output plane relative to the total transmitted power. The resulting efficiency map in Figure shows a wavelength-dependent trend, increasing efficiency at longer wavelengths. Additionally, the DOE exhibits angular robustness across a broad range of incidence angles with relatively stable efficiency, demonstrating its potential for broadband and wide-angle applications.

Angular efficiency response of the diffractive optical element (DOE) at selected wavelengths (400 nm, 550 nm, 700 nm, and 1100 nm) are shown in Figure 3.6. The plot illustrates the stability of the efficiency of the SpliCon across different incidence angles (-40° to 40°). While minor fluctuations are observed, the overall efficiency remains relatively stable, with higher efficiency at longer wavelengths. The peaks and variations in the curves indicate diffraction effects and potential alignment sensitivities in the DOE performance.

The wavelength-dependent efficiency of our SpliCon for different incidence angles (0° , 10° , 20° , and 40°). The results demonstrate a clear trend: efficiency increases

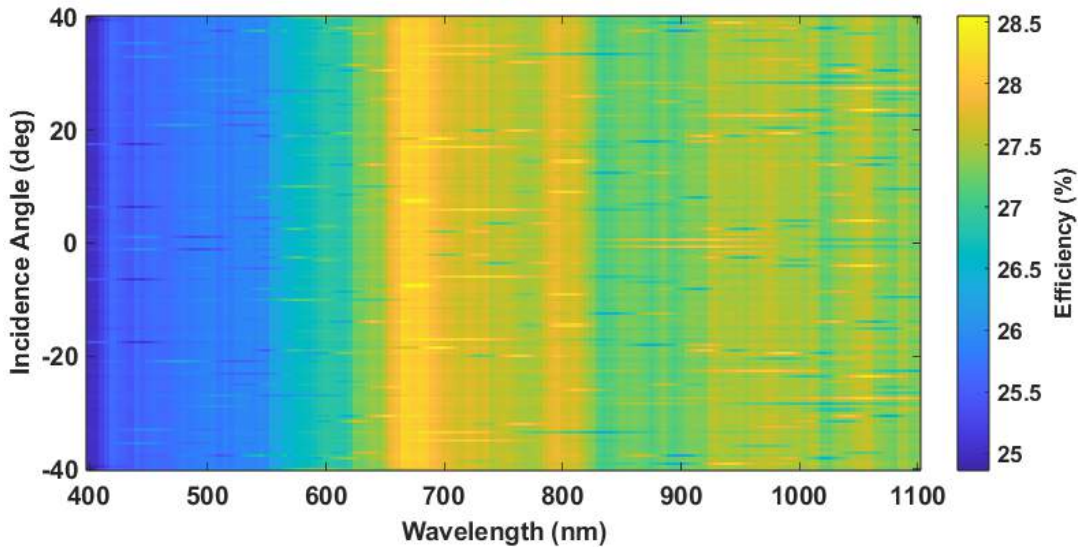


Figure 3.5: Efficiency map of the SpliCon as a function of wavelength (400–1100 nm) and incidence angle (-40° to 40°).

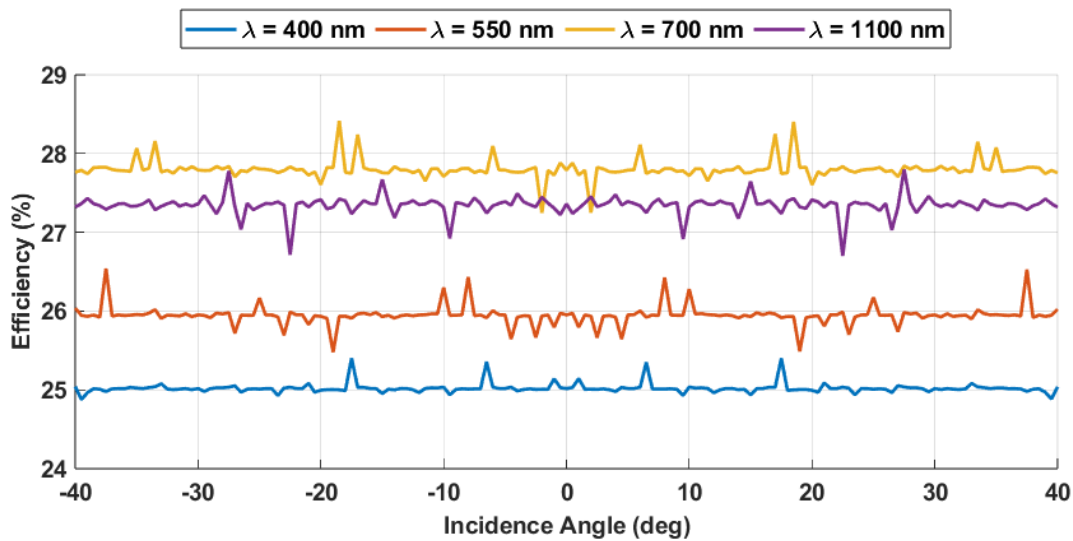


Figure 3.6: Efficiency variation of the SpliCon as a function of incidence angle for selected wavelengths (400 nm, 550 nm, 700 nm, and 1100 nm).

with wavelength up to approximately 700 nm, after which it stabilizes with minor fluctuations. The overlapping curves for different angles indicate that the SpliCon maintains a consistent performance across a range of incidence angles, suggesting angular robustness. Assessing the broadband and angular response of the SpliCon, the Figure shows the potential of our design for applications requiring stability in

optical performance over a wide spectral range. The relative uniformity of efficiency across wavelengths and angles highlights the effectiveness of the SpliCon design in minimizing angular sensitivity and maximizing light utilization.

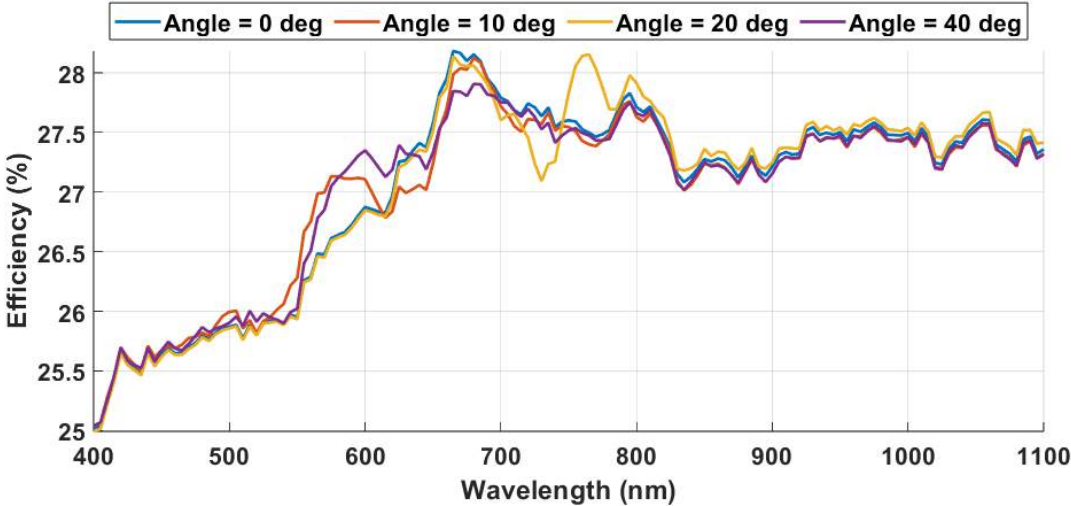


Figure 3.7: Wavelength-dependent efficiency of the SpliCon for different incidence angles (0° , 10° , 20° , and 40°).

In order to compare the results, we also consider the results for the conventional DOE given in

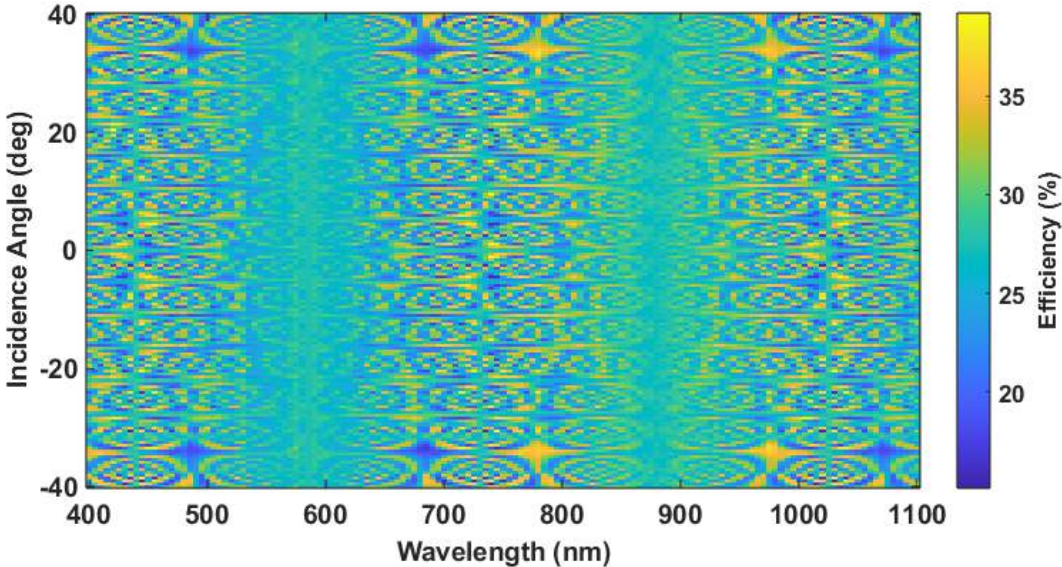


Figure 3.8: Efficiency map of the conventional DOE as a function of wavelength (400–1100 nm) and incidence angle (-40° to 40°).

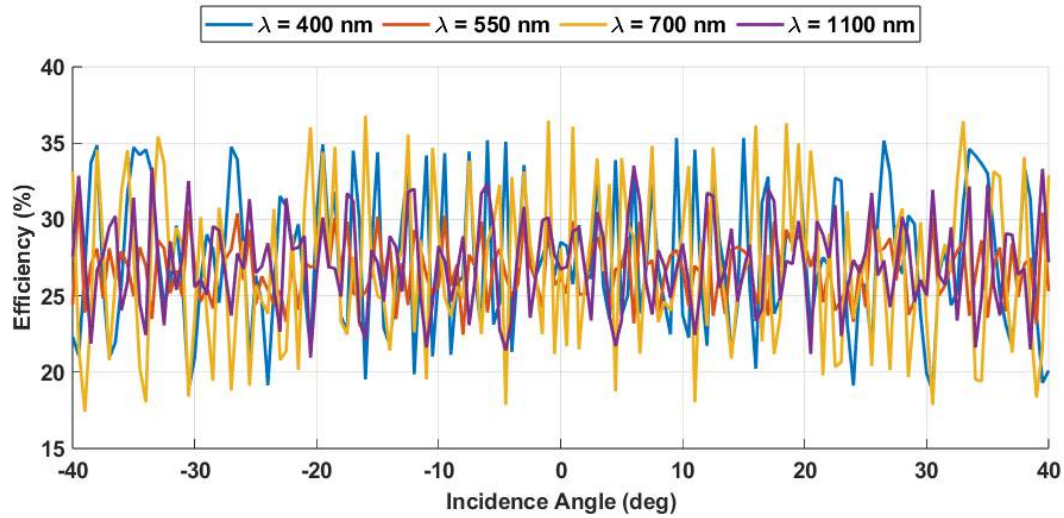


Figure 3.9: Efficiency map of the conventional DOE as a function of wavelength (400–1100 nm) and incidence angle (-40° to 40°).

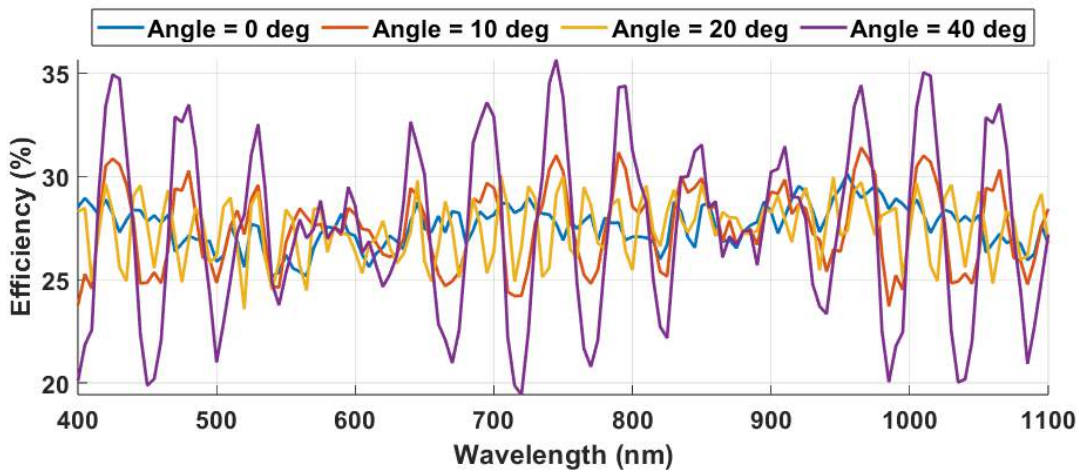


Figure 3.10: Efficiency map of the conventional DOE as a function of wavelength (400–1100 nm) and incidence angle (-40° to 40°).

The calculated enhancement for different angles is shown in Figure 3.11 and is compared with the experimental results.

The SpliCon demonstrated an angle-independent behavior over an expanded range of $\pm 40^\circ$. At a range covering the acceptance angle of the experimental setup the calculated enhancement is in a good agreement with the experimental results, which validated the method. The optimized SpliCon can be fabricated on cost-effective

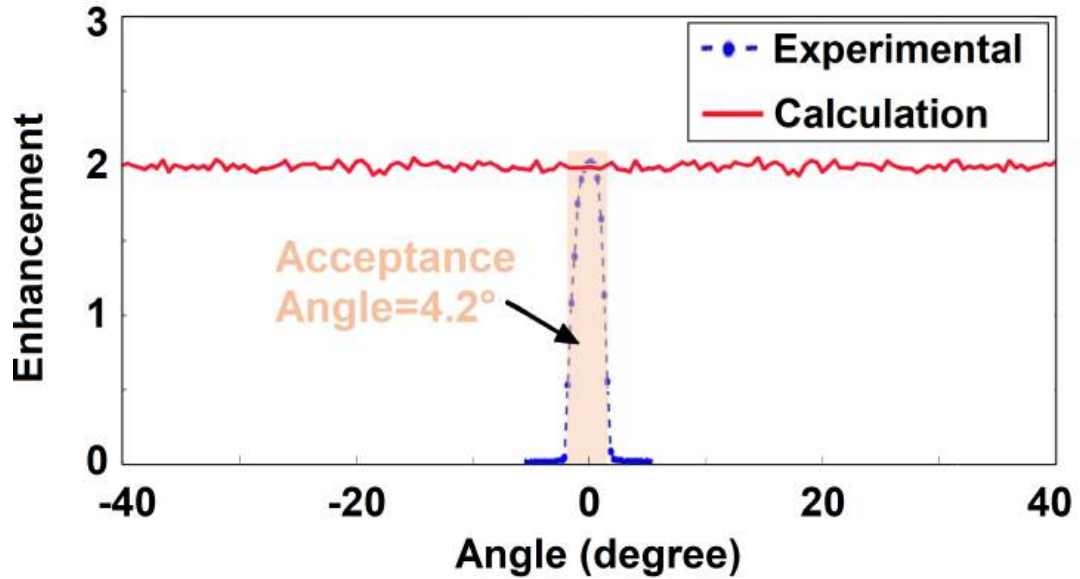


Figure 3.11: Calculations validate the angle independency of the SpliCon outside the acceptance angle of the experimental setup which expands up to $\pm 40^\circ$

materials by different methods including laser writing [85, 86] and can be placed in front of solar cells to improve efficiency. The thermal expansion of the glass on which the SpliCon will be fabricated affects the performance of the splitting and concentration ratio. For this reason, glasses with a low thermal expansion coefficient should be preferred for fabricating SpliCons.

3.4 Conclusions

In this chapter, we explored the angular response of our optimized SpliCon by employing Fourier optics principles and computational modeling. We aimed to extend the analysis beyond the experimental acceptance angle of 4.2° , evaluating SpliCon's efficiency for a broader range of incident angles up to $\pm 40^\circ$. By utilizing Huygens-Fresnel principles, Fresnel diffraction approximations, and convolution-based methods, we successfully modeled and calculated the spectral splitting and concentration behavior of the SpliCon under varied illumination angles.

To ensure the accuracy and reliability of our computational approach, we first validated our MATLAB-based model using a reference phase plate from previous studies,

confirming that our simulations closely matched established experimental data. This verification step was essential in verifying the robustness of our methodology before applying it to the optimized SpliCon. We then converted the 1920×1080 phase pattern of the SLM into an equivalent DOE thickness map, considering the refractive index variations of BK-7 glass as a function of wavelength. The thickness conversion allowed us to model a real-world SpliCon design that could be fabricated using direct laser writing or 3D printing techniques while maintaining the desired resolution to align with fabrication constraints. Our modeling results revealed strong angular stability of the SpliCon across the tested wavelength range (400–1100 nm). The efficiency analysis demonstrated that the SpliCon maintains high spectral splitting and concentration performance over a broad angular range, with a noticeable increase in efficiency at longer wavelengths. The efficiency map showed that while minor diffraction-induced variations were present, the overall angular response remained stable, confirming the suitability of the design for real-world applications.

Further analysis of the wavelength-dependent efficiency for different angles (0° , 10° , 20° , and 40°) demonstrated that efficiency increased with wavelength up to approximately 700 nm, after which it stabilized. This trend suggests that the SpliCon is particularly effective in optimizing longer-wavelength light absorption in solar energy applications. Comparisons with a conventional DOE highlighted the superior angular response of our SpliCon, with significantly reduced efficiency drop-offs at oblique angles. The full-width at half-maximum (FWHM) analysis confirmed that the SpliCon exhibits a wider angular acceptance range compared to conventional DOEs, reinforcing its practical advantages in photovoltaic applications.

Our computational findings align well with experimental results, validating the angle-independent behavior of the SpliCon across an extended angular range of $\pm 40^\circ$, beyond the limits of our experimental setup. This successful validation confirms that the SpliCon can be effectively fabricated and deployed to improve solar cell efficiency by maintaining consistent performance across varying solar incidence angles. Furthermore, we emphasized that choosing appropriate materials with low thermal expansion coefficients is crucial to maintaining long-term stability in real-world environments.

The ability to design a high-efficiency, angle-independent spectral splitting system

opens new possibilities for solar energy harvesting, as SpliCons can be integrated into solar panels to enhance spectral utilization without the need for tracking systems. Future work should explore the practical fabrication of the optimized design and assess its long-term durability and performance under real-world solar illumination conditions. Additionally, further refinements in the computational approach, such as polarization-dependent modeling and material absorption effects, could enhance the accuracy of the simulations.

In conclusion, this chapter successfully demonstrated that the optimized SpliCon not only achieves efficient spectral splitting and concentration but also exhibits robust angular performance across a broad range of incident angles. The combination of experimental and computational validation confirms its potential as a scalable, cost-effective solution for improving photovoltaic efficiency, paving the way for further practical implementations in next-generation solar energy systems.

CHAPTER 4

FABRICATION AND EXPERIMENTAL TESTING OF SPLIIONS

4.1 Transforming an Optimized SpliCon to a Physical SpliCon

As mentioned in the previous chapter, in this thesis, SLM is used to emulate DOEs, providing an ultra-fast way of implementing numerous configurations and finding the optimum design, as it is completely impossible to fabricate physical devices and incorporate them into the test one by one. However, SLM is costly, making it improbable for large-scale photovoltaic applications. The main purpose of using SLM here was to provide a fast and effortless preparation of a SpliCon for desired configurations. After the optimization process and the optimized phase plate have been completed, the SLM needs to be replaced by a physical SpliCon. To do so, the phase information of the phase plate in each pixel should be converted to the equivalent thickness in the physical SpliCon.

The phase modulation of the incident light is defined as [47]:

$$\phi_{xy}(\lambda) = \frac{2\pi}{\lambda} h_{xy} [n(\lambda) - 1] \quad (4.1)$$

where h_{xy} is the thickness of the medium, λ is the wavelength and $n(\lambda)$ is the refractive index of the medium.

Although measuring the refractive index is generally less accurate than measuring the thickness of a material, some techniques, such as ellipsometry, can provide precise measurements of both parameters. For instance, the accurate measurement of thickness and refractive index of Multilayer Antireflective Coatings using ellipsometry has been reported by Yang and Kherani [60]. Additionally, using the refractive index instead of the thickness can offer advantages such as better modeling of thin-film layers

and more accurate predictions of light trapping and absorption.

In a conventional diffractive optical element (DOE) where the periodic phase delay is controlled by altering the thickness of the diffractive material (Figure 4.1(a)). In this case Equation 1 is optimized to obtain the optimal phase. Instead of modulating the thickness, we modulate the refractive index of the material to apply a periodic phase delay because pixels of the SLM have a fixed height value (Figure 4.1(b)). In this case we are controlling $n(\lambda)$ in Eq. 4.1 and obtain the optimal phase. The two different approaches eventually translate into the same effect namely phase shift. Using the SLM the modulation of the refractive index is achieved by gray values applied to each superpixel on the SLM surface. A phase pattern obtained on the SLM surface can be transformed into a physical SpliCon for practical large-scale applications only by using Eq. 4.1.

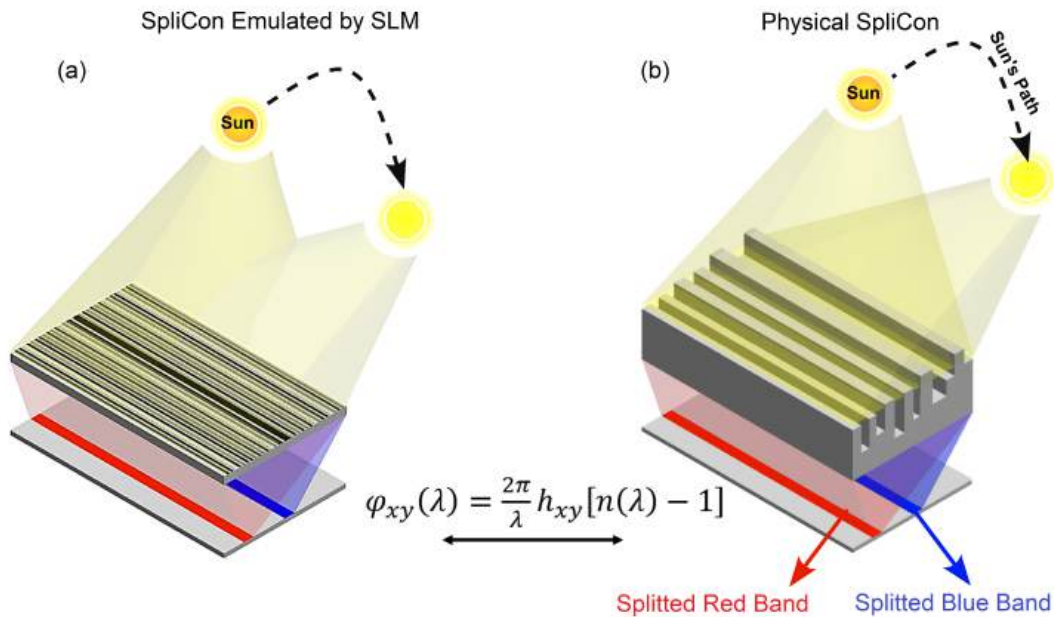


Figure 4.1: (a) The surface of the SLM with seven varying refractive indices , and (b) A physical DOE with seven varying height levels.

When using SLM, instead of modulating the thickness, we modulate the refractive index of the material to apply a periodic phase delay, as the pixels of the SLM have a fixed height value (Figure 4.1(a)). In this case, $n(\lambda)$ in Eq. (4.1) is controlled to obtain the optimal phase. For a physical SpliCon, the periodic phase delay is controlled by altering the thickness of the diffractive material (Figure 4.1(b)). The two different

approaches eventually translate into the same effect namely phase shift. Using the SLM the modulation of the refractive index is achieved by gray values applied to each superpixel on the SLM surface. A phase pattern obtained on the SLM surface can be transformed into a physical SpliCon for practical large-scale applications only by using Eq. (4.1). Since we used an ultra clear resin (photopolymer) to fabricate proof-of-concept SpliCon, we use the refractive index of the polymer ($n_{Polymer}$) in our calculation. To find the thickness profile of the physical SpliCon having the gray levels of the SLM, the phase changes in the SpliCon should be the same as the SLM's. Therefore, we can write:

$$\phi_{SLM} = \phi_{Polymer} \rightarrow \frac{2\pi}{\lambda} h_{SLM} [n_{SLM}(\lambda) - 1] = \frac{2\pi}{\lambda} h_{Polymer} [n_{Polymer}(\lambda) - 1] \quad (4.2)$$

Using Eq.(4.2) the thickness of the SpliCon is calculated as:

$$h_{Polymer} = \frac{[n_{SLM} - 1]h_{SLM}}{n_{Polymer} - 1} \quad (4.3)$$

The thickness of the SLM (h_{SLM}) is selected as 10 μm based on the information received from the manufacturer (HOLOEYE Photonics AG). Using Eq. 4.3, which relates the refractive index of SLM and the polymer height, we calculated the refractive index of SLM versus Gray levels as given in Figure 4.3(a).

The height profile and distribution are given in Figures 4.3(a) and (b), respectively. As it can be seen in Figure 4.3(b) the heights start from a base thickness of 10 μm , which is the base height of the SLM. The maximum thickness reaches 15 μm , indicating that the variation in height between peaks and valleys ranges from 1 to 5 μm . The base thickness can be changed to align with the requirements of fabrication process.

4.2 Fabrication of SpliCons

Diffraction optical elements can be fabricated either by using clean room fabrication methods such as high energy beam direct writing [85, 87], focused ion beam machining [88] and gray scale lithography [54] or by precision tool-based micro-machining techniques such as diamond turning [89] or magnetorheological finish-

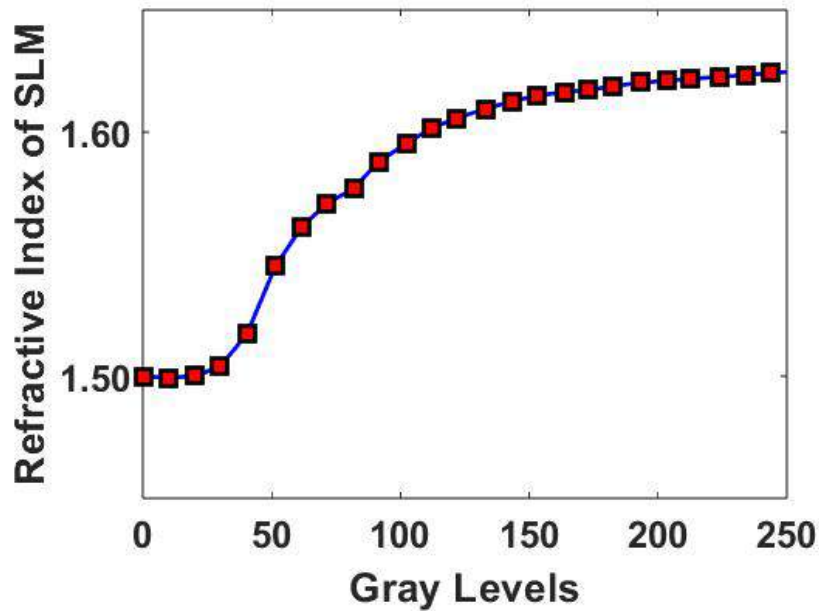


Figure 4.2: Refractive index vs. gray levels of the SLM

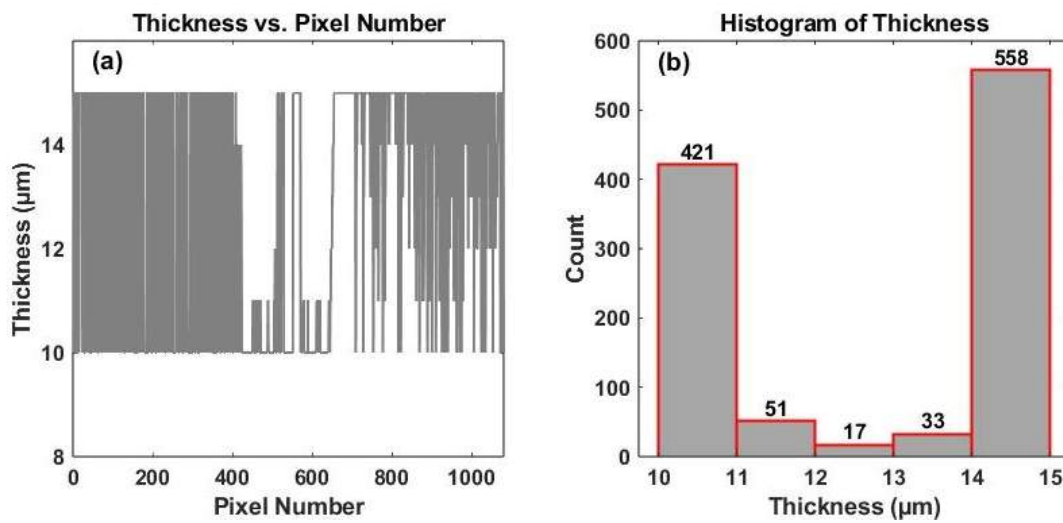


Figure 4.3: (a) Thickness of the physical SpliCon versus Pixel number, and (b) The histogram of thickness distribution of the physical SpliCon

ing [90]. While effective, these methods encounter some limitations and can be time-consuming, costly, and require specialized infrastructure [91].

In this thesis, we tried three different methods to realize our SpliCons. In the first method, we aimed to use direct laser writing to create our micro-features on a crown

glass. The second approach was to create a mirror image of our SpliCon on silicon material and use it as a mold to cast Polydimethylsiloxane (PDMS). As we encountered some limitations in making the mold by direct laser writing, we switched the method to fabricate the SpliCon using stereolithography 3D printing (SLA). In the subsequent sections, we will discuss the challenges we faced during the fabrication process and address the limitations of each technique until we successfully fabricated our SpliCons.

4.2.1 Direct Laser Writing of Crown Glass

In the first attempt to fabricate our SpliCons, we aimed to use direct laser writing of Crown glass. Two methods are available in the literature to use femtosecond/nanosecond lasers on transparent materials based on nonlinear multi-photon absorption. The first method is direct femtosecond laser writing followed by chemical wet etching, known as laser-assisted etching [92]. The second method is to obtain the direct ablation of Glass in water, known as water-assisted femtosecond laser drilling [93].

Based on the setup available in the laser processing laboratory (ALPhA Lab.), the first method is chosen to fabricate SpliCons. The in-house developed laser, produces an average power of 5 W at a wavelength of 1550 nm. The repetition rate can be changed in the range of 100 kHz to 1 MHz depending on the requirements. In this method, two main steps are needed. First, the refractive index of the regions that should be removed is altered by the laser, and then a selective wet etching is performed. The laser-modified regions are selectively wet etched by diluted hydrofluoric (HF) acid solution (typically 5–10%) [94]. Some researchers have reported using sodium hydroxide (NaOH) [95] and potassium hydroxide (KOH) [96]. In this study, we use diluted HF acid solution (8%) to etch the laser-modified layer. Pilot experiments are performed to determine the etching rates.

The fabrication procedure of the SpliCons using direct laser writing is illustrated schematically in Figure 4.4. The Galvo scanner scans and modifies the Crown Glass to the desired depth based on the height information already obtained. The modified layer shows a higher etching rate compared to the bulk crown glass when exposed to the HF dilution, making it possible to etch the modified region selectively. It is worth

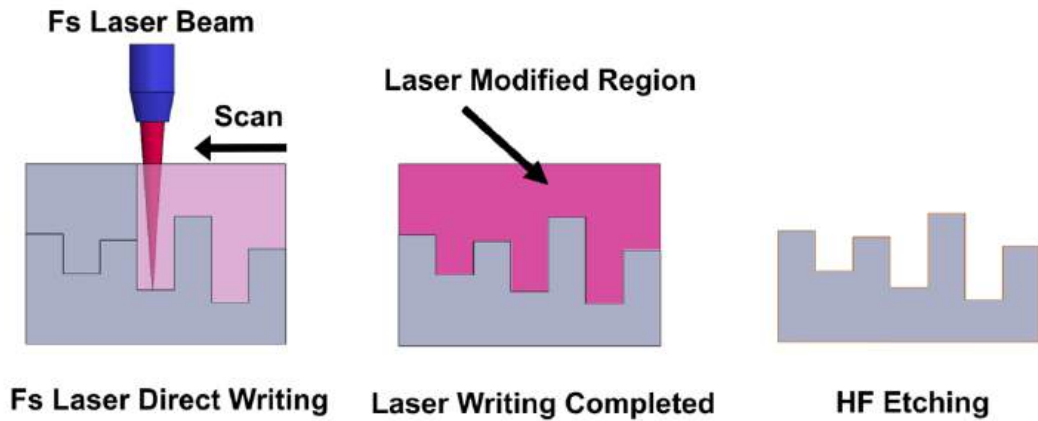


Figure 4.4: Schematic illustration of the direct laser writing method to realize SpliCons on Crown Glass

to be mentioned that, some researchers have reported a heat treatment step before the etching process for photostructurable glass-ceramic (Foturan®) [97]. In our study we did not use any pre-process or post-process heat treatment.

In direct laser writing, the depth of the channels is a function of laser power and scanning steps. To understand the minimum feature size that can be realized using the available laser at ALPhA Lab. on Crown Glass, we used the minimum power of the laser with a single laser scan ($\sim 2.5 \mu\text{J}$). After etching the samples, the depth of the channels is measured, as depicted in Figure 4.5.

Our results revealed that the resolution of the laser is insufficient to fabricate our design, where a height resolution in the order of $1 \mu\text{m}$ is needed. Additionally, our further tests have shown that the process is not repeatable. The channel profiles have also deviated from a square shape, indicating that the method does not meet our fabrication requirements.

Based on the findings derived from direct laser writing on Crown Glass, a primary issue encountered in the production of SpliCons pertains to the inadequate attainment of the desired resolution along the thickness of the device ($1 \mu\text{m}$). To overcome this issue, we have recalculated the thickness variations of the SpliCons. To enhance the precision, increments were chosen to be multiples of $10 \mu\text{m}$. However, since our

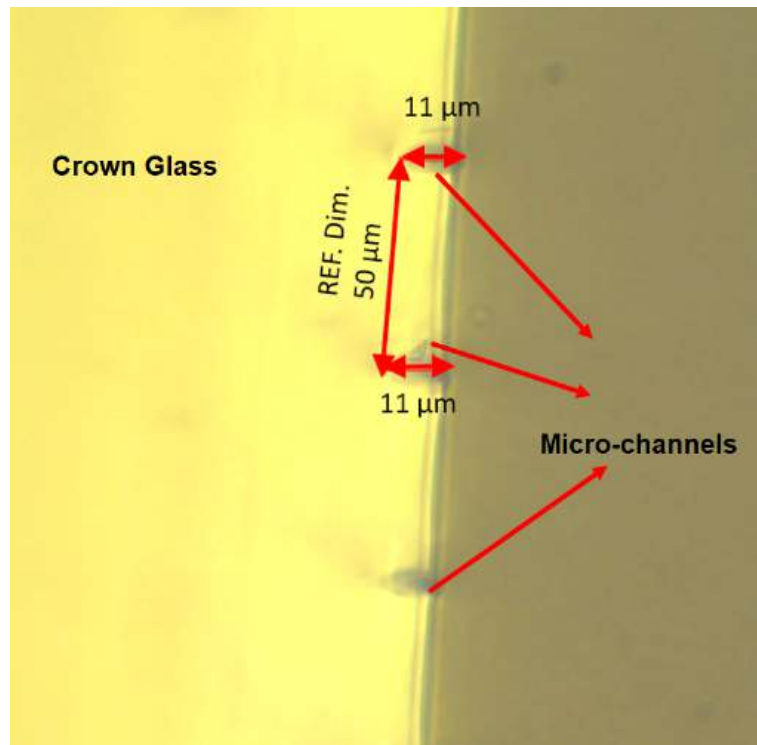


Figure 4.5: Micro-channels produced at the minimum laser energy ($\sim 2.5 \mu\text{J}$) on Crown Glass

lateral resolution was $8 \mu\text{m}$ (single-pixel size), regrettably, this course of action led to an additional complication, namely the aspect ratio of the features, which again made the fabrication process impossible.

Another important factor that motivated us to investigate other fabrication techniques was the limitation of the method of creating male features (protrusions) with various dimensions. As in direct laser writing, we start from the surface and create female features (grooves); the grooves of different depths can be easily created, while the thickness of protrusions remains at the same level and cannot be altered. On the other hand, creating grooves was controllable, while protrusions of different sizes were impossible with the current setup. Thinking of making grooves controllable, we concluded that we should make a mold by direct laser writing and then use this mold to cast some transparent polymers like Polydimethylsiloxane (PDMS), which would give us a replica of the mold with protrusion heights corresponding to the grooves in the mold.

4.2.2 Fabrication of SpliCons by PDMS Casting

Our direct laser writing experiments on Crown Glass revealed that groove depth can be controlled in the process, which led to the idea of using replica-molds to fabricate our SpliCons. A suitable transparent polymer is also needed for our application when using the mold. Our literature survey has shown that researchers in the field of microfluidics widely use Polydimethylsiloxane (PDMS) for applications requiring transparency [98]. The use of PDMS to fabricate multimode waveguides [99], capacitive pressure sensors [100] and transparent flexible antennas [101] has also been reported in the literature. The use of PDMS, with its near-matching refractive index to Glass at 1.41 ($\lambda = 632 \text{ nm}$), further supports the feasibility of this approach [102].

The PDMS casting process starts with the fabrication of a mold on silicon using direct laser writing as illustrated schematically in Figure 4.6(a). After mold has been prepared the PDMS is poured into the mold (Figure 4.6(b)). Two liquid components should be mixed to prepare the PDMS material. One part is the base polymer (Sylgard 184 silicone), and the other acts as a curing agent (cross-linker). The standard mixing ratio of 10:1 is generally used. After molding has been performed, the curing can be done at room temperature or elevated temperatures up to 200 °C [103]. When curing is completed, the SpliCon has been peeled off the mold (Figure 4.6(c)).

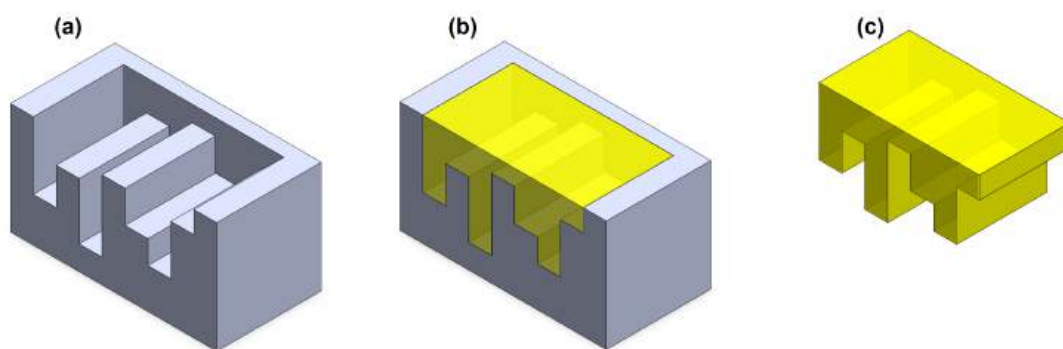


Figure 4.6: Schematic representation of the PDMS casting process: (a) Cross-section of the mold, (b) Pouring PDMS into the Mold Cavity, (c) De-molding of SpliCon after curing

We chose Silicon as a mold material in this study, and several experiments were conducted. We tried single-scan and multi-scan strategies with different etching periods.

The features obtained are shown in Figure 4.7 for various processing parameters. It can be seen that channels of different depths can be fabricated depending on the processing parameters. It is evident from Figure 4.7 that the geometry of the channels (a flat bottom and sharp corners) is far from our desired geometry, meaning that after the casting of PDMS, instead of flat protrusions, hill-like features will be generated.

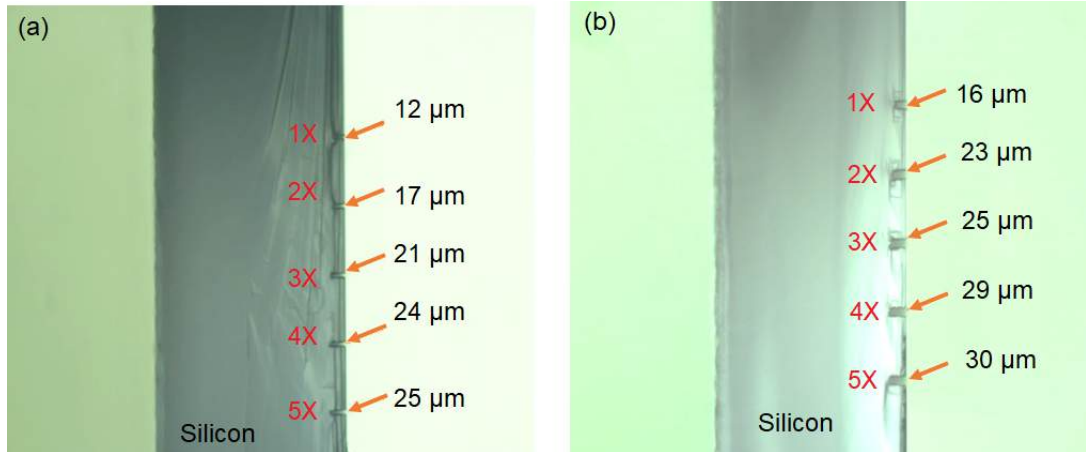


Figure 4.7: Micro-channels fabricated on Silicon using direct laser writing: (a) Different number of scans with an etching period of 5 min., (b) Different number of scans with an etching period of 8 min.

4.2.3 Fabrication of SpliCons by Stereolithography Additive Manufacturing

As we encountered limitations in realizing our SpliCons using direct laser writing, we opted to implement additive manufacturing (AM) techniques to fabricate SpliCons. Our literature survey has revealed that AM, also known as three-dimensional (3D) printing, is a promising method to realize optical and photonic components, including lenses [104], free-form optics [105], beam splitters [106] and diffractive optical elements [107], to name a few. AM techniques encompass different methods that can be applied to metals and polymers. In this study, we fabricated our SpliCons using stereolithography (SLA) 3D printing. SLA, also known as photo-solidification, is a precise AM process that uses a focused light source to selectively cure or solidify a reactive liquid photo-polymer layer-by-layer. The energy required to start polymerization, a process in which several tiny monomers chemically join to generate strongly cross-linked macro-molecules is provided by the irradiation process [108].

4.2.3.1 Materials for the SLA

Compared with other AM technologies, SLA has a more limited selection of materials [109], where the selected material should also be compatible with the 3D printer. Finding appropriate material becomes more challenging for our application, where optical properties and transparency are the main concerns. Searching for a suitable resin to fabricate transparent SpliCons, we found a highly clear resin by ANYCUBIC. Based on the information provided by the manufacturer, thanks to its optimized formula, resin offers a 100% increase in flexibility compared to standard resin, which allows for more durable prints and makes them less prone to breaking and distortion during printing process. The refractive index of the ultra-clear resin is reported to vary between 1.515 and 1.495 for wavelengths in the range of 380-800 nm after printing and curing [110]. The selected resin is formulated to produce parts that remain crystal clear for an extended period in indoor environments, resisting yellowing over time. For our application, the UV wavelength compatibility of 365-405 nm ensures efficient curing, while the high transparency and resistance to yellowing for over 30 minutes make it suitable for optical components. Additionally, the low molding shrinkage (3.72-4.24%) helps maintain dimensional accuracy, and the high flexural modulus (>798 MPa) and tensile strength (28.1 MPa) contribute to structural stability, making it ideal for precise optical elements.

4.2.3.2 Computer-aided Design

Like any other 3D printing process, SLA builds 3D physical prototypes using a 3D CAD model. Our SpliCon design includes over 1000 micro-scale features, making its 3D modeling highly challenging and time-consuming. The manual creation of these micron-sized features, one-by-one, is highly susceptible to human error. Additionally, whenever we change our design, the 3D model must be recreated, which is time-consuming. To facilitate the generation of the 3D model, a macro has been developed and is integrated to the SolidWorks program, which automatically generates our design. To do so, after height calculations are performed by MATLAB, the height information will be stored in an Excel file. The developed macro reads the height information from the Excel file to generate a point cloud. The points are connected to

each other by straight lines resulting in the contour of the cross-section of the device. This contour is then extruded to achieve the 3D solid model as depicted in Figure 4.8. To prevent the distortion of the device due to its very thin and flexible structure, a frame has been created on the perimeter of the SpliCon to provide additional rigidity to the device.

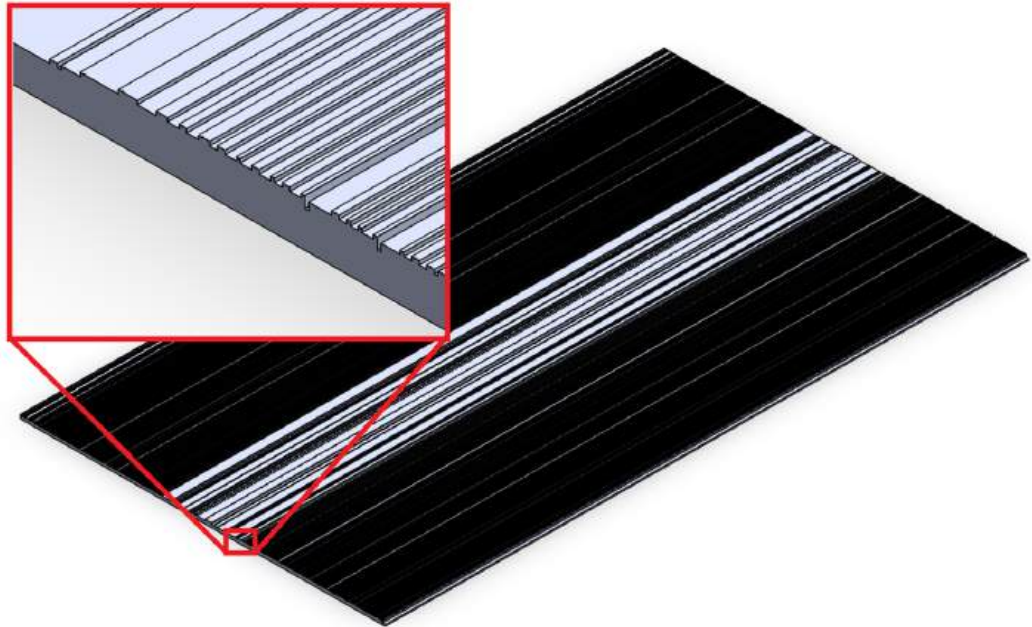


Figure 4.8: Solid Model of the SpliCon

4.2.3.3 SLA 3D Printing

Upon completing the solid model of the SpliCon and selecting the appropriate printing resin, the slicing of the 3D model was performed using the Formware 3D Slicer program. The orientation of the parts for 3D printing has been optimized using this software. The structural supports are set to be applied on the frame side of the model to ensure the part stability during fabrication and keep the SpliCon features intact. The sliced information has been exported to the Form 4 SLA 3D printer in the standard tessellation language (STL) format. All the parameters of the 3D printer have been set at their finest value. Figure 4.9 illustrates the parameters and slicing process for the SpliCon fabrication. A closer view of the SLA process for SpliCon fabrication is given in Figure 4.10.

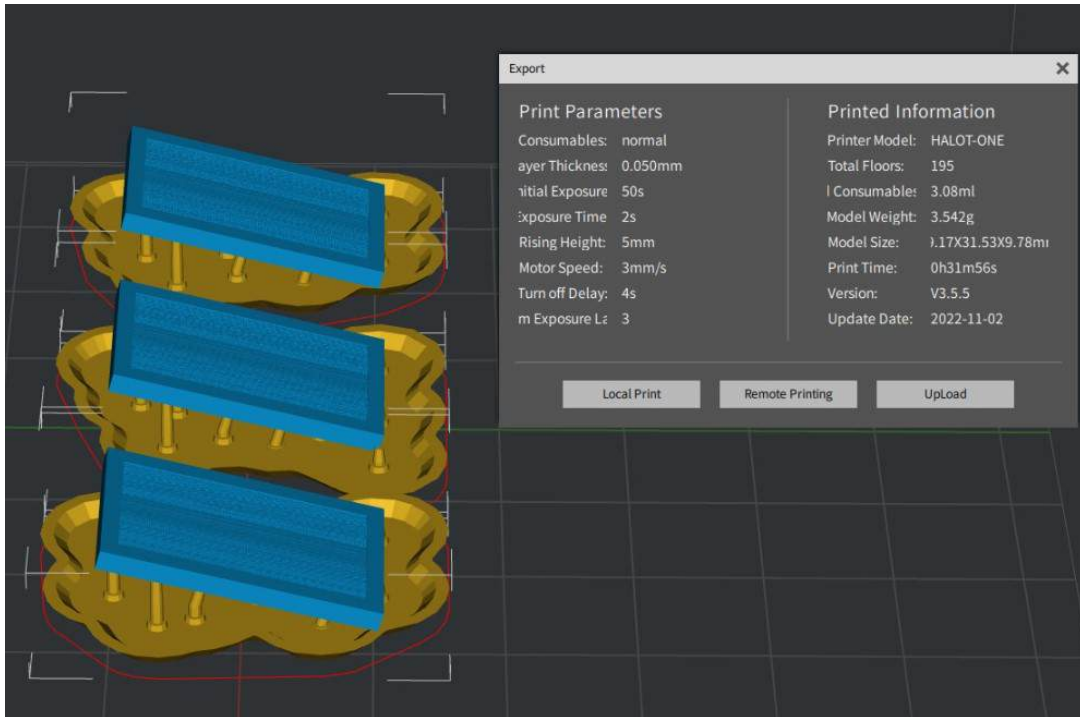


Figure 4.9: SLA settings for the SpliCon fabrication

For high clear resin, a layer thickness of 0.05 mm is recommended, with an exposure time of 4 seconds to ensure proper curing. A light-off time of 2 seconds is suggested to allow sufficient cooling between layers. The bottom exposure time is set to 25 seconds, with 4 bottom layers to enhance adhesion to the build plate. Additionally, an anti-aliasing level of 1 is applied to improve surface smoothness. The Z lift distance is 8 mm, with both the Z lift speed and Z retract speed set to 6 mm/s for optimal movement and layer stability.

The fabricated SpliCons are shown in Figure 4.11(a). After fabrication, the topography of the features on the SpliCons was carefully evaluated with a laser scanning microscope (LSM) to ensure the success of fabrication. This thorough examination sheds light on the micro-scale features, surface properties and dimensional accuracy. Figure 4.11(b) displays the topography of the device that was gathered and illustrates how well the designed features were replicated in the SpliCons that were manufactured. The realization of feature sizes in the order of 1-1.5 μm is evident in the surface topography measurement of the SpliCon. The layered structure of the device, which arises from the nature of the process, is also evident. It is worth mentioning that, with

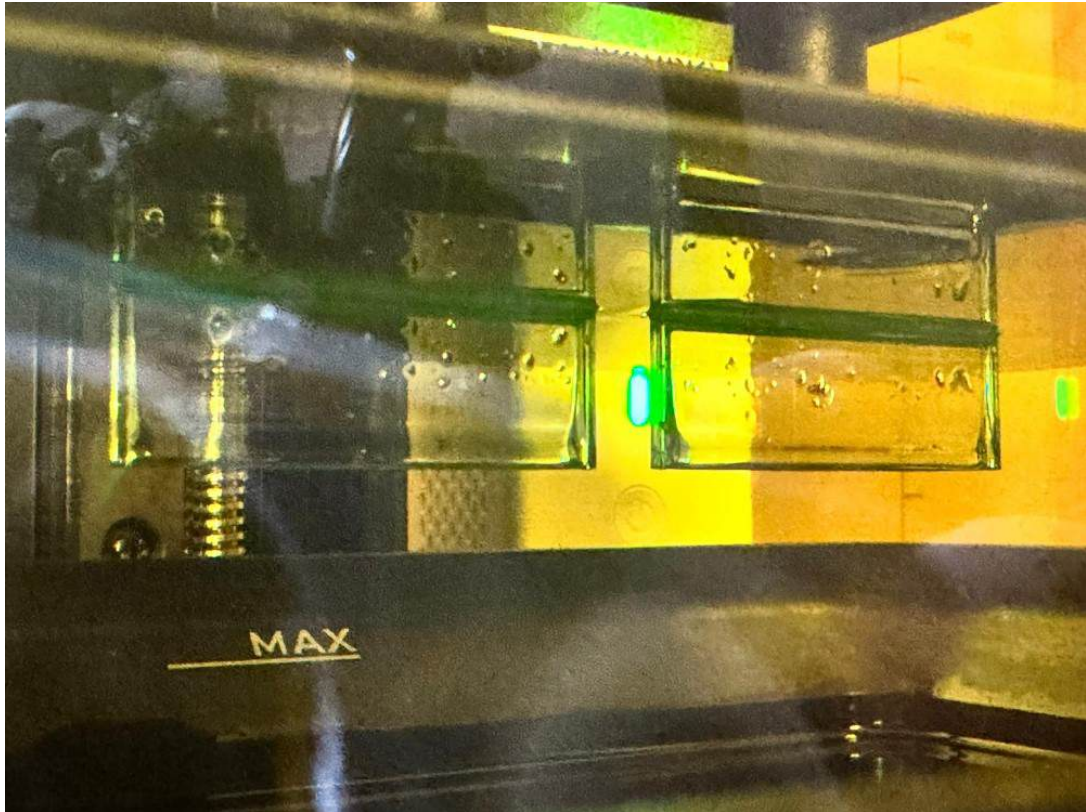


Figure 4.10: SLA 3D printing to realize proof-of-concept SpliCons

some advanced AM techniques such as two-photon polymerization it is possible to achieve surface roughness values of less than 15 nm and feature sizes as small as 140 nm [111].

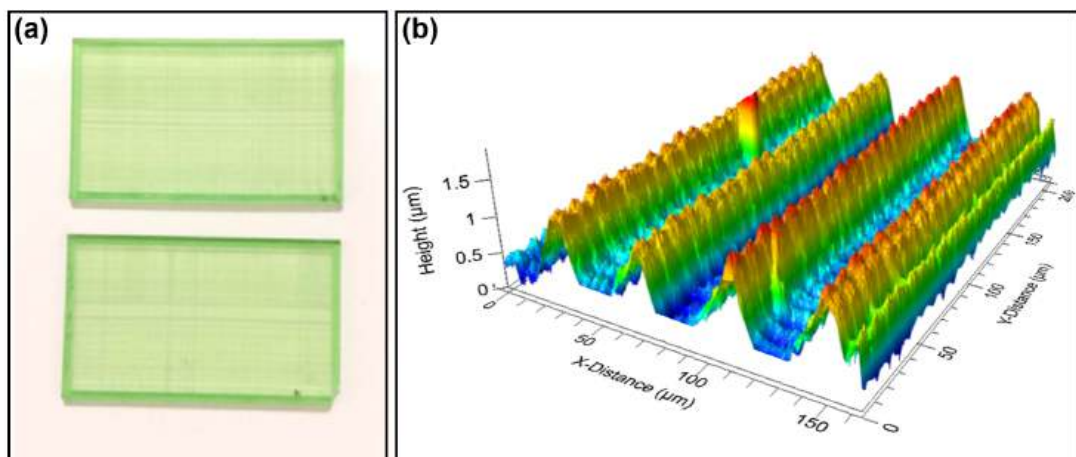


Figure 4.11: (a) Proof-of-concept SpliCons fabricated by SLA 3D printing, and (b) Topography of the SpliCons measured by LSM.

4.3 Experimental Testing of SpliCons

Upon a successful fabrication of the proof-of-concept SpliCons using SLA additive manufacturing technique, the SLM has been removed and replaced with the physical SpliCon and subjected to the illumination tests using broadband light source. The experimental setup to test the proof-of-concept SpliCon is shown in Figure 4.12. Similar to the experimental setup of Figure 2.2, the setup is equipped with a motor-controlled mirror to manipulate and control the angle of the incident light.

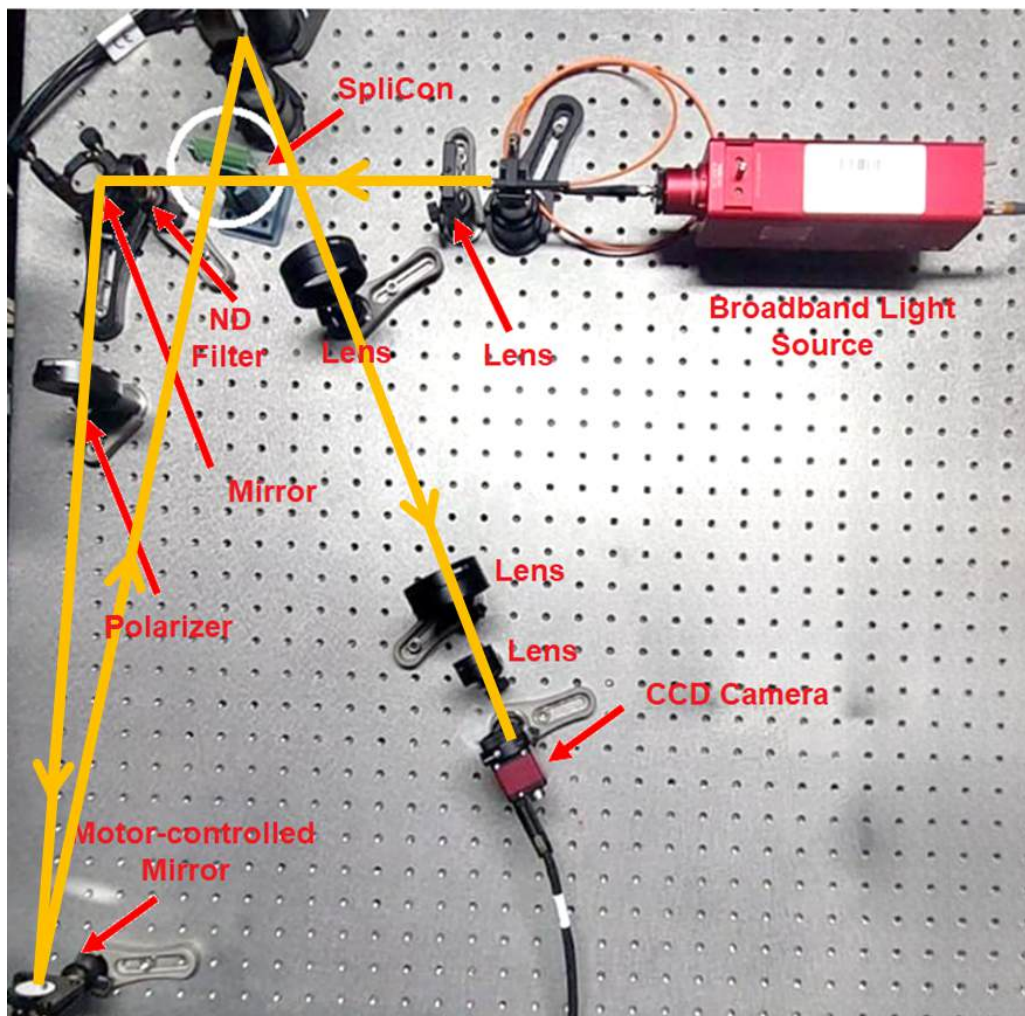


Figure 4.12: Experimental setup to test the proof-of-concept SpliCon

As the device is composed of a layered structure, some scatter in the incident light has been observed. The raw image captured on the CCD camera has been shown in Figure 4.13.



Figure 4.13: The raw image on the CCD camera for the proof-of-concept SpliCon

In order to reduce the effect of layered structure on our results, a plain device has been fabricated using the same procedure, and the images were obtained before using SpliCon. The intensity profiles before (using plane device) and after wavefront shaping by SpliCon captured by the CCD camera are shown in Figure 4.14(a) and (b), respectively. The differential changes in the intensity is given in Figure 4.14(c), which indicates the increase in the intensity in the region of interest using the proof-of-concept SpliCon. The intensity increase for each color band can be clearly distinguished from Figure 4.14(d-f), which indicates the success of the designed SpliCon for the simultaneous spectral splitting and concentration of the broadband incident light.

After successful spectral splitting and concentration have been observed, the proof-of-concept SpliCon has been investigated for its angle independence. The motor-controlled mirror that precisely altered the angle of incidence was used to illuminate the SpliCon at different angles in the range of acceptance angle of the system. The achieved enhancement for different angles, displayed in Figure 4.15, demonstrates the angular response of the device and proves its capacity to function consistently across a range of incident angles.

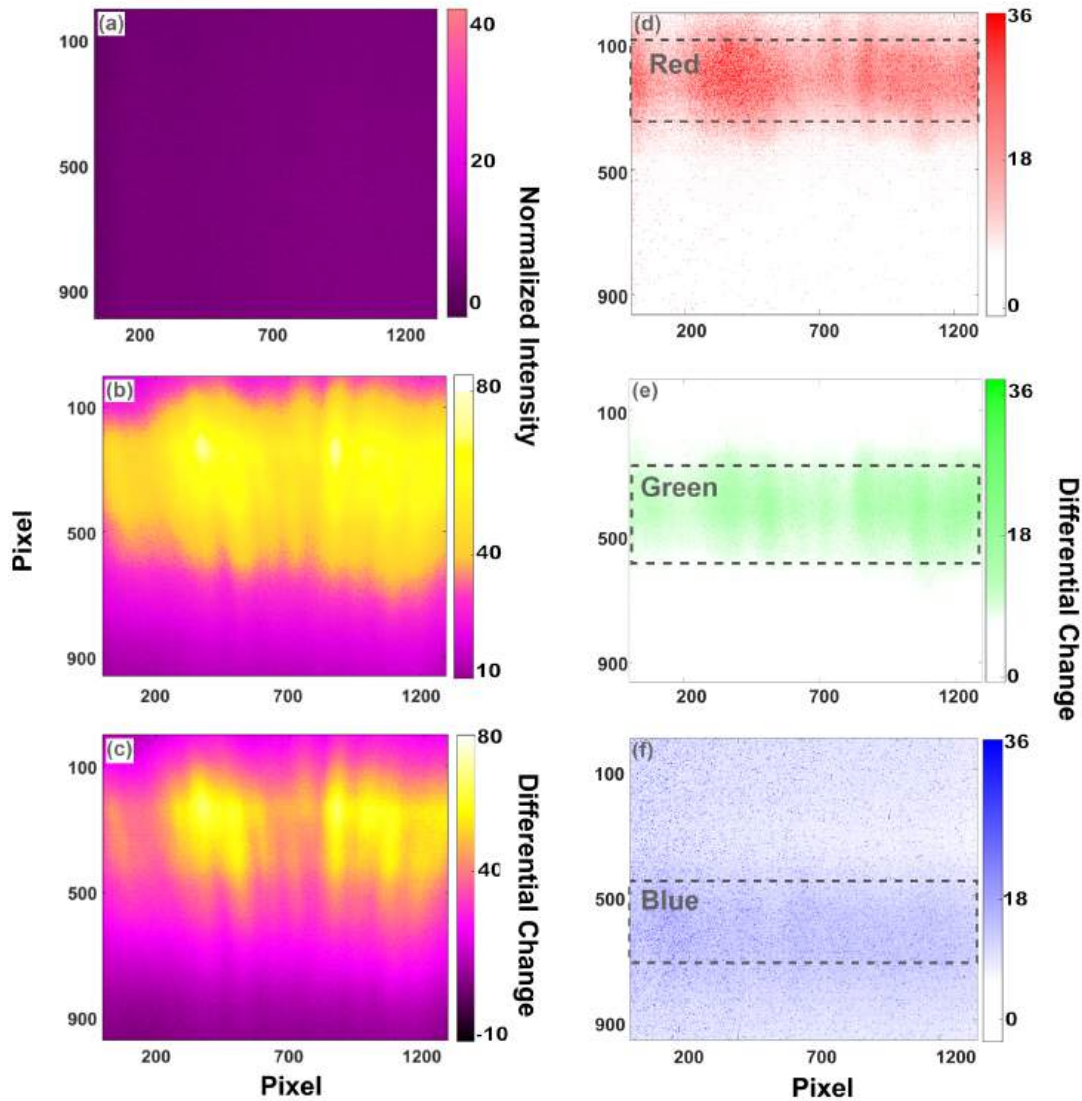


Figure 4.14: The intensity profiles for: (a) plane device, (b) proof-of-concept Split-Con, (c) Differential intensity changes for combined color channels. Differential change for separate colors (d) Red, (e) Green and (f) Blue. The dashed lines indicate the target areas in which the colors are concentrated.

Considering the fact that solar irradiance is not uniform across all wavelengths [112], we have measured the power of different bands of our light source using a power meter in front of our light source. The powers measured are 103 μW , 116 μW , and 139 μW for the red, green, and blue bands, respectively. These variations in the measured power are similar to the power of different bands in the sunlight, meaning that our halogen lamp can mimic the sunlight. However, the spectrum of our illumination

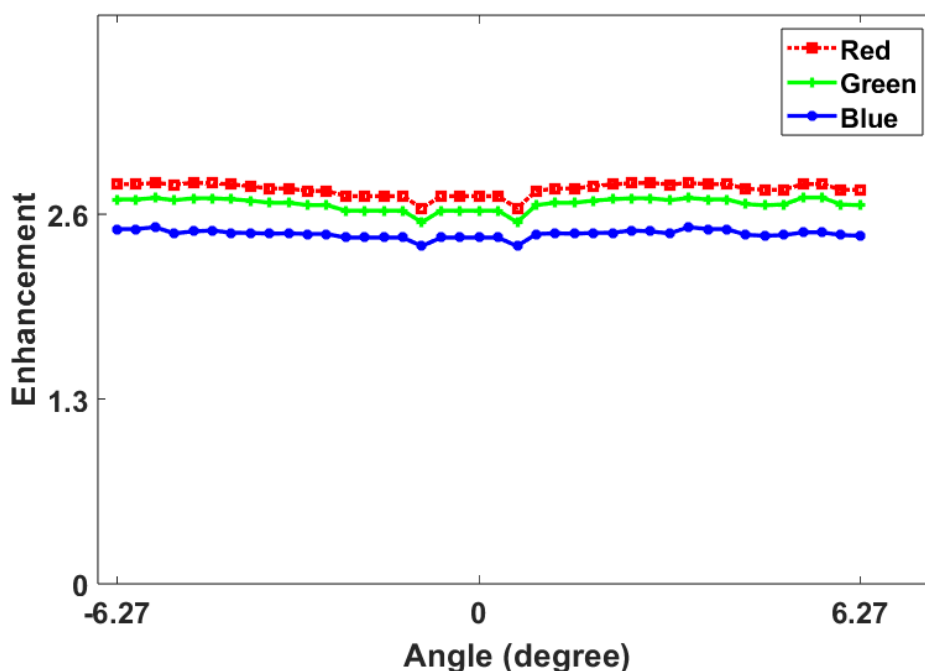


Figure 4.15: The enhancement of the proof-of-concept SpliCon under angled illumination

may not perfectly match the spectrum of the actual sunlight that the solar cell will be exposed to. This can lead to an overestimation of the cell's performance in some frequency bands, which can skew overall performance measurements of the solar cells when integrated with our SpliCons. This is one of the issues reported for the indoor performance measurement of PV modules using solar simulators, known as a spectral mismatch. To overcome this problem, a spectral mismatch correction factor (MMF) can be utilized, as described in detail in the work of Chantana et al. [113, 114].

Another important challenge which may be faced, when applying SpliCons in real solar systems, is the difference in physical and mechanical properties of SpliCons and solar cell materials. Using materials with different coefficients of thermal expansion (CTE) results in thermal stress and mechanical failure. This can cause the SpliCon to detach from the solar cell, reducing its effectiveness or even damaging it. This is becoming more critical when these materials have been bonded together at their common interface. In our design, we have considered a gap of 350 μm between the cells and SpliCon. Consequently, the thermal stresses will not be directly transferred

into the Splicon. Even if the manufacturers prefer a transparent bond during the integration process, the elasticity of the thin bonding layer can accommodate enough thermal stresses to avoid failure and delamination of the SpliCon from the solar cell. This additional layer may be selected to have a CTE between SpliCon and solar cell material acting as a functional gradient material (FGM), providing a smooth transition of stresses between different layers [115]. Additionally, the new developments in the production of transparent glass-ceramic materials [116] make it possible to choose materials with CTEs very close to the solar cell materials, which can help reduce the risk of thermal stress and mechanical failure.

4.4 Conclusions

In this chapter, the thickness variations of the SpliCon have been determined based on SLM-generated phase plate. A subroutine has been developed, which automatically generates the 3D solid model of the SpliCon based on the information stored in an Excel file. After the solid model has been prepared, different fabrication methods have been examined to realize the SpliCons, including direct laser writing of Crown Glass, direct laser writing of Silicon mold to cast SpliCons from PDMS material, and stereolithography 3D printing of SpliCons using an ultra-clear resin. Depending on the limitations of each method, We have faced several challenges during fabrication. Among available techniques, We fabricate a proof-of-concept SpliCon using stereolithography additive manufacturing. The fabricated SpliCon underwent testing under angled illumination, and the results showed successful angle-independent spectral splitting and concentration of broadband light, thereby validating the concept.

CHAPTER 5

CONCLUSION AND OUTLOOK

In this thesis, angle-independent SpliCons, capable of simultaneously splitting and concentrating broadband light, are reported for the first time. We implement an experimental optimization method for wavefront shaping, demonstrating significantly reduced optimization time compared to computational techniques. In this method, a phase-only SLM is used to emulate the SpliCon, where the thickness variations in the SpliCon are emulated by controlling and modifying the gray levels in the SLM.

Using the optimized SpliCon, we obtain 58%, 51%, and 59% spectral splitting ratios with an enhancement factor of 202%, 188%, and 204% for red (560-875 nm), green (425-620 nm), and blue channels (420-535 nm), respectively. A full-width half maximum (FWHM) of 3.2° has been achieved compared to 0.66° for a conventional DOE within the acceptance angle of the experimental setup of 4.2° . For incident angles exceeding our setup's acceptance angle, we performed simulations using the convolution method. The simulation results revealed angle independence in the range of $\pm 40^\circ$. When a tracking system is used, the efficiency of the solar panel increases as we maintain the optimal angle of the incident light on the solar panel. However, these systems can not be mounted on the buildings' roofs or the building's side walls. Additionally, they impose many maintenance costs, increase the investment cost, and consume some of the energy produced by the system's motors. So, this system does not offer a comprehensive solution. Our angle-independent SpliCon design maximizes the energy in which a solar panel can collect from the available energy input, without a need for costly sun tracking systems.

We fabricate a proof-of-concept SpliCon using stereolithography additive manufac-

turing(3D printing) with an ultra-clear resin. The fabricated SpliCon underwent testing under angled illumination, and the results showed successful angle-independent spectral splitting and concentration of broadband light, thereby validating the concept.

5.1 Recommendations for Future Works

- In this thesis, we used a Continuous Sequential algorithm to optimize the phase plate for the SpliCon. New optimization algorithms can be developed for wavefront shaping. The performance of various existing algorithms, such as Stepwise Sequential, Segmented, Hybrid Stepwise Continuous, and Hybrid Segmented Continuous, can also be evaluated in SpliCon design.
- The developed algorithm can be implemented to reduce the reflectance intensity of solar cells by utilizing phase plates created by implementing a spatial light modulator. The approach's efficacy in enhancing solar cells' performance and its potential impact on mitigating global warming can be investigated.
- In this thesis, SpliCons are realized through the additive manufacturing process of stereolithography. The applicability of the other fabrication techniques can also be investigated and compared.

REFERENCES

- [1] S. Essig, C. Allebé, T. Remo, J. F. Geisz, M. A. Steiner, K. Horowitz, L. Barraud, J. S. Ward, M. Schnabel, A. Descoeurdes, *et al.*, “Raising the one-sun conversion efficiency of iii-v/si solar cells to 32.8% for two junctions and 35.9% for three junctions,” *Nature Energy*, vol. 2, no. 9, pp. 1–9, 2017.
- [2] A. Polman and H. A. Atwater, “Photonic design principles for ultrahigh-efficiency photovoltaics,” *Nature materials*, vol. 11, no. 3, pp. 174–177, 2012.
- [3] A. Yolalmaz and E. Yüce, “Angle-independent diffractive optical elements for efficient solar energy conversion,” in *Photonics for Solar Energy Systems VIII*, vol. 11366, pp. 43–50, SPIE, 2020.
- [4] M. N. Erim, N. Erim, and H. Kurt, “Spectral splitting for an ingap/gaas parallel junction solar cell,” *Applied Optics*, vol. 58, no. 16, pp. 4265–4270, 2019.
- [5] M. A. Green, “Photovoltaic technology and visions for the future,” *Progress in Energy*, vol. 1, no. 1, p. 013001, 2019.
- [6] A. G. Martin, E. Keith, H. Yoshihiro, W. Wilhelm, and D. D. Ewan, “Solar cell efficiency tables (version 39),” *Progress in photovoltaics: research and applications*, vol. 20, no. 1, pp. 12–20, 2012.
- [7] T. Leijtens, K. A. Bush, R. Prasanna, and M. D. McGehee, “Opportunities and challenges for tandem solar cells using metal halide perovskite semiconductors,” *Nature Energy*, vol. 3, no. 10, pp. 828–838, 2018.
- [8] J.-H. Yun, E. Lee, H.-H. Park, D.-W. Kim, W. A. Anderson, J. Kim, N. M. Litchinitser, J. Zeng, J. Yi, M. M. D. Kumar, *et al.*, “Incident light adjustable solar cell by periodic nanolens architecture,” *Scientific reports*, vol. 4, no. 1, p. 6879, 2014.
- [9] A. Imenes and D. Mills, “Spectral beam splitting technology for increased con-

- version efficiency in solar concentrating systems: a review,” *Solar energy materials and solar cells*, vol. 84, no. 1-4, pp. 19–69, 2004.
- [10] Q. Huang, J. Wang, B. Quan, Q. Zhang, D. Zhang, D. Li, Q. Meng, L. Pan, Y. Wang, G. Yang, *et al.*, “Design and fabrication of a diffractive optical element as a spectrum-splitting solar concentrator for lateral multijunction solar cells,” *Applied optics*, vol. 52, no. 11, pp. 2312–2319, 2013.
- [11] A. Barnett, D. Kirkpatrick, C. Honsberg, D. Moore, M. Wanlass, K. Emery, R. Schwartz, D. Carlson, S. Bowden, D. Aiken, *et al.*, “Very high efficiency solar cell modules,” *Progress in Photovoltaics: Research and Applications*, vol. 17, no. 1, pp. 75–83, 2009.
- [12] G. Kim, J. A. Dominguez-Caballero, H. Lee, D. J. Friedman, and R. Menon, “Increased photovoltaic power output via diffractive spectrum separation,” *Physical review letters*, vol. 110, no. 12, p. 123901, 2013.
- [13] A. Mojiri, R. Taylor, E. Thomsen, and G. Rosengarten, “Spectral beam splitting for efficient conversion of solar energy—a review,” *Renewable and Sustainable Energy Reviews*, vol. 28, pp. 654–663, 2013.
- [14] G. Li, Z. Su, L. Canil, D. Hughes, M. H. Aldamasy, J. Dagar, S. Trofimov, L. Wang, W. Zuo, J. J. Jerónimo-Rendon, *et al.*, “Highly efficient pin perovskite solar cells that endure temperature variations,” *Science*, vol. 379, no. 6630, pp. 399–403, 2023.
- [15] M. Yang, S. Fu, L. Wang, M. Ren, H. Li, S. Han, X. Lu, F. Lu, J. Tong, and J. Li, “Efficient organic solar cells by modulating photoactive layer morphology with halogen-free additives,” *Optical Materials*, vol. 137, p. 113503, 2023.
- [16] M. Yamaguchi, K.-H. Lee, K. Araki, and N. Kojima, “A review of recent progress in heterogeneous silicon tandem solar cells,” *Journal of Physics D: Applied Physics*, vol. 51, no. 13, p. 133002, 2018.
- [17] R. King, a. Law, K. Edmondson, C. Fetzer, G. Kinsey, H. Yoon, R. Sherif, and N. Karam, “40% efficient metamorphic gainp/ gainas/ ge multijunction solar cells,” *Applied physics letters*, vol. 90, no. 18, 2007.

- [18] H. Cotal, C. Fetzer, J. Boisvert, G. Kinsey, R. King, P. Hebert, H. Yoon, and N. Karam, “III–V multijunction solar cells for concentrating photovoltaics,” *Energy & Environmental Science*, vol. 2, no. 2, pp. 174–192, 2009.
- [19] F. Dimroth and S. Kurtz, “High-efficiency multijunction solar cells,” *MRS bulletin*, vol. 32, no. 3, pp. 230–235, 2007.
- [20] M. Heydarian, C. Messmer, A. J. Bett, M. Heydarian, D. Chojniak, Ö. Ş. Kabaklı, L. Tutsch, M. Bivour, G. Siefer, M. C. Schubert, *et al.*, “Maximizing current density in monolithic perovskite silicon tandem solar cells,” *Solar RRL*, vol. 7, no. 7, p. 2200930, 2023.
- [21] W. Shockley and H. Queisser, “Detailed balance limit of efficiency of p–n junction solar cells,” in *Renewable energy*, pp. Vol2_35–Vol2_54, Routledge, 2018.
- [22] R. Kellenbenz, R. Hoheisel, P. Kailuweit, W. Guter, F. Dimroth, and A. W. Bett, “Development of radiation hard Ga 0.50 in 0.50 p/Ga 0.99 in 0.01 μm^2 space solar cells with multi quantum wells,” in *2010 35th IEEE Photovoltaic Specialists Conference*, pp. 000117–000122, IEEE, 2010.
- [23] A. Marti and G. L. Araújo, “Limiting efficiencies for photovoltaic energy conversion in multigap systems,” *Solar Energy Materials and Solar Cells*, vol. 43, no. 2, pp. 203–222, 1996.
- [24] A. Yamamoto, K. Sugita, A. Bhuiyan, A. Hashimoto, and N. Narita, “Metal-organic vapor-phase epitaxial growth of InGa and InAlN for multi-junction tandem solar cells,” *Materials for Renewable and Sustainable Energy*, vol. 2, pp. 1–9, 2013.
- [25] J. F. Geisz, R. M. France, K. L. Schulte, M. A. Steiner, A. G. Norman, H. L. Guthrey, M. R. Young, T. Song, and T. Moriarty, “Six-junction III–V solar cells with 47.1% conversion efficiency under 143 suns concentration,” *Nature energy*, vol. 5, no. 4, pp. 326–335, 2020.
- [26] E. H. Jung, N. J. Jeon, E. Y. Park, C. S. Moon, T. J. Shin, T.-Y. Yang, J. H. Noh, and J. Seo, “Efficient, stable and scalable perovskite solar cells using poly (3-hexylthiophene),” *Nature*, vol. 567, no. 7749, pp. 511–515, 2019.

- [27] K. Yoshikawa, H. Kawasaki, W. Yoshida, T. Irie, K. Konishi, K. Nakano, T. Uto, D. Adachi, M. Kanematsu, H. Uzu, *et al.*, “Silicon heterojunction solar cell with interdigitated back contacts for a photoconversion efficiency over 26%,” *Nature energy*, vol. 2, no. 5, pp. 1–8, 2017.
- [28] M. Green, E. D. Dunlop, J. Hohl-Ebinger, M. Yoshita, N. Kopidakis, and X. Hao, “Solar cell efficiency tables (version 56),” *Prog. Photovolt. Res. Appl.*, vol. 28, p. 629, 2020.
- [29] J. Tong, Z. Song, D. H. Kim, X. Chen, C. Chen, A. F. Palmstrom, P. F. Ndione, M. O. Reese, S. P. Dunfield, O. G. Reid, *et al.*, “Carrier lifetimes of $> 1 \mu\text{s}$ in sn-pb perovskites enable efficient all-perovskite tandem solar cells,” *Science*, vol. 364, no. 6439, pp. 475–479, 2019.
- [30] J. H. Heo, D. H. Song, and S. H. Im, “Planar $\text{ch}_3\text{nh}_3\text{pbbr}_3$ hybrid solar cells with 10.4% power conversion efficiency, fabricated by controlled crystallization in the spin-coating process,” *Advanced Materials*, vol. 26, no. 48, pp. 8179–8183, 2014.
- [31] M. Saliba, T. Matsui, K. Domanski, J.-Y. Seo, A. Ummadisingu, S. M. Za-keeruddin, J.-P. Correa-Baena, W. R. Tress, A. Abate, A. Hagfeldt, *et al.*, “Incorporation of rubidium cations into perovskite solar cells improves photovoltaic performance,” *Science*, vol. 354, no. 6309, pp. 206–209, 2016.
- [32] Z. Li, Y. Zhao, X. Wang, Y. Sun, Z. Zhao, Y. Li, H. Zhou, and Q. Chen, “Cost analysis of perovskite tandem photovoltaics,” *Joule*, vol. 2, no. 8, pp. 1559–1572, 2018.
- [33] S. P. Philipps, A. W. Bett, K. Horowitz, and S. Kurtz, “Current status of concentrator photovoltaic (cpv) technology,” tech. rep., National Renewable Energy Lab.(NREL), Golden, CO (United States), 2015.
- [34] Y. Xing, P. Han, S. Wang, Y. Fan, P. Liang, Z. Ye, X. Li, S. Hu, S. Lou, C. Zhao, *et al.*, “Performance analysis of vertical multi-junction solar cell with front surface diffusion for high concentration,” *Solar energy*, vol. 94, pp. 8–18, 2013.

- [35] H. Yuen, M. Wiemer, and V. Sabnis, “High efficiency solar cells at solar junction,” in *Renewable Energy and the Environment*, p. SRWB3, Optica Publishing Group, 2011.
- [36] J. M. Russo, D. Zhang, M. Gordon, S. Vorndran, Y. Wu, and R. K. Kostuk, “Spectrum splitting metrics and effect of filter characteristics on photovoltaic system performance,” *Optics express*, vol. 22, no. 102, pp. A528–A541, 2014.
- [37] M. Bonnet-Eymard, M. Boccard, G. Bugnon, F. Sculati-Meillaud, M. Despeisse, and C. Ballif, “Optimized short-circuit current mismatch in multi-junction solar cells,” *Solar energy materials and solar cells*, vol. 117, pp. 120–125, 2013.
- [38] M. Yamaguchi, K.-I. Nishimura, T. Sasaki, H. Suzuki, K. Arafune, N. Kojima, Y. Ohsita, Y. Okada, A. Yamamoto, T. Takamoto, *et al.*, “Novel materials for high-efficiency iii–v multi-junction solar cells,” *Solar Energy*, vol. 82, no. 2, pp. 173–180, 2008.
- [39] A. J. Nozik, “Photoelectrochemistry: applications to solar energy conversion,” *Annual review of physical chemistry*, vol. 29, no. 1, pp. 189–222, 1978.
- [40] L. Z. Broderick, B. R. Albert, B. S. Pearson, L. C. Kimerling, and J. Michel, “Design for energy: Modeling of spectrum, temperature and device structure dependences of solar cell energy production,” *Solar Energy Materials and Solar Cells*, vol. 136, pp. 48–63, 2015.
- [41] S. Kiyae, Y. Saboohi, and A. Z. Moshfegh, “A new designed linear fresnel lens solar concentrator based on spectral splitting for passive cooling of solar cells,” *Energy Conversion and Management*, vol. 230, p. 113782, 2021.
- [42] D. Zhang, Y. Wu, J. M. Russo, M. Gordon, S. Vorndran, and R. K. Kostuk, “Optical performance of dichroic spectrum-splitting filters,” *Journal of Photonics for Energy*, vol. 4, no. 1, pp. 043095–043095, 2014.
- [43] Y. Ji, A. Ollanik, N. Farrar-Foley, Q. Xu, L. Madrone, P. Lynn, V. Romanin, D. Codd, and M. Escarra, “Transmissive spectrum splitting multi-junction solar module for hybrid cpv/csp system,” in *2015 IEEE 42nd Photovoltaic Specialist Conference (PVSC)*, pp. 1–5, IEEE, 2015.

- [44] H. A. Macleod and H. A. Macleod, *Thin-film optical filters*. CRC press, 2010.
- [45] N. Mohammad, P. Wang, D. J. Friedman, and R. Menon, “Enhancing photovoltaic output power by 3-band spectrum-splitting and concentration using a diffractive micro-optic,” *Optics Express*, vol. 22, no. 106, pp. A1519–A1525, 2014.
- [46] M. V. Collados, D. Chemisana, and J. Atencia, “Holographic solar energy systems: The role of optical elements,” *Renewable and Sustainable Energy Reviews*, vol. 59, pp. 130–140, 2016.
- [47] B. N. Gün and E. Yüce, “Wavefront shaping assisted design of spectral splitters and solar concentrators,” *Scientific Reports*, vol. 11, no. 1, p. 2825, 2021.
- [48] M. Stefancich, A. Zayan, M. Chiesa, S. Rampino, D. Roncati, L. Kimerling, and J. Michel, “Single element spectral splitting solar concentrator for multiple cells cpv system,” *Optics express*, vol. 20, no. 8, pp. 9004–9018, 2012.
- [49] W. Bloss, M. Griesinger, and E. Reinhardt, “Dispersive concentrating systems based on transmission phase holograms for solar applications,” *Applied optics*, vol. 21, no. 20, pp. 3739–3742, 1982.
- [50] Y.-S. Cheng and R.-C. Chang, “Characteristics of a prism-pair anamorphic optical system for multiplex holography,” *Optical Engineering*, vol. 37, no. 10, pp. 2717–2725, 1998.
- [51] H. Angelskår, I.-R. Johansen, M. Lacolle, H. Sagberg, and A. S. Sudbø, “Spectral uniformity of two-and four-level diffractive optical elements for spectroscopy,” *Optics Express*, vol. 17, no. 12, pp. 10206–10222, 2009.
- [52] N. Kazanskiy, “Modeling diffractive optics elements and devices,” in *Optical Technologies in Telecommunications 2017*, vol. 10774, pp. 206–216, SPIE, 2018.
- [53] M. R. Taghizadeh, P. Blair, B. Layet, I. Barton, A. Waddie, and N. Ross, “Design and fabrication of diffractive optical elements,” *Microelectronic Engineering*, vol. 34, no. 3-4, pp. 219–242, 1997.

- [54] J.-S. Sohn, M.-B. Lee, W.-C. Kim, E.-H. Cho, T.-W. Kim, C.-Y. Yoon, N.-C. Park, and Y.-P. Park, "Design and fabrication of diffractive optical elements by use of gray-scale photolithography," *Applied optics*, vol. 44, no. 4, pp. 506–511, 2005.
- [55] A. Yolalmaz and E. Yüce, "Spectral splitting and concentration of broadband light using neural networks," *APL Photonics*, vol. 6, no. 4, 2021.
- [56] G. Wang, B. Wang, X. Yuan, J. Lin, and Z. Chen, "Novel design and analysis of a solar pvt system using lfr concentrator and nano-fluids optical filter," *Case Studies in Thermal Engineering*, vol. 27, p. 101328, 2021.
- [57] I. Mingareev, R. Berlich, T. Eichelkraut, H. Herfurth, S. Heinemann, and M. Richardson, "Diffractive optical elements utilized for efficiency enhancement of photovoltaic modules," *Optics Express*, vol. 19, no. 12, pp. 11397–11404, 2011.
- [58] W. E. Sha, W. C. Choy, and W. C. Chew, "Angular response of thin-film organic solar cells with periodic metal back nanostrips," *Optics letters*, vol. 36, no. 4, pp. 478–480, 2011.
- [59] M. Freitag, J. Teuscher, Y. Saygili, X. Zhang, F. Giordano, P. Liska, J. Hua, S. M. Zakeeruddin, J.-E. Moser, M. Grätzel, *et al.*, "Dye-sensitized solar cells for efficient power generation under ambient lighting," *Nature Photonics*, vol. 11, no. 6, pp. 372–378, 2017.
- [60] J. Y. Y. Loh and N. Kherani, "Design of nano-porous multilayer antireflective coatings," *Coatings*, vol. 7, no. 9, p. 134, 2017.
- [61] S. Jalaly, M. Vahdani, M. Shahabadi, and G. M. M. Sadeghi, "Design, fabrication, and measurement of a polymer-based anti-reflection coating for improved performance of a solar panel under a specific incident angle," *Solar Energy Materials and Solar Cells*, vol. 189, pp. 175–180, 2019.
- [62] Z. Tang, W. Tress, and O. Inganäs, "Light trapping in thin film organic solar cells," *Materials today*, vol. 17, no. 8, pp. 389–396, 2014.

- [63] V. V. Iyengar, B. K. Nayak, and M. C. Gupta, “Optical properties of silicon light trapping structures for photovoltaics,” *Solar Energy Materials and Solar Cells*, vol. 94, no. 12, pp. 2251–2257, 2010.
- [64] A. Amelia, Y. Irwan, I. Safwati, W. Leow, M. H. Mat, and M. S. A. Rahim, “Technologies of solar tracking systems: A review,” in *IOP Conference Series: Materials Science and Engineering*, vol. 767, p. 012052, IOP Publishing, 2020.
- [65] Y. A. Akimov and W. S. Koh, “Design of plasmonic nanoparticles for efficient subwavelength light trapping in thin-film solar cells,” *Plasmonics*, vol. 6, pp. 155–161, 2011.
- [66] H. A. Atwater and A. Polman, “Plasmonics for improved photovoltaic devices,” *Nature materials*, vol. 9, no. 3, pp. 205–213, 2010.
- [67] H. A. Kazem, M. T. Chaichan, A. H. Al-Waeli, and K. Sopian, “Dual axis solar photovoltaic trackers: An in-depth review,” *Energy Sources, Part A: Recovery, Utilization, and Environmental Effects*, vol. 46, no. 1, pp. 15331–15356, 2024.
- [68] G. C. Lazaroiu, M. Longo, M. Roscia, and M. Pagano, “Comparative analysis of fixed and sun tracking low power pv systems considering energy consumption,” *Energy Conversion and Management*, vol. 92, pp. 143–148, 2015.
- [69] Z. R. K. Abojela, M. K. M. Desa, and A. H. Sabry, “Current prospects of building-integrated solar pv systems and the application of bifacial pvs,” *Frontiers in Energy Research*, vol. 11, p. 1164494, 2023.
- [70] E. D. Kosten, J. H. Atwater, J. Parsons, A. Polman, and H. A. Atwater, “Highly efficient gaas solar cells by limiting light emission angle,” *Light: Science & Applications*, vol. 2, no. 1, pp. e45–e45, 2013.
- [71] G. Dennler, K. Forberich, M. C. Scharber, C. J. Brabec, I. Tomiš, K. Hingerl, and T. Fromherz, “Angle dependence of external and internal quantum efficiencies in bulk-heterojunction organic solar cells,” *Journal of Applied Physics*, vol. 102, no. 5, 2007.
- [72] D. Cheyns, B. Rand, B. Verreert, J. Genoe, J. Poortmans, and P. Heremans, “The angular response of ultrathin film organic solar cells,” *Applied physics letters*, vol. 92, no. 24, 2008.

- [73] D. D’Ercole, L. Dominici, T. M. Brown, F. Michelotti, A. Reale, and A. Di Carlo, “Angular response of dye solar cells to solar and spectrally resolved light,” *Applied Physics Letters*, vol. 99, no. 21, 2011.
- [74] V. Stockhausen, L. Andrade, D. Ivanou, B. Stannowski, and A. Mendes, “Incident angle and light intensity variation: a comparative impact study on perovskite, dye-sensitized and silicon heterojunction solar cells towards building-integrated applications,” *Solar Energy Materials and Solar Cells*, vol. 191, pp. 451–458, 2019.
- [75] J. Balenzategui and F. Chenlo, “Measurement and analysis of angular response of bare and encapsulated silicon solar cells,” *Solar Energy Materials and Solar Cells*, vol. 86, no. 1, pp. 53–83, 2005.
- [76] P. F. Felzenszwalb and D. P. Huttenlocher, “Efficient graph-based image segmentation,” *International journal of computer vision*, vol. 59, pp. 167–181, 2004.
- [77] R. Achanta, A. Shaji, K. Smith, A. Lucchi, P. Fua, and S. Süsstrunk, “Slic superpixels compared to state-of-the-art superpixel methods,” *IEEE transactions on pattern analysis and machine intelligence*, vol. 34, no. 11, pp. 2274–2282, 2012.
- [78] Ren and Malik, “Learning a classification model for segmentation,” in *Proceedings ninth IEEE international conference on computer vision*, pp. 10–17, IEEE, 2003.
- [79] S. Ans, F. Zamkotsian, and G. Demésy, “Topology optimization of blazed gratings under conical incidence,” *Journal of the Optical Society of America A*, vol. 41, no. 8, pp. 1531–1543, 2024.
- [80] H. Yılmaz, W. L. Vos, and A. P. Mosk, “Optimal control of light propagation through multiple-scattering media in the presence of noise,” *Biomedical optics express*, vol. 4, no. 9, pp. 1759–1768, 2013.
- [81] A. C. Hardy and F. H. Perrin, *The principles of optics*. McGraw-Hill book Company, Incorporated, 1932.

- [82] J. W. Goodman, *Introduction to Fourier optics*. Roberts and Company publishers, 2005.
- [83] R. Baierlein, *Thermal physics*. Cambridge University Press, 1999.
- [84] “Refractive index of BK7 glass,” 2023.
- [85] T. P. Xiao, O. S. Cifci, S. Bhargava, H. Chen, T. Gissibl, W. Zhou, H. Giessen, K. C. Toussaint Jr, E. Yablonovitch, and P. V. Braun, “Diffractive spectral-splitting optical element designed by adjoint-based electromagnetic optimization and fabricated by femtosecond 3d direct laser writing,” *ACS Photonics*, vol. 3, no. 5, pp. 886–894, 2016.
- [86] O. Tokel, A. Turnalı, G. Makey, P. Elahi, T. Çolakoğlu, E. Ergeçen, Ö. Yavuz, R. Hübner, M. Zolfaghari Borra, I. Pavlov, *et al.*, “In-chip microstructures and photonic devices fabricated by nonlinear laser lithography deep inside silicon,” *Nature photonics*, vol. 11, no. 10, pp. 639–645, 2017.
- [87] C. Dix, P. McKee, A. Thurlow, J. Towers, D. Wood, N. Dawes, and J. Whitney, “Electron-beam fabrication and focused ion beam inspection of submicron structured diffractive optical elements,” *Journal of Vacuum Science & Technology B: Microelectronics and Nanometer Structures Processing, Measurement, and Phenomena*, vol. 12, no. 6, pp. 3708–3711, 1994.
- [88] Y. Fu and B. K. A. Ngoi, “Investigation of diffractive optical element fabricated on diamond film by use of focused ion beam direct milling,” *Optical Engineering*, vol. 42, no. 8, pp. 2214–2217, 2003.
- [89] P. Zhou, C. Xue, C. Yang, C. Liu, and X. Liu, “Diffraction efficiency evaluation for diamond turning of harmonic diffractive optical elements,” *Applied Optics*, vol. 59, no. 6, pp. 1537–1544, 2020.
- [90] C. Song, Y. Dai, X. Peng, Y. Wang, and Y. Su, “Machining model of position-attitude in magnetorheological finishing (mrf) of high-precision off-axis aspheric optical elements,” *International Journal of Precision Engineering and Manufacturing*, vol. 14, pp. 1455–1463, 2013.
- [91] R. Eshel, V. Frumkin, M. Nice, O. Luria, B. Ferdman, N. Opatovski, K. Gommed, M. Shusteff, Y. Shechtman, and M. Bercovici, “Fabrication of

diffractive optical elements by programmable thermocapillary shaping of thin liquid films,” *arXiv preprint arXiv:2109.00158*, 2021.

- [92] R. N. Widmer, D. Bischof, J. Jurczyk, M. Michler, J. Schwiedrzik, and J. Michler, “Smooth or not: Robust fused silica micro-components by femtosecond-laser-assisted etching,” *Materials & Design*, vol. 204, p. 109670, 2021.
- [93] R. An, Y. Li, Y. Dou, H. Yang, and Q. Gong, “Simultaneous multi-microhole drilling of soda-lime glass by water-assisted ablation with femtosecond laser pulses,” *Optics express*, vol. 13, no. 6, pp. 1855–1859, 2005.
- [94] K. Sugioka, J. Xu, D. Wu, Y. Hanada, Z. Wang, Y. Cheng, and K. Midorikawa, “Femtosecond laser 3d micromachining: a powerful tool for the fabrication of microfluidic, optofluidic, and electrofluidic devices based on glass,” *Lab on a Chip*, vol. 14, no. 18, pp. 3447–3458, 2014.
- [95] E. Casamenti, S. Pollonghini, and Y. Bellouard, “Few pulses femtosecond laser exposure for high efficiency 3d glass micromachining,” *Optics express*, vol. 29, no. 22, pp. 35054–35066, 2021.
- [96] C. A. Ross, D. G. MacLachlan, D. Choudhury, and R. R. Thomson, “Optimisation of ultrafast laser assisted etching in fused silica,” *Optics express*, vol. 26, no. 19, pp. 24343–24356, 2018.
- [97] J. M. Fernández-Pradas, D. Serrano, S. Bosch, J. Morenza, and P. Serra, “3d features of modified photostructurable glass–ceramic with infrared femtosecond laser pulses,” *Applied surface science*, vol. 257, no. 12, pp. 5219–5222, 2011.
- [98] A. Folch, A. Ayon, O. Hurtado, M. Schmidt, and M. Toner, “Molding of deep polydimethylsiloxane microstructures for microfluidics and biological applications,” 1999.
- [99] D. Cai, A. Neyer, R. Kuckuk, and H. Heise, “Optical absorption in transparent pdms materials applied for multimode waveguides fabrication,” *Optical materials*, vol. 30, no. 7, pp. 1157–1161, 2008.

- [100] L. Chen, X. Chen, Z. Zhang, T. Li, T. Zhao, X. Li, and J. Zhang, "Pdms-based capacitive pressure sensor for flexible transparent electronics," *Journal of Sensors*, vol. 2019, no. 1, p. 1418374, 2019.
- [101] A. S. M. Sayem, R. B. Simorangkir, K. P. Esselle, and R. M. Hashmi, "Feasibility study of pdms embedded transparent conductive fabric for the realization of transparent flexible antennas," in *2019 13th European Conference on Antennas and Propagation (EuCAP)*, pp. 1–4, IEEE, 2019.
- [102] V. Prajzler, P. Nekvindova, J. Spirkova, and M. Novotny, "The evaluation of the refractive indices of bulk and thick polydimethylsiloxane and polydimethyl-diphenylsiloxane elastomers by the prism coupling technique," *Journal of Materials Science: Materials in Electronics*, vol. 28, pp. 7951–7961, 2017.
- [103] I. D. Johnston, D. K. McCluskey, C. K. Tan, and M. C. Tracey, "Mechanical characterization of bulk sylgard 184 for microfluidics and microengineering," *Journal of Micromechanics and Microengineering*, vol. 24, no. 3, p. 035017, 2014.
- [104] J. Gawedzinski, M. E. Pawlowski, and T. S. Tkaczyk, "Quantitative evaluation of performance of three-dimensional printed lenses," *Optical engineering*, vol. 56, no. 8, pp. 084110–084110, 2017.
- [105] Z. Hong and R. Liang, "Ir-laser assisted additive freeform optics manufacturing," *Scientific reports*, vol. 7, no. 1, pp. 1–7, 2017.
- [106] P. Gašo, D. Pudiš, D. Seyringer, A. Kuzma, L. Gajdošová, T. Mizera, and M. Goraus, "3d polymer based 1x4 beam splitter," *Journal of Lightwave Technology*, vol. 39, no. 1, pp. 154–161, 2020.
- [107] H. Wang, H. Wang, W. Zhang, and J. K. Yang, "Toward near-perfect diffractive optical elements via nanoscale 3d printing," *ACS nano*, vol. 14, no. 8, pp. 10452–10461, 2020.
- [108] S. N. B. Oliaei and B. Nasserri, "6. stereolithography and its applications," *Additive and Subtractive Manufacturing*, vol. 1, pp. 229–250, 2020.

- [109] J. Borrello, P. Nasser, J. C. Iatridis, and K. D. Costa, “3d printing a mechanically-tunable acrylate resin on a commercial dlp-sla printer,” *Additive manufacturing*, vol. 23, pp. 374–380, 2018.
- [110] Anycubic, “How to use high clear resin,” 2023. Accessed: 2024-08-21.
- [111] G. Berglund, A. Wisniowiecki, J. Gawedzinski, B. Applegate, and T. S. Tkaczyk, “Additive manufacturing for the development of optical/photonic systems and components,” *Optica*, vol. 9, no. 6, pp. 623–638, 2022.
- [112] M. Fligge, S. Solanki, Y. Unruh, C. Fröhlich, and C. Wehrli, “A model of solar total and spectral irradiance variations,” *Astronomy and Astrophysics*, v. 335, p. 709-718 (1998), vol. 335, pp. 709–718, 1998.
- [113] J. Chantana, Y. Horio, Y. Kawano, Y. Hishikawa, and T. Minemoto, “Spectral mismatch correction factor for precise outdoor performance evaluation and description of performance degradation of different-type photovoltaic modules,” *Solar Energy*, vol. 181, pp. 169–177, 2019.
- [114] J. Chantana, H. Mano, Y. Horio, Y. Hishikawa, and T. Minemoto, “Spectral mismatch correction factor indicated by average photon energy for precise outdoor performance measurements of different-type photovoltaic modules,” *Renewable Energy*, vol. 114, pp. 567–573, 2017.
- [115] P. Pradhan and H. Murthy, “Application of undercut and fgm to mitigate stress gradients in cylindrical contacts,” *The Journal of Strain Analysis for Engineering Design*, vol. 60, no. 1, pp. 37–48, 2025.
- [116] K. Pavani, J. S. Kumar, and K. U. Kumar, “Novel luminescent transparent ceramics for light emitting devices,” in *Luminescent Ceramics*, pp. 265–283, Elsevier, 2025.

CURRICULUM VITAE

Parisa Naghinazhadahmadi

Educational Background

PhD Candidate

Micro and Nano Technology, Middle East Technical University

Thesis: Reflective and Transparent Diffractive Optical Elements and their Angular Response

M.Sc.

Electrical and Electronics Engineering, Azad University of Iran, Tabriz Branch

Thesis: Design and simulation of Organic Light Emitting Diode (OLED)

B.Sc.

Electrical and Electronics Engineering, Azad University of Iran, Tabriz Branch

Research Projects

- MEMS-based Microbial Fuel Cells TÜBİTAK 113E195 (Boursier)
- Accurate Electromagnetic Analysis and Optimizations of Photonic Crystals Involving Dielectric Rods (DEMOS), TÜBİTAK -1001 (Boursier)

Teaching & Working Experiences

- Lecturer (Part-time) at TED University (2024-2025)
 - CMPE371 - Signals and Systems
 - CMPE113 - Fundamentals of Programming (I)
- Teaching Assistant at TED University (2018-2024)

- Teaching Assistant at Middle East Technical University (2021-2023)
- Lecturer at Azad University of Mameghan, Sama Technical & Vocational College, Iran (2007-2009)
 - Electrical Circuits
 - Analog Electronics Lab
- Lecturer at Azad University of Iran, Sofian Branch (2008-2009)
 - Systems and Control (Theory and Lab)
- Research Engineer at Petrochemical Company of Tabriz (Polynar) (2006-2007)

Publications & Presentations

- Naghinazhadahmadi, P., B.,N., Gün, Atila, S., Yolalmaz, Yüce, E. (2025). Angle Independent Spectral Splitting and Concentration of White Light Using SpliCons. *ACS Photonics Journal* (submitted).
- Naghinazhadahmadi, P., Pavlov, I., Yüce, E. (2024). Angle Independent DOEs for Enhanced Solar Cell Efficiency, 4th International Conference on Photovoltaic Sciences and Technologies (PVCON 2024), 38 July 2024, Ankara, Turkey. (Poster)
- Naghinazhadahmadi, P., Gün, B.,N., Atila, S., Yolalmaz, A., Yüce, E. (2022). Angle Independent Diffractive Optical Elements to Improve the Efficiency of Solar Cells, 3rd International Conference on Photovoltaic Sciences and Technologies (PVCON 2022), 57 July 2022, Ankara, Turkey.
- Atila, S., Yolalmaz, A., Gün, B.,N., Naghinazhadahmadi, P., Yüce, E. (2022). Enhancing Performance of GaAs Solar Cell via Wavefront Shaping, 3rd International Conference on Photovoltaic Sciences and Technologies (PVCON 2022), 57 July 2022, Ankara, Turkey. (Poster)
- Ayan, A., Turkay, D., Unlu, B., Naghinazhadahmadi, P., Oliaei, S. N. B., Boztug, C., & Yerci, S. (2019). Strain Engineering of Germanium Nanobeams by Electrostatic Actuation. *Scientific Reports*, 9(1), 4963.

- Rostami, A., Janabi-Sharifi, F., and Naghinazhadahmadi, P. (2010). Finite Difference Modeling of Bipolar OLED, ISOT 2010 International Symposium on Optomechatronic Technologies, 25-27 October 2010, Toronto, Canada.
- P. Naghinazhadahmadi, Masumeh Alizadeh (2010). Design and Simulation of Organic Light Emitting Diodes (OLEDs), 13th Iranian Student Conference on Electrical Engineering, September 2010, Tehran, Iran.

Lingual Skills

- Turkish (Azeri) & Persian: Native
- English:
 - YDS: 85
 - TOEFL IBT: 87
 - Reading: 21, Listening: 21, Speaking: 24, Writing: 21
- Turkish (Istanbul): Fluent

Software and Programming Languages

- Programming Languages: MATLAB, LabVIEW
- Analysis Packages: HSPICE, COMSOL, PSPICE, CADENCE, AWR, CST

Research Interests

- Optoelectronics
- OLED, Solar Cells
- MEMS
- Micro and Nano Fabrication